ABSTRACT

MECHANICAL CHARACTERIZATION OF ANIMAL DERIVED STARTING MATERIALS FOR TISSUE ENGINEERING

by
Bin Zhang

Animal derived starting materials are well established in the production of Tissue Engineered Medical Devices. Porcine specifically can be found in products ranging in application from hernia repair to breast reconstruction. Although this material has been largely accepted in the Tissue Engineering industry, little is known of its material properties and mechanical characteristics. A review of the scientific literature describes limited mechanical measures only on uncontrolled research grade material. The objective of this work is to mechanically characterize porcine starting material used in the medical device industry. Porcine skin is provided by Midwest Research Swine, LLC (MRS) an established supplier to Medical Device companies. The experiments are established to evaluate if the skin's mechanical characteristics vary by location and direction. The porcine skin samples are marked for their location (Back and Neck) as well as Orientation (Head and Spine). A custom die is used to prepare uniaxial tensile samples parallel, perpendicular, and at 45 degrees from the Spine landmark. An MTS load frame and Digital Image Correlation (DIC) measurement system is used to acquire the stress-stretch relationship. Mechanical indices from the stress-stretch relationship is analyzed by first separating it into a toe and linear region through a bilinear curve fitting method, apply the Ogden hypereslastic material model to the Toe, and linear model to the linear region. The Ogden fit in the toe region reveals anisotropic behavior that varied by location on the porcine skin, where the Back region behaves anisotropically and the Neck isotopically.

The Gasser-Ogden-Holzepfel (GOH) structural model is explored to unify the tissue's directional properties. The GOH model requires that the microstructural element's (e.g., collagen fiber) arrangement within the macroscopic tissue is known beforehand. In the literature this is accomplished through histological measurements on the tissue itself. This requirement limits the ability of the GOH model to be used in the real time analysis of experimental work, which is needed in both academia and the tissue engineering industry. A method is developed to determine the microstructural arrangement (angle and dispersion) by utilizing the mechanical response at two orientations. This developed Microstructural Arrangement Determination Method (MADM) is verified by reproducing a GOH ABAQUS model from the literature. MADM is then applied to porcine skin experimental data, revealing a potential limitation of the GOH model in its treatment of transverse strain.

MECHANICAL CHARACTERIZATION OF ANIMAL DERIVED STARTING MATERIALS FOR TISSUE ENGINEERING

by
Bin Zhang

A Dissertation
Submitted to the Faculty of
New Jersey Institute of Technology
in Partial Fulfillment of the Requirements for the Degree of
Doctor of Philosophy in Mechanical Engineering

Department of Mechanical and Industrial Engineering

May 2020

.

APPROVAL PAGE

MECHANICAL CHARACTERIZATION OF ANIMAL DERIVED STARTING MATERIALS FOR TISSUE ENGINEERING

Bin Zhang

Dr. Samuel C. Lieber, Dissertation Advisor — Date
Assistant Professor of Engineering Technology, NJIT

Dr. Joga I. Rao, Committee Member — Date
Professor and Chair of Mechanical and Industrial Engineering, NJIT

Dr. Shawn A. Chester, Committee Member — Date
Associate Professor of Mechanical and Industrial Engineering, NJIT

Dr. Eun Lee, Committee Member — Date
Associate Professor of Biomedical Engineering, NJIT

Dr. Siva P. Nadimpalli, Committee Member — Date
Associate Professor of Mechanical Engineering, Michigan State University

BIOGRAPHICAL SKETCH

Author: Bin Zhang

Degree: Doctor of Philosophy

Date: May 2020

Undergraduate and Graduate Education:

- Doctor of Philosophy in Mechanical Engineering,
  New Jersey Institute of Technology, Newark, NJ, 2020

- Master of Science in Mechanical Engineering,
  New Jersey Institute of Technology, Newark, NJ, 2016

- Bachelor of Science in Thermal Energy and Power Engineering,
  Shanghai Institute of Technology, Shanghai, P. R. China, 2013

Major: Mechanical Engineering

Presentations and Publications:

Bin Zhang, Bob Tarantino, and Samuel C. Lieber. "Effect of Metal Additive Manufacturing on the Engineering Design of Manufacturing Tooling: A Case Study on Dies for Plastic Extruded Products." ASME International Mechanical Engineering Congress and Exposition. American Society of Mechanical Engineers Digital Collection, 2017.

Samuel Lieber, Bin Zhang, Shawn Chester, Siva Nadimpalli, Justin Suriano, Nicholas Santoro, David Theis,. Mechanical Characterization of Porcine Starting Material Reveals Location Dependent Auxetic Behavior. Biomedical Engineering Society Annual Meeting 2018, Atlanta Georgia.

Bin Zhang, Shawn A. Chester, Siva P.V. Nadimpalli, Justin T. Suriano, David P. Theis, Samuel C. Lieber. "Mechanical Characterization of Porcine Skin Starting Material." (Submitted).

献给我亲爱的家人们。

感谢你们一直以来的支持与信赖。

Dedicated to my dear family.

Thank you for the support and trust all the time.

ACKNOWLEDGMENT

Over the four years of my PhD life, I am so lucky to be surrounded by so many supportive talented and inspiring individuals. I would like to express my special thanks to my Thesis and Dissertation advisor Dr. Samuel C. Lieber in Engineering Technology department who have been a mentor, and a teacher. He made my PhD journey more rewarding, and taught me how to be a researcher and problem-solver. I also would like to thank my dissertation committee of Dr. Shawn A. Chester, Dr. Siva P. Nadimpalli, Dr. Joga I. Rao, and Dr. Alice Lee for their supports and encouragements over the past three years.

I appreciate the funding from Engineering Technology department for the last four years. I also appreciate the experiment materials provided from Midwest Research Swine, LLC.

TABLE OF CONTENTS

TABLE OF CONTENTS
(Continued)

Chapter **Page**

TABLE OF CONTENTS
(Continued)

Chapter **Page**

TABLE OF CONTENTS
(Continued)

LIST OF TABLES

LIST OF FIGURES

LIST OF FIGURES
(Continued)

LIST OF FIGURES
(Continued)

Figure **Page**

LIST OF FIGURES
(Continued)

LIST OF FIGURES
(Continued)

CHAPTER 1

INTRODUCTION

1.1 Study Material Introduction

Meshes are used in a number of medical device products including hernia repair [1-3] and breast reconstruction [4, 5]. Biologic meshes fall under two groups of homografts and xenografts [6]. The latter are regulated by the Food and Drug Administration (FDA) [6, 7]and include tissues from porcine and bovine sources [1]. Among the xenograft options, porcine has dominated the medical device market [8]. The porcine skin's dermis is the most common tissue type [3, 8] because it can be harvested in larger sheets thus providing the larger size options found in several released medical device products [2, 6]. Although porcine skin is an established medical device starting material regulated by the FDA, little is known about its mechanical properties. The FDA provides guidance for mesh products used in general surgery. This regulatory guidance is for devices that are produced from either synthetic or animal derived materials (ADM). The specific guidance on ADM is that it needs to come from a controlled animal source with well documented information provided on the animal's makeup and environmental factors. The guidance for mechanical characterization; however, is not specific to ADM and is provided generally for mesh devices. This guidance is centered on failure measures including tear resistance, tensile, burst, and suture pullout strength. These mechanical measures for mesh devices are further described in the literature [1, 6, 9-11] and utilize test protocols based on the guidance from the American Society of Testing Materials (ASTM) standards [9, 10]. The general guidance provided by ASTM standards is valuable as a starting point but is not specific towards the development of tissue testing protocols. The characterization of starting

materials used in tissue engineering scaffolds can be found in ASTM F2027 [12], where ADMs are included; however, their specific mechanical testing needs are not addressed. Soft tissue ADMs, such as porcine skin, are grouped as a part of polymer starting materials, and further guidance can be found by reviewing their standards. ASTM D638 [13] provides the guidance for tensile properties of plastics. Although this standard has served as the primary guidance for tensile testing of biologic mesh devices [9], it does not address any specific guidance on testing of biologic materials.

1.2 Objective

The objective of this dissertation work is to characterize the mechanical properties of PSSM under uniaxial tension. Knowledge of the PSSM's mechanical properties would serve as a platform that could be used by companies and academics interested in exploring its use as a medical device or in novel tissue engineering processes. PSSM mechanical properties need to be geometry independent to allow the developer to readily explore diverse geometric configurations. Ideally more advanced engineering analysis could be conducted by implementing the mechanical properties in engineering simulation software (e.g., FEA). The development of the experimental and theoretical characterization methods needed for this aim could serve to further grow tissue engineering standards used to guide industry and academia. The further development of tissue engineering standards would help bring the mechanical characterization of ADMs on par with synthetic medical device materials.

The mechanical properties are further studied with both isotropic (Ogden) and anisotropic (Gasser-Holzapfel-Ogden) model.

1.3 Applications for Starting Material

The applications of porcine skin dermis can be widely found in the productions of Tissue Engineered Medical Devices, such as surgical mesh materials, and scaffolds for regenerative medicine, however little is known of its material properties and mechanical characteristics. In this section, the state-of-the-art applications of this common starting material are presented.

1.3.1 Tissue Application in Hernia Surgery

A hernia is defined as a protrusion or projection (prolapse) of an organ through the wall of the cavity where it is normally contained [14]. People suffer from different types of hernia, according to the physical location of the symptom. A report shows that about 70-75% of found hernia cases are the inguinal hernia, followed by femoral (6-17%) and umbilical (3-8.5%) hernias [15]. Hernias can be very uncomfortable, and sometimes patients also suffer from severe pain, especially during bowel movements, urination, heavy lifting, or straining [16]. Hernia repairing surgery is one of the most common surgeries all around the world. It has been estimated that there are over 20 million repairs of hernia performed each year worldwide [17]. The surgical mesh has been widely accepted for the proved reduction in hernia recurrence and postoperative pain compared to conventional suture repair, and in fact, more than 80% of hernia repairs carried out in the United States use mesh products [2, 18].

Biologic mesh materials as the third generation surgical meshes are outstanding in the mesh products for the better prevalence of adhesions, and superior biocompatibility [2]. Typically, the biologic mesh materials are made of the dermis from human, porcine, and fetal bovine, and need to be decellularized to leave only highly organized architecture with

the surrounding extracellular ground tissue. This decellularized dermis tissue provides a matrix, which allows native cells to populate and generate connective tissue that could replace the defect tissue in the hernia location [19].

1.3.2 Tissue Application in Breast Reconstruction

Breast reconstruction surgery is another big application of biological mesh. Breast cancer is the biggest cause of doing breast reconstruction surgery, and only in 2017, there are an estimated 252,710 new cases of invasive breast cancer is diagnosed among women, and 2,470 cases are diagnosed in men [20].

For women with breast cancer requiring mastectomy or lumpectomy surgery, breast reconstruction surgery is considered helpful for recovery and aesthetic purposes. Compared to the synthetic matrices, the biological scaffold can arguably provide better surgical outcomes by allowing rapid host revascularization and cell repopulation [4]. The literature also shows the biological mesh can provide better aesthetic outcomes than synthetic matrices, and the ability to incorporate into the host tissue is another distinguishing point of the biological mesh over the other methods.

1.4 Background for Midwest Research Swine (MRS)

In the literature, the material characterizations of porcine skin tissue were usually conducted on uncontrolled, non-industrial-grade materials. Industry-grade porcine skin tissue provided by Midwest Research Swine. LLC (MRS) an established supplier to Medical Device companies gives us this unique opportunity to characterize porcine skin tissue for Medical Devices. In this section, the background of MRS is introduced.

Midwest Research Swine (MRS) was founded in 1986 as the leading U.S. supplier of high quality, affordable research swine to the biomedical research industry. They have more than 25 years' experience dealing with universities, research institutes, startup companies and well-established medical companies.

The swine in MRS are tightly controlled during the entire raising process in order to avoid unnecessary variables to the experiments and researches. The pig produced by Midwest Research Swine are a mix of American Yorkshire-Landrace-Duroc. This genetic hybrid vigor and heterosis have been developed specifically for biomedical uses and not as a sideline business to selling breeding stock or packing meat products. The pigs in MRS are classified as High Health Status Herd pig, which are those managed for reproductive and weight-gain efficiencies with a minimum of medication. All the pigs for research purposes are raised inside environmentally-controlled facilities to reduce the prevalence of infectious diseases without compromising the animals' developmental vigor (thriftiness). Not only the raising process is fully controlled in MRS, but also the procedure of processing the skin tissue is also standardized. The technology they have been using to process the porcine skin is called Precision Leveling Technology (PLT). This technology is able to remove tissue layers from dermis in a very precise and controlled way under the reduced costs. See the pictures (Figure 1.1) below for procedure of PLT.

After production, the quality assurance for the products is also systematical. The piglets weaned and feed efficiency are consistently monitored according to the production performance. The death and diseases are also analyzed by monitoring both rates and causes. The pig health is quarterly laboratory tested. See Figure 1.2 for the flow chart of Total Quality Assurance Approach.

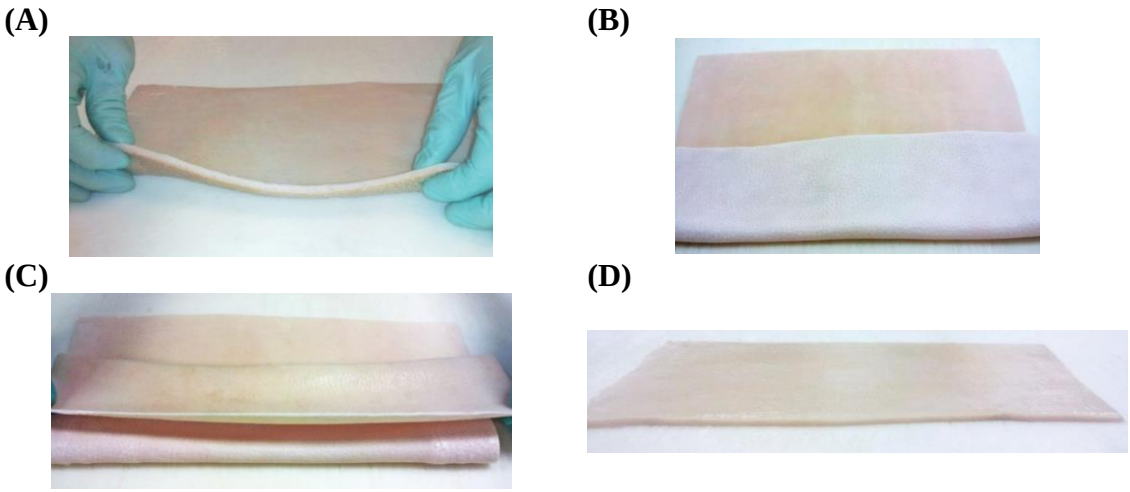

Figure 1.1 Preparation of porcine skin dermis for experiment purpose in MRS, **(A)** The raw material of skin excised from pig, **(B)** Removing the hypodermis (bottom fatty layer) from the targeted dermis section. **(C)** Removing the epidermis (top thin layer) from the targeted dermis section, **(D)** Sizing the targeted dermis section to final product thickness specifications.
Source: [21]

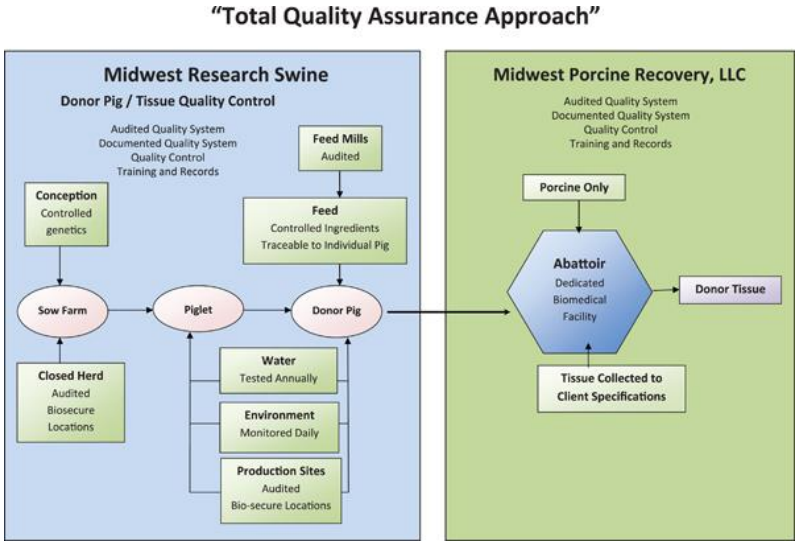

Figure 1.2 Quality Assurance Flow Chart for Production of Porcine Skin in MRS.
Source: [22].

1.5 Skin Tissue Mechanical Testing

Skin is one of the most important organs in the body with the exception of the brain. The skin is a complicated multifunctional organ covers the entire surface of the body [23]. The skin has various functions, including protecting the internal body structure from the environment, regulating body temperature, and providing a network of sensory receptors [24, 25]. Skin must be sufficiently flexible to enable large deformation in all directions during the body motion, and simultaneously have the capability to return to its original state.

In this section, the structure of the skin is described. In addition, the mechanical test approaches for characterizing the skin tissue material are listed and discussed.

1.5.1 Structure of Skin

At the meso-macroscopic level, skin is generally considered as a multi-layer structure as showed in Figure 1.3. The structure of skin can be categorized into three main layers, which are epidermis layer, dermis layer, and hypodermis layer, and each layer made of several components, which make the mechanical properties of skin very complicated. The topmost layer of skin is called epidermis which is approximately 75 – 100 m [26]. Epidermis is a waterproof layer protecting the underlying tissues from chemicals, infection, dehydration, and mechanical stress.

The second layer is the dermis, which is a thicker and fibrous tissue. Being compared to the other two layers, the dermis layer is relatively dense consisting of three fibrous proteins, collagen, elastin, and supporting matrix or ground substance. The dermis tissue consists of strong stiff collagen fibers, which contribute 75% of the dry weight of the dermis, while the rubber-like elastin make up 4% of the dry-weight and the semi-fluid

ground substance makes up 20% of the dry weight [23]. Elastin contributes mostly to the stress-strain relationship at small strains [27]. Collagen fibers are gradually recruited and start to contribute more and more when the skin tissue is stretched further.

The third layer is known as hypodermis, mainly made of adipose cells. The thickness of hypodermis varies greatly over the surface of skin [26]. The hypodermis helps insolate the body from heat and cold, cushions the impact from outside, and serves also as an energy-storage area.

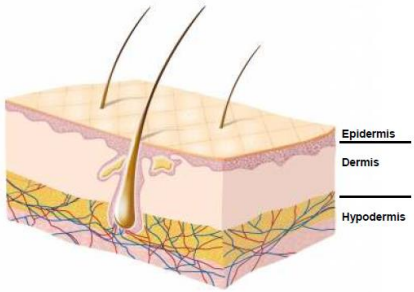

Figure 1.3 Diagram of Three Layers of Skin, including epidermis, dermis and hypoderimis.
Source: [28]

1.5.2 Testing the Mechanical Properties of Skin Ex-Vivo

Since the *ex vivo* test of skin tissues has several advantages over the *in vivo* tests, analyzing the mechanical properties of skin in *ex vivo* experiments are more commonly conducted. One of the major advantages is that the tissue excised from the body can be carried out as a destructive test to determine the failure mechanisms and the ultimate tensile strength. Another advantage is that different loading values and rates are more manageable. Furthermore, since the boundary conditions of excised skin tissue layers can be determined precisely, the stress-strain relationships can be easily modeled and quantified.

The disadvantages of experimenting with tissue samples in the *ex vivo* condition are also obvious. When the skin excised from the body, it is removed from the natural environment, which results in the elimination of pretension conditions and the source of hydration [28]. What's more, skin samples are usually preserved between excision and testing which potentially alters the mechanical properties of the tissue [29]. Caro-Bretelle, A., et al. discussed the effect of conservation of skin in saline solution and freezing may irreversibly alter the mechanical properties of porcine skin [30]. As well, the soft tissue sample tending to slip from clamp holding can be another major problem for accurate results for tensile tests.

The tensile test is the most popular method to test skin samples *ex vivo*. By this method, not only the anisotropic, viscoelastic, nonlinear, and nonhomogeneous behaviors have been proven, but also the age-related properties [31], creep impact [32], and fatigue [33] have been determined. Uniaxial tensile testing and biaxial tensile testing are the most common approaches for tensile tests.

Uniaxial Tension

For uniaxial tensile testing, samples of soft tissue are usually cut into "dog-bone" shape and stretched in one direction while held by two clamps [29, 34-40]. The uniaxial tensile tests for soft tissues are usually considered tricky because the samples tend to slip. Thus, some special approaches or clamps should be adopted for preventing the slippage of samples from clamp fixation, such as using freeze clamp [41], serrated jaw clamps [42], or holding samples with the sandpaper or tissue paper at the ends [43]. However, the uniaxial tensile test is the only feasible method of measuring the failure properties of soft tissue.

Also, the anisotropic behavior of tissue material can be easily verified by testing the samples in multiple directions with uniaxial tensile tests [29, 34, 36, 37, 39, 44-46].

Biaxial Tension

The square shape is always recruited in biaxial tensile tests. The samples are stretched in two orthogonal directions at the same rate while held by hooks or strings [47, 48]. This method can better simulate the stretching process of *in vivo* conditions. However, this method of testing can be challenging for the hooks affixed to the edge of samples tend to tear the samples, and affect the measurements of failure properties. Furthermore, hooking samples on devices of biaxial tensile tests can be time-consuming [29] which is a potential issue for sample dehydration, and decay.

1.5.3 Testing the Mechanical Properties of Human Skin

Human skin is always the most highlighted material that attracts much attention from the researchers and medical companies for widespread applications. Yet, it is commonly known that the properties of vital human skin are too complex and variable to analyze and repeat. Gallagher has shown some mechanical properties under the dynamic stretch speeds [36]. Annaidh has done uniaxial tensile tests on human skin with DIC 2D strain measurement. The averaged values of mechanical properties are revealed, and the relationship of these mechanical properties to the orientation of the Langer's lines are suggested [34]. Other researchers have also done various studies on human skin tissue in earlier times [31, 49, 50].

Even so, the accessibility to real human skin is very limited because of the difficulty of finding appropriate donators and ethical problems. Researchers are looking for good animal models as substitutes for human skin.

1.5.4 Testing the Mechanical Properties of Porcine Skin

Because of the limited accessibility to real human skin mentioned above, porcine skin has been tested as a substitute for human skin in various experiments. Furthermore, porcine skin is also a starting material of many medical products for the skin implanting industry. Porcine skin is always a popular biological material for experiments.

Ankersen testing on porcine skin aims as a substitute for human skin to quantify the force needed to penetrate human tissue[38]. Huang used biaxial tensile tests to identify the directional biomechanical properties of porcine skin tissues, and it is observed that the properties of porcine skin tissue are varying in different direction with respect to fiber directions [47]. Shergold measured uniaxial compressive responses of pig skin over a wide range of strain rates (0.004-4000 to compare different parameters of the fitted Ogden model in different strain rates [45]. Uzer used the DIC-2D method to measure the true deformation on the skin and investigate the mechanical properties of skin under tension in *ex vivo* conditions [51]. Zak tested and compared different maximum tensile strength and the slope of the linear section in the stress-strain curve (Young's Modulus) from five different regions on the pig body. However, the importance of skin orientations and more detailed locations were overlooked [40]. Lagan conducted uniaxial tensile experiments on porcine skin for two directions of the samples which are parallel and perpendicular to the spine. Nonetheless, the locations of samples are neglected which makes the mechanical properties losing generality [44].

Just like what I mentioned above, researchers have done a great deal of work on studying mechanical properties of porcine skin tissue. Yet, there is no comprehensive paper

discussing the variance of mechanical properties in terms of the location changes and orientation changes. This item is a gap needs to be filled up.

1.6 Mechanical Properties of Skin

Skin tissue is commonly known as anisotropic[46], viscoelastic [52], nonlinear [49] and non-homogeneous material because of its fibrous structure. In this section, the literature on mechanical properties of skin tissue is presented.

1.6.1 Nonlinear stress-strain relationship

Skin tissue is a well-known rubber-like material with a nonlinear stress-strain relationship due to the microstructure of skin, and the stress-strain relationship looks like Figure 1.4(A). Under uniaxial tension, the stress-strain behavior is usually split into three, normally toe (initial non-linear), linear and failure [53]. In Phase I, the collagen fibers are initially coiled and unaligned, thus contribute very little to the mechanical properties, and then the collagen fibers are engaged gradually, and getting aligned and straightened in the direction of the applied load. Hence, the contribution of collagen fibers on the material stiffness becomes more significant with the stretching process, and the stress-strain relationship in this phase is notably non-linear. At the entry of Phase II, the collagen fibers are fully aligned and straightened, and any further extension can cause the high stiffness response of skin. In this region, comparing to elastin, the collagen fibers have much more contributions to the mechanical properties which make this region can be considered as pure collagen [49]. In Phase III, the stiffness of the skin tissue is observed decreasing, which is a result of gradual breakage of the collagen fibers [39].

The identification of the transition points between the toe region and linear regions is significant. The method of Bilinear curve fitting is commonly used to identify the transition point of stress-stretch curves of soft biological tissues [54-56].

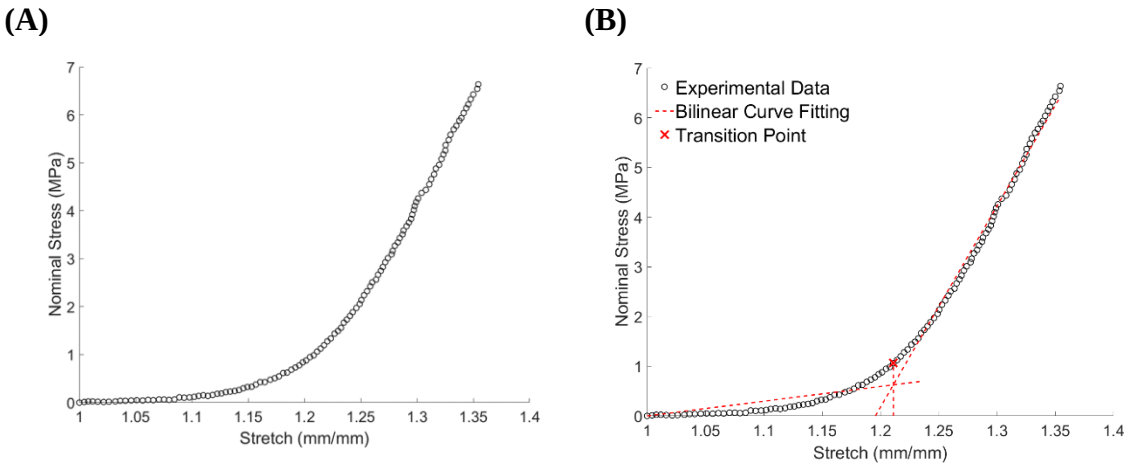

Figure 1.4 (A) Representative Tensile curve with clear non linear and linear regions. **(B)** Representative figure showing the Bilinear Fit identifying a Transition Point with a linear fit to the Toe and Linear regions respectively.

1.6.2 Viscoelasticity

Numerous researchers have shown the rate-dependence of skin tissue [36, 45, 57-60]. Shergold [45] has done uniaxial compression tests on porcine skin tissue in a wide range of strain rates from 0.004 – 4000 . The stress-strain curves are clearly different for various strain rates. The Ogden model has been fitted to these stress-strain curves for different strain rates, and the result has shown that the coefficients of the Ogden model are highly sensitive to the strain rate. It is obvious that the hyperelastic models don't take the viscoelasticity of skin tissue into account.

Dele Prete [32], Khatyr [61], and Agache [62] have reported the creep behavior of skin tissue if constant stress is applied to samples. The strain-time curves can be decomposed into three phases (Figure 1.5). Phase I is the pure elastic, and Phase II is the transition phase for viscoelastic behavior, and the sample starts to get further extended. Phase III shows the pure creep behavior of skin. Skin also exhibits the relaxation behavior

of viscoelastic materials. Stress decays over time while the sample is stretched and strain is kept at a constant level.

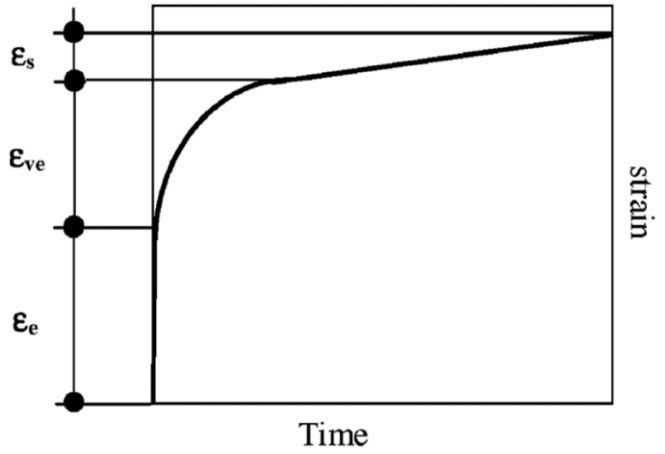

Figure 1.5 Schematic plot for typical strain – time curves for creep behavior of skin tissue.
Source: [62].

1.6.3 Anisotropy

The mechanical properties of skin tissues are generally impacted by the structure of collagen fibers. Consequently, the skin tissue is anisotropic, and direction-dependent material. The natural orientation of collagen fibers on the body is commonly known as Langer's lines (Figure 1.6). Dupuytren first recognized the phenomenon of directional tension impact on the skin [63]. Langer [64, 65] proved this influence with a large series of cadavers of different ages and different constitutions. Langer lines are a very important reference for understanding the mechanical properties of skin mapping over the entire body because the skin's mechanical anisotropy follows the same pattern as Langer lines and stretches the least along the Langer lines [25]. Rose [66] used the elliptical deformation method of the circular punch biopsy to draw the tension line on the pig skin. Three young

domestic pigs were tested and a consistent mapping was found in three animals (Figure 1.7).

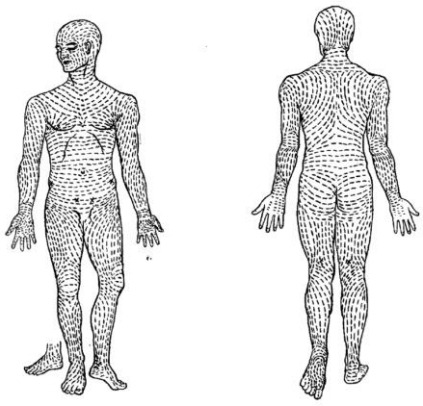

Figure 1.6 Langer's Lines over human body.
Source: [64].

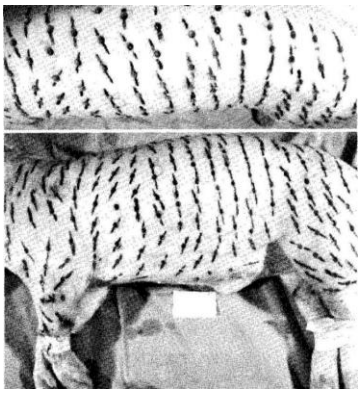

Figure 1.7 Langer's Lines over domestic porcine skin.

When the skin is stretched along the direction of Langer's lines, it is easier to get collagen fibers aligned and straightened since the collagen fibers in dermis tissue are predominantly parallel to the Langer's Lines [64, 67, 68]. Some researchers have shown the significant difference between two directions which are parallel and perpendicular to the Langer's Lines. Annaidh [34] discussed the mechanical properties of human skin in different orientations based on Langer's lines (parallel, perpendicular, and 45 bias from Langer's lines). The toe region, which is the Phase I in Figure 1.4(A), is typically shorter

for those samples stretched in the direction of Langer's Lines. It will only extend a small amount of strain before it reaches the maximum stiffness (slope of the linear region). However, the stretch across the Langer's Lines will result in a much longer toe region, which means further extension before reaching maximum stiffness.

1.6.4 Preconditioning Effect

The stress-strain behavior of connective soft tissues, such as tendon, ligament, and skin, have been proved not only to be rate-dependent materials but also as loading-history-dependent materials [57, 69, 70], which means the shape of stress-strain curves varies depending on the history of loading. During the cyclic loading and unloading of connective tissues, the stress-strain curves will follow differently. Figure 1.8 shows the typical precondition results for a typical porcine skin which is imposed on cyclic stretching up to the same maximum stress. It can be observed that the loop gradually offsets to right and the amount of shifting is decreasing until a converged hysteresis loop is obtained [29].

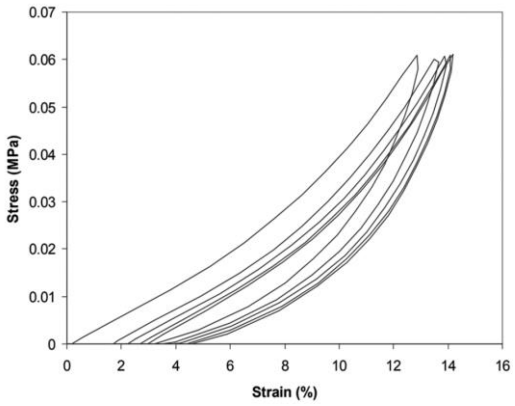

Figure 1.8 Typical preconditioning results of swine skin.
Source: [69].

Because of the phenomena discussed above, the preconditioning step is required for most of the connective tissues consists of elastin and collagen fibers in order to get

repeatable and consistent experiment results. This procedure can properly orient the collagen fibers in the microstructure of skin tissue to its natural alignment, and result in more consistent experimental data [71]. Karimi et al. [29] reported that the preconditioning process can be completed by 10 cycles for the rat skin.

1.6.5 Failure Properties

Failure mechanical properties of skin tissue are commonly tested by *ex-vivo* uniaxial tensile tests. The results of the experiments are remarkably different because of the species of animals, sample locations, and loading directions.

Strain rate is one of the main factors affecting the failure mechanical properties of skin tissue. Dombi [60] did a systematic comparison of a low rate (0.3 /s) and a high rate (60 /s) tensile experiments using the dorsal skin of rats aged 1.5-6 months. The skin tensile strength of high strain rate experiments was significantly increased (two or threefold) compared to low strain rate experiments. It is concluded that the strength of connective soft tissues is the summation of collagen fibers and collagen-matrix interaction [59, 72]. By comparing studies of Annaidh [34] and Gallagher [36], when the former one with a lower strain rate and the latter one with a higher strain rate both done on samples excised from the human back, it can be concluded that higher failure stress and lower failure strain are resulted by increasing strain rate. Ottenio [58] concluded that the UTS (15.965.7, 24.167.1, and 25.868.2MPa in 0.06, 53, and 167/s strain rates, respectively) of the human skin increases with an increased strain rate. However, the contrary result about failure strain was showed that it was independent of the strain rate. Moreover, the same result was reported by Shergold [45] for the failure mechanical properties of porcine skin with various strain rates ranging from 0.004 to 4000/s.

The anisotropic property of skin tissue is another critical factor that noticeably affects the failure properties depending on the loading direction. The uniaxial tensile test is the method mainly used for measuring the property difference between different loading directions [29, 34, 36, 38, 39, 45, 46, 73]. Human skin was one of the most valuable research subjects for many researchers. Annaidh [34] reported the property differences of human back skin between the directions parallel and perpendicular to the Langer's Lines. It is concluded that several properties (initial slope, elastic modulus, failure stretch, strain energy, and UTS) are affected by the loading direction. Ottenio [58] reported the similar experiment results, which is the greatest UTS (28.0 5.7 MPa) found in the parallel samples, the middle value of UTS (22.5 8.2 MPa) found in 45 degrees, and the least UTS found in perpendicular samples (15.6 5.2 MPa) regarding the Langer's lines. The tensile samples were harvested from the left and right sides of human back skin, they have made the conclusion that there is no significant difference for failure properties of human skin, which suggests that the Langer's lines are symmetric about the spine. The authors discussed that for most of the connective soft tissue, the collagen fibers are parallel to the Langer's lines, thus the tensile strength is greater in this direction.

Other researches have been done on porcine skin as well, and the spine as a typical landmark has been widely used for orienting sample cutting. Ankerson [38] obtained the porcine skin samples from back and belly parallel and transverse to the spine and measured the mechanical properties with uniaxial tension in *ex vivo* conditions. The differences of failure strain and failure stress between longitudinal and transverse directions are significant for the belly skin, however, this phenomenon is much more negligible for the skin in back locations. Łagan [44] excised the samples from porcine back skin, and the

samples are cut in two directions, which are parallel and perpendicular to the spine. The result was reported that the UTS for the parallel samples was 10.65 1.75 MPa and 11.87 1.69 MPa for perpendicular samples, and the failure strains were 0.32 0.02 and 0.66 0.05 respectively.

Furthermore, skin location also has a significant influence on some of the failure properties of skin tissue. Annaidh [34] reported that the location of specimens of human back skin has a significant effect on the UTS and the strain energy, but neither on the failure stretch. Żak [40] tested and compared different maximum tensile strength and the slope of the linear region in the stress-strain curve (Young's Modulus) from five different regions on pig body, including nuchal region, dorsal region, lateral abdominal region, cranial abdominal region and thoracic limb region. The results of the maximum tensile strength (2.08 ± 0.25 MPa) and the conventional Young's modulus (5.87 ± 1.52 MPa) were obtained.

1.7 Full-Field Optical Extensometer

1.7.1 Introduction to DIC

Surface deformation measurements of different materials and structures have always been conducted as one of the major topics for experimental solid mechanics [74]. Especially, attention on the experimental biomechanics is extensively attracted by people for the importance of knowing the characterization of biological tissues, organs, and their interactions with biomedical devices [75].

Digital Image Correlation (DIC) has been widely accepted and used for measuring the mechanical properties of biological tissues as a flexible and impacting tool for different scale levels [76, 77]. The population of DIC can be explained by its flexibility, scalability

in a wide range of dimensions, the robustness of its operation principles, and the simplicity of its use [74, 75, 78, 79]. In different literatures, there are other names being used for the same technique [74], such as the digital speckle correlation method (DSCM) [80, 81], texture correlation [82], computer-aided speckle interferometry (CASI) [83, 84], and electronic speckle photography (ESP) [85, 86].

1.7.2 Advantages of DIC

Optical techniques are frequently used for measuring biomedical materials after the 90s. As a comparison, the strain gages have been highly utilized for measuring isotropic materials like metal. However, pointwise measurement of strain gauges can only provide accurate measurements at selected locations, while the other area (between the strain gages) are not investigated [75]. On the other hand, the optical techniques have the following three main features, which are mandatory for the typical measurements of biomedical materials [75]:

a) Full-field measurements. This feature is extremely important for measuring biomedical materials. Because most of the biomaterials are inhomogeneous and anisotropic, the measurement techniques of tracking two points on specimen surface are not practicable and will lead to analytical errors. However, full-field techniques can provide a more comprehensive description of the behavior of biological materials.

b) Contactless measurements. Comparing to the physical extensometers, the optical techniques use a high-resolution camera to capture the displacement, which avoids the interference of the mechanical properties of specimens during the measurements. This feature is particularly critical to deformable materials, such as skin and organs.

c) Relatively, sample preparation on the specimen surface compared to some other measurement techniques, such as strain gauges or FBGS (Fiber Bragg Grating Sensor). Biomedical materials are typical with irregular geometries, which makes the preparation of the regular speckle patterns more difficult and unwise.

For some other full-field optical measurement techniques, such as interferometric techniques (holographic interferometry, speckle interferometry, and electronic speckle pattern interferometry) can be very accurate and sensitive to the small displacement measurements, which is unsuitable for the soft tissue materials with large deformability [78]. Other optical measurement techniques, such as Moiré interferometry requires great efforts to prepare a regular pattern on the surface of the specimen, which is also not suitable for soft tissue materials with irregular geometries [75, 78]. In general, all the techniques mentioned above have their own limitations and found not feasible techniques for measuring soft tissue materials. Digital Image Correlation (DIC) is a promising method, which is able to overcome most of the limitations and can practically be used in the applications of measuring biomedical materials [75, 79].

1.7.3 Preparation for Surface Pattern

The accuracy of DIC measurements is strongly affected by the quality of the speckle pattern [74]. For optimal use of DIC for biological material, the surface of th specimen must have a randomly distributed pattern which can be either natural or artificial. If the tissue sample happens to have a randomly distributed pattern on its surface, such as an intrinsic texture, this sample can be directly exploited by the DIC system.

In most of the cases that the natural texture is not available, the process of applying artificial speckle patterns will be very critical to the accuracy of results, thus the researches about the speckle pattern has attracted attention from many authors [87-89]. There are several techniques to apply the speckle pattern on the biological tissue surface. These consist of the use of powders [90, 91], powder ink mixed into a gelatinous substance [92], and paint (white paint for the background, black paint for speckles) [76, 93, 94]. The

spherical particles can keep the speckle size under control, but, unfortunately, the powder adhesion on specimen surface is not reliable with large deformation, because the particles can be washed out, which will affect the DIC measurements. On the other hand, the paint speckle is also not acceptable for the applications of tissue samples. Because the tissue samples need to remain wet during the testing process, the paint speckles are hard to adhere to tissue. Also, for the large deformability of tissue samples, the paint speckle may crack and potentially affect the testing results. The most critical drawback of paint is that the paint can alter the mechanical and chemical properties of tissue samples [77, 94]. Overall, the speckle pattern on the tissue surface should always satisfy the following requirements:

1. No chemical or mechanical reactions between specimen and speckles;
2. Random distribution, in order to univocally identify each area of the surface of the specimen [75].
3. High contrast to allow the algorithm to capture the correct area on the sample surface.
4. The tissue samples must remain wet and the surface treating process must be done before the specimen dehydrated, otherwise, the tissue material will probably suffer alterations of mechanical properties;
5. The speckle pattern on the tissue samples must be able to withstand large deformation (10%-30%) [76].
6. The speckle size should be in the stochastic pattern and larger than three pixels in diameter to avoid aliasing issues during the correlation however, the size should also be controlled to avoid compromising spatial resolution [91].

1.7.4 Two-Dimensional DIC

Although three-dimensional digital image correlation (3D-DIC) has the advantage of measuring the deformation out of the plane of the sensors on the surface of the specimen by adapting the second camera, two-dimensional digital image correlation (2D-DIC) has been highly adopted to analyze in-plane deformation for tissues that can be simplified to

2D surface. Because of the simplicity and effectivity of the 2D-DIC, it can be said that the 2D-DIC technique is one of the most common ones in optical measurement methods. The 2D-DIC technique has been frequently employed in the applications of measuring tissue materials, such as arteries [79], cartilage [95, 96], hoof horn [97], and skin [94, 98]. Figure 1.9 shows the typical setup for 2D-DIC method, the specimen is clamped on the tensile testing machine and a charge-coupled device (CCD) camera is placed away from the specimen with its optical axis normal to the specimen surface.

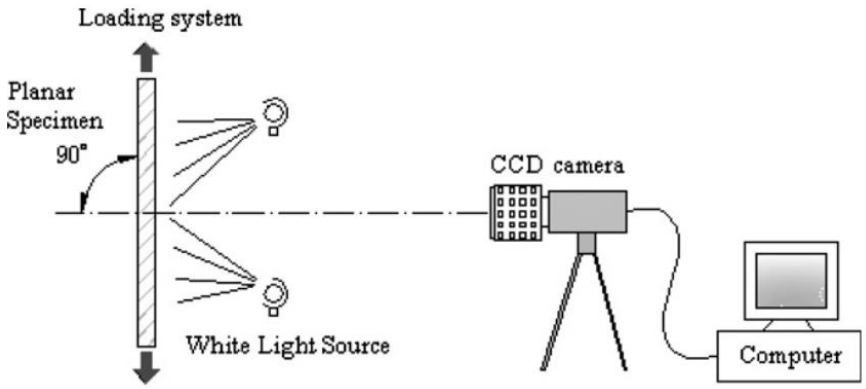

Figure 1.9 Typical optical image acquisition system for 2D DIC method.
Source: [74].

1.7.5 Applications to Soft Tissue

Before the introduction of the DIC technique, most of the strain measurement in soft tissue structures is by the means of physical extensometers, which have physical contact with the sample [99]. This method highly affects the mechanical properties under observation. The optical extensometer as a better alternative was used on the soft tissue samples, which avoid the physical contact (e.g., [100]), but the biggest limitation for the optical extensometer is that the strain field is averaged and any local displacement and strain distribution are neglected. However, these limitations have all been overcome by implementing DIC on

soft tissue. Innumerable applications can benefit from DIC for its robustness and efficiency, especially for the soft tissue materials, such as heart, ligament, arterial, and skin.

Various mechanical properties can be determined with the help of DIC, including Young's modulus, Poisson's Ratio, and residual stress. Sutton used 3D DIC to measure the strain field of mouse carotid artery [79]. Fritz compared the mechanical properties of normal porcine skin and dermal substitute using 2D DIC [101].

1.8 Tissue Constitutive Models

1.8.1 Introduction to the Mathematic Modelling in Soft Biological Material

The mechanical characteristics of soft biological tissues are always considered very complex to predict and describe because of the structural and macroscopic mechanical properties of the soft biological tissue, which can be highlighted into three main characteristics nonlinear behavior, structural non-homogeneous, and mechanical anisotropy [102]. It is possible to make the skin properties more predictable and describable with the help of relevant mathematical than experimental data alone. Furthermore, characterizing the mechanical properties of animal skin is obviously critical for clinical and non-clinical research applications and product development. Being able to connect the experimental data to a mathematical model is vitally important to not only understanding the mechanical properties of skin, but also can be used as a descriptive and predictive tool for surgery simulation, and tissue engineering. Especially nowadays, the numerical analysis tools such as Finite Element Analysis (FEA) and Computational Fluid Dynamics (CFD) are commonly used in academic and industrial applications, which can take better

advantages of constitutive models by capturing particular mechanical features in skin tissues.

1.8.2 Constitutive Models of the Skin

Soft tissues are normally considered as anisotropic material because of their fibrous structure. The mechanical behavior of soft tissue has attracted an increasing amount of attention in the researchers for several decades [103]. In the literature, there are some constitutive models have been developed and conducted to describe the mechanical behavior for soft biological tissues, such as Veronda's model [104], Ogden's model [105], Fung's model [106], Lanir's model [107], Weiss's model [108], HGO model [109], GOH model [109]. Most of the constitutive models can be categorized into two types, which are phenomenological models and structural models. The phenomenological model is a set of mathematical relations that describe the overall relation of stress as a function of strain [106] without considering the mechanical behavior of the individual components in the material or their mutual interactions [104]. The advantages of some of the phenomenological models is mathematically simple and therefore straightforward to apply, however, the parameters in the equations are meaningless to the physical relationship [110]. One may have to change the form of the model for different material types and orientations [39], so this type of models might not be able to accurately represent the material properties under all conditions [25].

The other category consists of structural models, which have meaningful parameters to realistically describe the material properties. This type of models attempts to integrate information on material composition and structure and then correlate this information to mechanical behavior. The parameters in these structural models are more

easily identifiable and many can be measured in the laboratory [25, 111]. Contrasting with phenomenological models, structural models can be a better tool to describe and predict the material properties after appropriate validations. In recent years, various structural models have been proposed to use statistical distributions to describe the structure of collagen fibers in the soft tissues. For the main models that consider fiber dispersion, the reader is referred to Table 1 of [112]. Lanir [107]was the first one that try to approximate the fiber distribution with the Angular Integral (AI) method. This method accounts for each fiber orientation individually, which leads to accurate results, but it is not a practical option for efficient numerical implementations because of the expensive computational cost [113]. The alternative approach, which is known as Generalized-Structural-Tensor (GST) model [109, 114] is simpler to implement and the related computational effort is less [115]. The GST model is also widely implemented in the commercial FEA packages, e.g., ABAQUS.

1.8.3 Isotropic Constitutive Models of the Skin

In this section, the isotropic constitutive models that are commonly used to describe soft biological materials are listed. First, the kinematics is summarized for completeness.

Kinematics

Let $\boldsymbol{\Omega}_0$ be a continuous body in reference configuration, the notation $\boldsymbol{\chi}$ is used for deformation which transforms a material point $\boldsymbol{X} \in \boldsymbol{\Omega}_0$ to the current position $\boldsymbol{x} = \boldsymbol{\chi}(\boldsymbol{X})$ in it's deformed configuration [116]. As is standard, the deformation gradient is obtained as

$$\boldsymbol{F} = \partial \boldsymbol{\chi}(\boldsymbol{X}) / \partial \boldsymbol{X}, \tag{1.1}$$

and the local volume ratio is

$$J(\boldsymbol{X}) = \det(\boldsymbol{F}) > 0. \tag{1.2}$$

The multiplicative decomposition is adopted

$$\boldsymbol{F} = J^{1/3}\boldsymbol{I}\overline{\boldsymbol{F}}, \tag{1.3}$$

and the corresponding right and left Cauchy-Green tensors are given by

$$\boldsymbol{C} = \boldsymbol{F}^T\boldsymbol{F}, \qquad \boldsymbol{b} = \boldsymbol{F}\boldsymbol{F}^T. \tag{1.4}$$

The deformation gradient $\boldsymbol{F}$ can be decomposed into volumetric part $J^{1/3}\boldsymbol{I}$ and distortional part $\overline{\boldsymbol{F}}$, where

$$det(\overline{\boldsymbol{F}}) = 1. \tag{1.5}$$

And the distortional parts of right and left Cauchy-Green tensors, $\overline{\boldsymbol{C}}$ and $\overline{\boldsymbol{b}}$ are given as

$$\overline{\boldsymbol{C}} = J^{-2/3}\boldsymbol{C}, \qquad \overline{\boldsymbol{b}} = J^{-2/3}\boldsymbol{b}. \tag{1.6}$$

In most of the researches, strain invariants are used to avoid explicit relationship between strain energy function and λ_i, because strain energy density must be insensitive to rigid body motion or a transition of coordinates. Three invariants of the right Cauchy-Green deformation tensor C are listed as followings:

$$I_1 = {\lambda_1}^2 + {\lambda_2}^2 + {\lambda_3}^2, \tag{1.7}$$

$$I_2 = {\lambda_1}^2{\lambda_2}^2 + {\lambda_2}^2{\lambda_3}^2 + {\lambda_3}^2{\lambda_1}^2, \tag{1.8}$$

$$I_3 = {\lambda_1}^2{\lambda_2}^2{\lambda_3}^2. \tag{1.9}$$

Neo-Hookean Model

The Neo-Hookean model is an extension of the Hooke's Law for describing incompressible nonlinear and isotropic behavior of material with large deformation such as rubber and soft tissues. The strain energy density function for an incompressible Neo-Hookean material in a three-dimensional description is

$$W = C_1(I_1 - 3), \tag{1.10}$$

where $C_1 = \frac{\mu}{2}$ is a material constant, μ is the shear (or rigidity) modulus of this material which can be experimentally measured. I_1 is the first invariant of the right Cauchy-Green Deformation Tensor C, which can be referred at Equation (1.7).

Mooney – Rivlin Model

An extension of Neo-Hookean model is the Mooney-Rivlin model. This model describes nonlinear, and isotropic material. For the incompressible cases, the strain energy density function can be written as

$$W = C_1(I_1 - 3) + C_2(I_2 - 3), \tag{1.11}$$

where $C_1 = \frac{\mu_1}{2}$ and $C_2 = -\frac{\mu_2}{2}$ are material constants. The shear modulus of this material is $\mu = \mu_1 + \mu_2$. I_1 and I_2 are the first and second invariant of the right Cauchy-Green Deformation Tensor C, which can be referred at Equation (1.7) and (1.8). Note the Mooney – Rivlin model can be degraded to Neo-Hookean model when $C_2 = 0$.

Veronda – Westmann Model

The Veronda – Westmann model are similar as Mooney – Rivlin model using two terms of invariants I_1 and I_2 . However, the strain energy is given by an exponential component, which can better describe the exponential stiffening at the toe region [104]. The strain energy density function can be represented as

$$W = C_1\left(e^{C_2(I_1-3)} - 3\right) + \frac{C_1 C_2}{2}(I_2 - 3), \tag{1.12}$$

where $C_1 = \frac{\mu_1}{2}$ and $C_2 = -\frac{\mu_2}{2}$ are also material constants and the shear modulus is $\mu = \mu_1 - \mu_2$.

Ogden Model

The Ogden model is another hyperelastic material model used to describe non-linear stress-strain behavior of complex materials, such as rubbers, polymers and biomedical materials [105]. This model just like the other models assumes that the material behavior is characterized by a strain energy density function W, from which the stress-strain relationship can be obtained.

$$W(\lambda_1, \lambda_2, \lambda_3) = \sum_{p=1}^{N} \frac{\mu_p}{\alpha_p} \left(\lambda_1^{\alpha_p} + \lambda_2^{\alpha_p} + \lambda_3^{\alpha_p} - 3\right), \tag{1.13}$$

Where N, μ_p, α_p are material constants. With the term N being 3, the material can be described very accurately, however by the meantime, it will also introduce 6 variables to evaluate, μ_1, α_1 and μ_2, α_2 and μ_3, α_3 , which makes the model losing its generality. Thus, one-term Ogden model is more often used to analyze skin tissues [44, 45]. Therefore, the one-term Ogden model is given as

$$W(\lambda_1, \lambda_2, \lambda_3) = \frac{2\mu}{\alpha^2} (\lambda_1^{\alpha} + \lambda_2^{\alpha} + \lambda_3^{\alpha} - 3), \tag{1.14}$$

where μ and α are material constants – shear modulus and strain hardening exponent respectively. Here the shear modulus results from

$$2\mu = \sum_{p=1}^{N} \mu_p \alpha_p. \tag{1.15}$$

Arruda – Boyce Model

Arruda and Boyce [117] introduced a constitutive model to simulate the stress-strain behavior of human skin. This model is based on the statistical mechanics which uses probability theory to study the average behavior of a material with eight polymer chains along the diagonal directions. The strain energy density function is derived from the inverse Langevin function. The first three terms of the constitutive model is given below as:

$$W = \mu\left[\frac{1}{2}(\mathrm{I}_1 - 3) + \frac{1}{20\mathrm{N}}\left(\mathrm{I}_1{}^2 - 9\right) + \frac{11}{1050\mathrm{N}^2}\left(\mathrm{I}_1{}^3 - 27\right) + \cdots\right], \qquad (1.16)$$

where μ is a material constant. For small strains, μ is the shear modulus.

Yeoh Model

Yeoh hyperelastic material model is a phenomenological model describing the deformation of incompressible, nonlinear elastic materials such as rubber. The strain energy density function is shown below [118],

$$\mathrm{W} = \sum_{\mathrm{i}=1}^{\mathrm{N}} \mathrm{C}_\mathrm{i}(\mathrm{I}_1 - 3)^\mathrm{i}, \qquad (1.17)$$

where C_i are material constants, and the quantity $2\mathrm{C}_\mathrm{i}$ can be interpreted as the initial shear modulus for consistency with linear elasticity. When $\mathrm{N} = 1$, the Yeoh model will be reduced to the neo-Hookean model for incompressible material.

Fung Model

Fung model is another famous phenomenological model for skin tissues [106]. The equations are shown below, and

$$W = \frac{1}{2}\left[a(\lambda_1^2 + \lambda_2^2 + \lambda_3^2 - 3) + \mathrm{b}\left(e^{c(\lambda_1^2+\lambda_2^2+\lambda_3^2-3)} - 1\right)\right], \qquad (1.18)$$

where a, b and c are material constants.

For soft material with large strains, the first term in the Equation (1.18) is negligible which simplify the Equation (1.18) into

$$W = \frac{1}{2}\left[C\left(e^{A(\lambda_1^2+\lambda_2^2+\lambda_3^2-3)} - 1\right)\right], \tag{1.19}$$

where C is the shear modulus of the material, and A is a material constant.

Isotropic Constitutive Model Selection

From all the constitutive models listed above, Ogden model is selected to fit and analyze the stress-strain curves. Ogden model has been chosen for its popularity of applications in the soft biological tissues. Moreover, the Ogden model represents power-law based material models, which is one of the most popular approaches to describe soft biological tissues.

1.8.4 Anisotropic Constitutive Models for Skin Tissue

GOH Model

The Gasser-Ogden-Holzapfel (GOH) [109] model is a popular and well-established structural model that provides a foundation to unify the anisotropic properties of soft biological tissues. The strain energy density function W of GOH model can be decomposed additively into two parts, one that is volumetric W_{vol}, and one that is distortional W_{dis}, in the form

$$W = W_{\text{vol}}(J) + \sum_{i=4,6} \bar{W}_{dis}(\bar{\boldsymbol{C}}, \boldsymbol{H}_i), \tag{1.20}$$

where the J is the volume ratio, $\bar{\boldsymbol{C}}$ is distortional left Cauchy-Green tensor. The structure tensor $\boldsymbol{H}_i$ can be presented as

$$\boldsymbol{H}_i = \kappa_i \boldsymbol{I} + (1 - 3\kappa_i)\boldsymbol{a}_{0i} \otimes \boldsymbol{a}_{0i} \quad \text{(i=4,6)}, \tag{1.21}$$

which represent the structure of ith family of fiber with the mean preferred directions along the unit vectors $\boldsymbol{a}_{0i}$ and dispersion parameter κ_i. The volumetric term is taken in the form

$$W_{\text{vol}}(J) = \frac{K}{2}\left(\frac{J^2 - 1}{2} - lnJ\right), \tag{1.22}$$

where K is the bulk modulus. The distortional part can be further decomposed into the isotropic and anisotropic terms.

$$\bar{W}_{dis} = \bar{W}_{\text{iso}}(\bar{\boldsymbol{C}}) + \sum_{i=4,6} \bar{W}_{aniso}(\bar{\boldsymbol{C}}, \boldsymbol{H}_i). \tag{1.23}$$

More specifically, the isotropic part of GOH model is taken as the well-known Neo-Hookean model

$$\bar{W}_{\text{iso}}(\bar{\boldsymbol{C}}) = \frac{\mu}{2}(\bar{I}_1 - 3), \tag{1.24}$$

where μ is the stiffness of the ground substance, and $\bar{I}_1 = tr(\bar{\boldsymbol{C}})$ is the first invariant of the distortional right Cauchy-Green tensor. A key assumption of the GOH model is that the anisotropic behavior is entirely due to two families of collagen fibers. The large deformation behavior of soft biological tissues are commonly approximated by exponential relations as mentioned in [102],

$$\sum_{i=4,6} \bar{W}_{aniso}(\bar{\boldsymbol{C}}, \boldsymbol{H}_i) = \frac{k_{1i}}{2k_{2i}} \sum_{i=4,6} [\exp(\mathrm{k}_{2\mathrm{i}}\langle \bar{E}_i \rangle^2) - 1], \tag{1.25}$$

where

$$\bar{E}_i = \boldsymbol{H}_i : \bar{\boldsymbol{C}} - 1, \tag{1.26}$$

is a Green-Lagrange strain-like quantity which indicates the strain in the mean orientation of the ith family of fibers defined by Holzapfel [112]. Holzapfel [119, 120] also proposed a fundamental hypothesis of fiber-based models which is that the fibers cannot support any compression and would buckle under the smallest compressive load. Following Holzapfel [112], the Macaulay bracket $\langle * \rangle$ is implemented here to switch the contribution of collagen fiber, $k_{1i} > 0$ are stress-like parameter related to stiffness of collagen fiber, and $k_{2i} > 0$ are dimensionless parameter for strain hardening behavior. κ_i are dispersion parameter of fiber. It is commonly assumed that the mechanical properties of two families of fibers are identical [34, 109, 112, 121], which means $k_{11} = k_{12} = k_1$, $k_{21} = k_{22} = k_2$, and $\kappa_1 = \kappa_2 = \kappa$. Therefore, the anisotropic part of GOH model can be further simplified to

$$\bar{W}_{\mathrm{aniso}}(\bar{\boldsymbol{C}}, \boldsymbol{H}_4, \boldsymbol{H}_6) = \frac{\mathrm{k}_1}{2\mathrm{k}_2} \sum_{i=4,6} [\exp\{\mathrm{k}_2\langle \bar{E}_i \rangle^2\} - 1]. \tag{1.27}$$

1.9 Unifying Anisotropic Properties on Sheet Metal

The Gasser-Ogden-Holzapfel (GOH) [109] model is a popular and well-established structural model that provides a foundation to unify the anisotropic properties of soft

biological tissues. In the literature, the structural properties of soft biological tissues are normally determined by measuring the orientation of collagen fibers with histology methods independently and then generalized the fiber orientation information into structural parameters, e.g., mean fiber orientation and the degree of fiber dispersion with statistical techniques [107]. The measured structural parameters are normally imported into the constitutive models as fixed numbers directly to estimate the other model parameters [35]. However, the limitations of the histology analysis, such as tissue frozen in time, the fixation of tissue samples, dehydration, over-processed samples and not direct measurements on the samples in question [122], may potentially introduce the error into the results. Because of the limitations of histology analysis mentioned before, eliminating the needs of independent histology analysis and determining the material properties from mechanical tests alone is demanding. The idea of determining the material properties of thin metal sheets by uniaxial tensile tests from samples in multiple directions applies to soft biological tissues.

The manufacturing of sheet metal via rolling involves plastic deformation because the material experiences a permanent deformation when the load is removed. Understanding the yield standards of sheet metal is critical to mold design optimization and quality control when using sheet metal for production [123, 124]. Owing to the characteristics of the rolling process during manufacturing, sheet metals generally exhibit a significant anisotropy of mechanical properties [125]. This fact leads to a significant mechanical difference between the rolling and transverse directions. The yielding and plastic flow of anisotropic rolled sheet metal is commonly characterized by the Hill yield criterion (e.g., Hill's model [126]) with six anisotropy parameters specifying the state of

anisotropy. The six anisotropy parameters in Hill's yield criteria are normally determined by combining the results of Lankford ratios [126] (plastic strain in width to thickness directions of tensile specimens) measured from uniaxial tensile tests with samples cut in 0°, 45°, and 90° measured from the rolling direction. While anisotropic sheet metal is an entirely different class of materials than those considered here, the idea of combining results of uniaxial tensile tests in different orientations to evaluate the anisotropy of the material and determine the mechanical properties can be adopted to characterize elastic behavior of anisotropic materials, e.g., soft biological tissues.

1.10 Review of Auxetic Material Properties

1.10.1 Materials with Negative Poisson's Ratio

Poisson's ratio is the ratio of lateral contraction to longitudinal expansion. It is a measure of the Poisson's effect, which is the phenomenon that a material tends to compress in the directions perpendicular to the direction of the extension. Conversely, if the material is compressed rather than stretched, the material usually tends to expand in the direction transverse to the direction of compressing. For most of the materials, the Poisson's ratio for them is positive because of the interatomic bonds realign with the deformation in the microscopic view.

Materials with a negative Poisson's ratio have been called with different names, including anti-rubber [127], dilational materials [128], and auxetic materials [129]. Lakes and his group design the first artificial material with negative Poisson's ratio in 1987, a foam with a re-entrant structure [130]. This form has been applied to a seat cushion material

[131]. Some other materials have also known as the auxetic materials, such as knitted nylon fabric [132].

1.10.2 Biological Materials with Negative Poisson's Ratio

There are some researchers reporting that the phenomena of negative Poisson's ratio were found in some biological materials, such as cancellous bone [133], and skins from cats [104] and cows [134]. Lees found the teat skin of cows has negative Poisson's ratio at low strain range. The behavior of the teat skin of cows is more similar to knitted nylon fabric instead of rubber in the uniaxial tests.

CHAPTER 2

EXPERIMENT SETUP AND EXPERIMENTAL DATA ANALYSIS

2.1 Experiment Setup

2.1.1 Material Preparation

Midwest Research Swine (MRS) is a known provider of porcine starting material used by the Medical Device industry to produce tissue engineered products, which results in their established quality control system, porcine breeding procedures, and manufacturing processes. MRS provided porcine skin from a 6 month Male 241 pound American Yorkshire-Landrace-Duroc, which is a traditional material used as a Medical Device starting material. The skin was debristed and the hypodermis was removed per MRS established process. Skin tissue was harvested from the back and neck regions with established templates (see Figure 2.1(A)) by identifying the tail and head respectively. The back specimen measured 42cm tall and 52 cm wide. The neck specimen measured 33 cm tall and 43cm wide. The spine and head were identified for orientation. Skin pieces were pouched, vacuum sealed, and overnight delivered to NJIT for testing, a process consistent with typical Medical Device practices. The tissue size and time needed for testing required freeze storage, which has been used to preserve skin properties [135-137] and has been used previously for porcine tensile testing [138]. Therefore, upon receipt the tissue pouches were frozen in a -80^{o}C freezer for storage. The tissue samples were defrosted over a 24 hour period in a 4 ^{o}C refrigerator prior to testing [139]. A steel rule die was designed and fabricated (Apple Steel Rule Die Co, Springfield, MA) with ASTM Type 5 Tensile samples that are perpendicular to each other (see Figure 2.1(B)). This custom die allows

perpendicular samples to be simultaneously cut from a tissue region. The die was positioned on the porcine skin such that one tensile sample was parallel to the spine and the other perpendicular. Tensile samples were cut utilizing a Tipmann Clicker 700 Die Cutting Press (Tippmann Industrial, Wayne, IN) with 7 tons of cutting pressure. Tensile samples were kept in an isotonic saline solution (Ricca Chemical 0.9% Sodium Chloride) until mechanical testing.

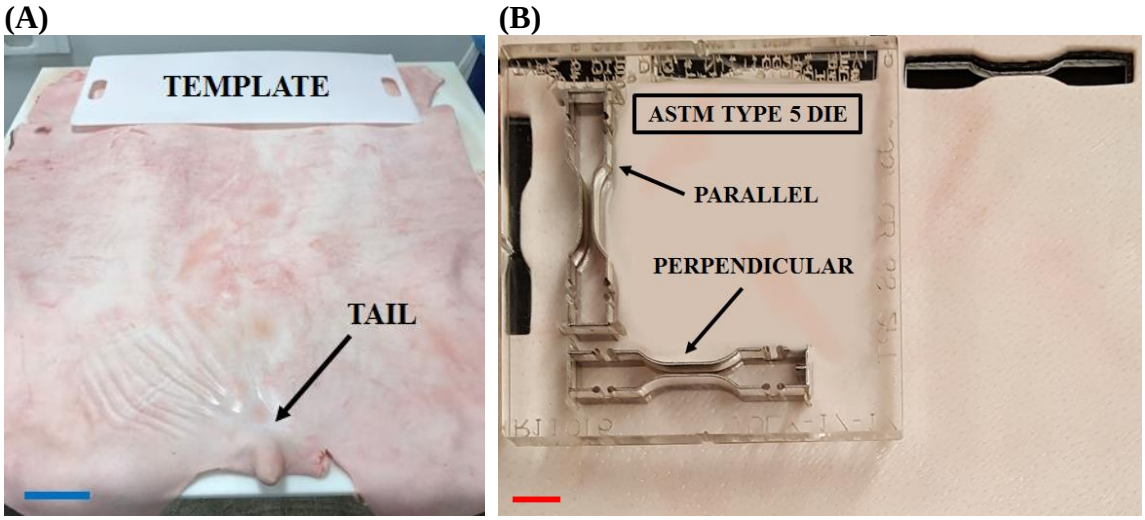

Figure 2.1 (A) Representative image of Porcine Hide with a cutting template. Blue Scale bar is 35 cm, **(B)** Representative image of ASTM Type 5 Tensile Die on tissue that allows the simultaneous cutting of parallel and perpendicular tensile samples. Red Scale bar is 0.375 inches.

A pneumatic die press was used to cut the skin sheets with the standard and custom dies (Figure 2.2). Calculations are conducted for standard and custom dies to ensure proper tonnage and pressure during cutting process. Two platens are purchased and utilized for standard and custom dies respectively.

Figure 2.2 Pneumatic die press for cutting samples with standard and custom dies.

The orientation of skin sheets are indicated by the notches on them. The one notch and two notches indicate head and spine respectively (Figure 2.3 (A)).After the die cutting done, the cut samples were soaked in saline solution and placed in plastic containers with tape that is labeled for each location (Figure 2.3(B)). The saline solution can keep the cut samples from dehydration.

The thickness of skin samples needs to be measured before the tensile experiment, because the thickness would be used to calculate the cross-section area for stress analysis (Figure 2.4 (A)). The Mitutoyo Drop Gauge was used to test the thickness of skin samples. The resolution is 0.00005 inch and accuracy can reach to 0.001 inch. The thicknesses are manually documented on data sheet for future analysis (Figure 2.4 (B)).

(A) **(B)**

Figure 2.3 (A) Left back skin sheet after cut. The notches on the sheet indicates the orientation of the skin sheet, **(B)** Cut samples are placed in the plastic containers with the tapes indicate the locations.

(A) **(B)**

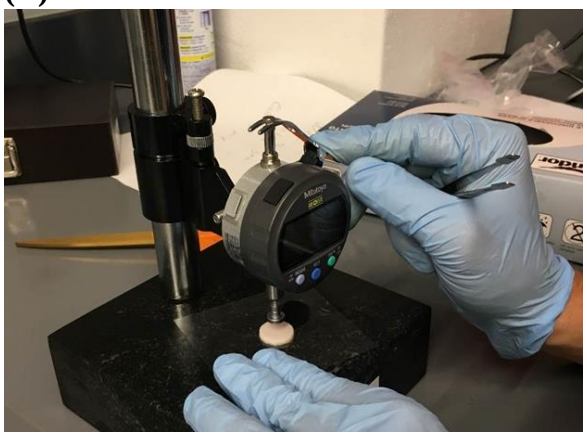

SAMPLE NAME	THICKNESS MIDDLE REDUCED SECTION(in.)	THICKNESS TOP REDUCED SECTION(in.)	THICKNESS BOTTOM REDUCED SECTION(in.)	ORIENTATION	
221	0.064	0.064	0.065	R12 1 Notch	
222	0.055	0.058	0.060	R12 0 Notch	10:53
223	0.046	0.055	0.047	R21 0 Notch	10:57 Skip
224	0.053	0.059	0.056	R21 2 Notch	11:01
225	0.058	0.064	0.065	R21 1 Notch	11:05
226	0.062	0.065	0.062	R22 0 Notch	11:09
227	0.063	0.066	0.062	R22 1 Notch	11:13
228	0.060	0.063	0.062	R22 2 Notch	11:17
229	0.059	0.064	0.059	R31 2 Notch	11:20
230	0.043	0.050	0.054	R31 0 Notch	11:25
231	0.057	0.063	0.057	R31 1 Notch	11:29
232	0.066	0.070	0.066	R32 2 Notch	11:32
233	0.066	0.065	0.066	R32 1 Notch	11:35
234	0.061	0.059	0.063	R32 0 Notch	11:43
235	0.067	0.068	0.071	R3 50	11:46
236	0.068	0.072	0.076	R2 50	11:50
237	0.055	0.055	0.063	R1 50	11:53
238	0.071	0.074	0.071	R1 10	11:59
239	0.066	0.071	0.069	R2 10	12:06
240	0.070	0.074	0.071	R3 10	12:12

Figure 2.4 (A) Mitutoyo Drop Gauge is used to test thickness of skin, **(B)** One example of data sheet for documenting skin thicknesses.

Air Eraser Etching Kit was used to spray the silicon carbide particles onto skin tissues (Figure 2.5(A)). Different grit sizes of silicon carbide and application methods have been explored. The silicon carbide particles have the best adhesivity to the skin tissues, and 100 grit sizes provide the clearest data. After the spraying done, the material preparation is done and ready to be sent to MTS machine for tensile tests. One sample is shown in Figure 2.5 (B).

(A) **(B)**

Figure 2.5 (A) Air Eraser Etching Kit is used to spray particles onto skin tissues **(B)** One skin tissue sample after preparation on the MTS machine.

2.1.2 Uniaxial Tensile Test

MTS machine has been used throughout our entire tensile stretching process (Figure 2.6). The prepared sample is gripped by the upper and lower grippers (Figure 2.5(B)). Before testing begins, a 1-kilo Newton load-cell is installed on the upper gripper (also called crosshead). The load force data and crosshead displacement data are collected by MTS machine and transfer to the software called TW Elite. 50 mm/min stretch velocity was conducted for all the standard tests, which correlates to strain rate. Other two speeds were also used to test the impact of strain rate to the material properties which are 10 mm/min and 100 mm/min (respectively for strain rates). The samples are stretched with this constant strain rate until it breaks (Figure 2.7). There are totally 93 samples has been conducted and ready for analysis.

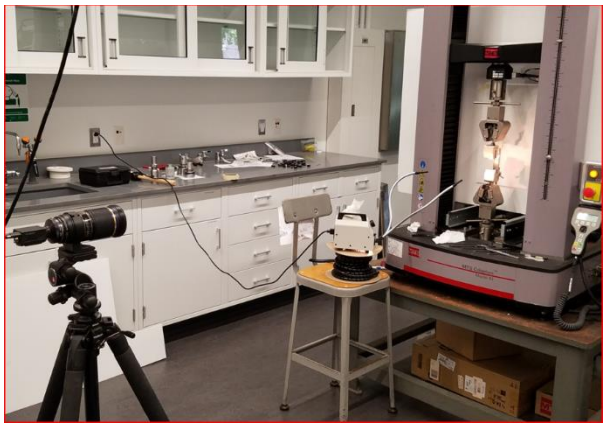

Figure 2.6 MTS system ready for experiment.

(A) **(B)**

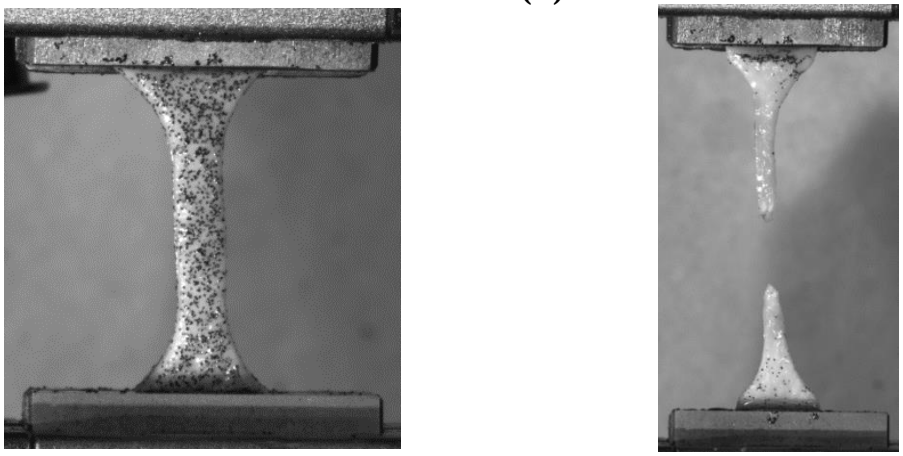

Figure 2.7 Representative image of speckled Type 5 tensile sample, **(A)** The tensile sample of PSSM ready for test prior to loading **(B)** The tensile sample of PSSM at failure

2.1.3 Optical Extensometer Setup

The load force and crosshead displacement are directly collected by MTS machine, and these two data sets are highly used in industrial applications. However, it is reported from literature that the crosshead displacement cannot comprehensively show the real displacements happening on the tissue samples. Thus, the digital image correlation (DIC) becomes necessary for its capability of full-field strain analyzing.

The DIC extensometer to be used is a combination of software, a camera system, and a dedicated PC for file storage and software operation. The camera uses the Point-Grey module, an attached lens, and an adjustable tripod, as seen in Figure 2.8. The camera is to be positioned in a manner that will allow the user to have a full image of the sample when it is elongated, but, also must be close enough to retain a high enough resolution of the speckle pattern. The camera must be centered and leveled using the adjusting knobs on the tripod as well.

The VIC-Snap software is also used with the high-resolution camera to capture a series of pictures during the entire testing process. The camera resolution needs to be adjusted in VIC-Snap appropriately, and the speckle pattern on the screen should be clearly visualized at roughly 850% scale by adjusting lighting and exposure of the lens to create enough contrast as to allow the light and dark pixels to be easily identified. Once this is completed, the camera is not to be moved for the remainder of testing.

Figure 2.8 Camera and Tripod

The acquisition speed is set to allow the camera to capture roughly 100 to 150 images from the start of the test to specimen failure. This will provide a sufficient amount of data to be analyzed. Based on different stretch speed, the acquisition speed needs to be

adjusted accordingly. Table 2.1 shows the acquisition intervals for different stretch speed, and the one used for all the standard samples is 150 ms for 50 mm/min.

Table 2.1 Acquisition Interval for Different Stretch Speed

MTS Crosshead Speed (mm/s)	MTS Crosshead Speed (mm/min)	Acquisition Interval (ms)
0.833	50	150
1.666	100	20
0.166	10	750

2.1.4 DIC Analysis

In order to obtain the real displacement on the tissue sample, a series of images need to be analyzed with dedicated software called VIC-2D. Two pairs of speckles for vertical and horizontal displacements have been selected and the distance between these speckles are measured on the first image. Based on the first image, the software will keep tracking these points and documenting the distances.

Once each sample has an extensometer output file, MATLAB is used to translate the correlation data into a useable format. A specific MATLAB file written for tissue tension test analysis with a 1 kilonewton load cell is used to take the extensometer file and use its data to create a new Excel sheet that displays Force, Crosshead Displacement, Nominal Stress, Stretch, True Strain, Engineering Strain, and Poisson's Ratio. This Excel sheet is named by the sample's numerical designation and is the final product of the data analysis. Once this spreadsheet is generated by MATLAB, the data is interpreted and comparisons are made by graphical methods in Excel. Figure 2.9 shows the extensometer stress-strain curve and crosshead stress-strain curve.

(A) **(B)**

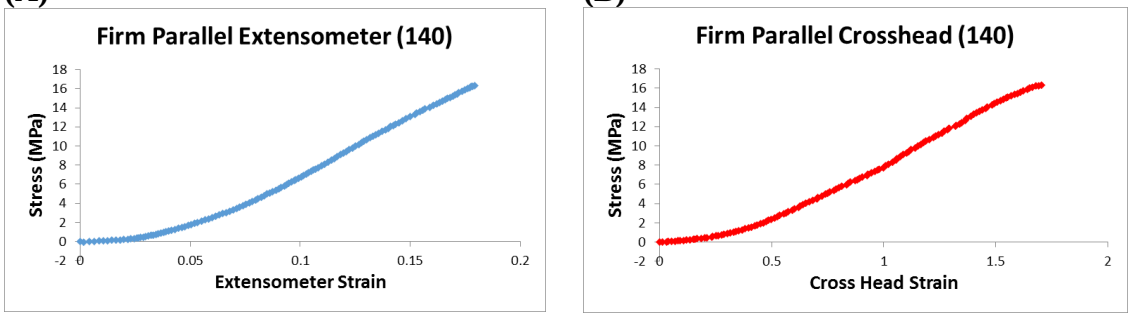

Figure 2.9 (A) Extensometer stress-strain curve for one sample, **(B)** Crosshead stress-strain curve for the same sample.

2.2 Constitutive Modeling

In this section, the Ogden constitutive model [105] is derived. The Ogden model for incompressible, isotropic, hyperelastic solids is widely used for rubber-like material, e.g., skin tissue. The one term Ogden model is used [45], and it can be expressed in terms of principal stretches λ_1, λ_2 and λ_3 as

$$W(\lambda_1, \lambda_2, \lambda_3) = \frac{2\mu}{\alpha^2}(\lambda_1^\alpha + \lambda_2^\alpha + \lambda_3^\alpha - 3), \tag{2.1}$$

where W is the strain energy density per undeformed unit volume, μ is interpreted as the shear modulus under infinitesimal straining, and α is interpreted as a strain hardening exponent [45, 140]. Since the skin tissue is assumed to be an incompressible material,

$$J = \lambda_1 \cdot \lambda_2 \cdot \lambda_3 = 1. \tag{2.2}$$

In addition, the skin tissue is also assumed to be an isotropic material, so under uniaxial tensile conditions, based on Equation (2.3) we have

$$\lambda_2 = \lambda_3 = \lambda_1^{-\frac{1}{2}}. \tag{2.3}$$

The first Piola-Kirchhoff stress tensor is obtained from the strain energy density by

$$P = \frac{\partial W}{\partial F} - pF^{-1} \tag{2.4}$$

where p is Lagrange multiplier enforcing the incompressibility condition. Under uniaxial tensile loading conditions, the stress in lateral and thickness directions are zero, $P_2 = P_3 = 0$. Therefore the principal components of first Piola-Kirchhoff stress tensor can be written as

$$P_1 = \frac{2\mu}{\alpha}\lambda_1^{\alpha-1} - p\lambda_1^{-1} \tag{2.5}$$

$$P_2 = P_3 = \frac{2\mu}{\alpha}\lambda_2^{\alpha-1} - p\lambda_2^{-1} = 0 \tag{2.6}$$

After calculating the pressure term p from Equation (2.6), and substituting it back into Equation (2.5), the nominal tensile stress P can be written in the form

$$P_1 = \frac{2\mu}{\alpha}\left(\lambda^{\alpha-1} - \lambda^{-\frac{\alpha}{2}-1}\right), \tag{2.7}$$

where $\lambda = \lambda_1$ is the tensile stretch. Therefore, Equation (2.7) is the specialized constitutive equation used for stress-stretch analysis.

2.3 Data Analysis

A Matlab (MathWorks, Natick, MA) program was developed for the data analysis. The nominal stress was calculated by taking the force and dividing it by the original cross sectional area of the tensile samples gauge region. The tensile stretch ( ), ratio between the final length and the initial length, was then calculated using DIC. The uniaxial stress-stretch was plotted (Figure 2.10 (A)). The transition point between the toe (initial non-linear) and linear regions of the curve was identified using a Bilinear Fit method [54-56]. The curve was broken up into three zones: toe, linear, and failure [53]. The Transition Point separates the toe and linear regions of the stress-stretch curve. The end of the linear region was identified as 80% of Failure Stress (FS), and an initial guess for the transition point algorithim was taken as 20% FS. The Bilinear Fit was iterated until the transition point did not vary by more than 1%. This resulted in a transition point marking the end of the toe region and beginning of the linear region, a Toe Slope from the linear fit of the toe region, and a Linear Slope from the linear fit of the linear region (Figure 2.10 (B)). The linear fit's quality to the experimental data in the toe and linear region was determined with *an* R^2 *value.*

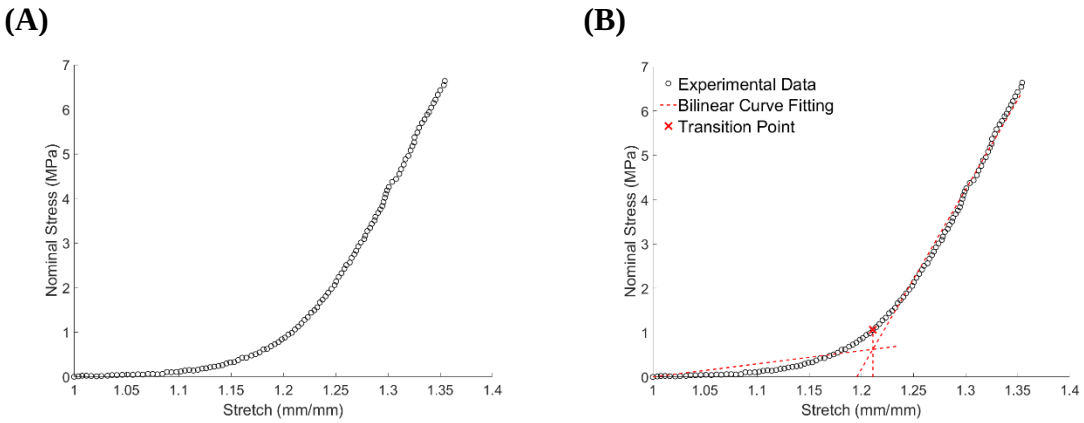

Figure 2.10 (A) Representative tensile curve with clear nonlinear and linear regions. **(B)** Representative figure showing the Bilinear Fit identifying a Transition Point with a linear fit to the Toe and Linear regions respectively.

The material constants of the Ogden model were identified using the *built-in MATLAB function lsqcurvefit* to minimize the objective function:

$$F(u) = \sum_{i=1}^{n} \left(P\,(\lambda_i) - P_i^{exp}(\lambda_i)\right)^2, \tag{2.8}$$

where *P* is the calculated nominal stress from the model at any given $_i$, and P_i^{exp} is the measured stress from experiments, n is the number the sample points in the experimental data, u is vector of unknown material constants to be determined ($u = (\mu, \alpha)$ for Ogden model). The calibration of the Ogden constitutive model was conducted up to 80% FS, which is the full curve encompassing both toe and linear regions. The performance of the Ogden model in describing the experimental data in respective regions (Toe, Linear, Full Curve) is measured by an R-squared value.

Statistical Analysis

All data are presented here as Means ± SE Means. Statistical analysis was conducted with Minitab® Statistical Software package, where significance for all analyses was determined by calculating a probability value (P). Values of $P < 0.05$ were considered to be significant. Tensile samples were classified in four groups: Back Parallel, Back Perpendicular, Neck Parallel, and Neck Perpendicular. The data set was evaluated for normal distribution and homogeneity of variances with an Anderson-Darling normality test and Levene's test respectively. A one-way ANOVA was conducted followed by a Tukey for all measures having equal variance. A Games-Howell post hoc test was used on the Intersection Strain, Linear Region Slope, and to 80% FS measures which had unequal variances. A trending

difference between the Failure Strain measure in the Back Parallel and Back Perpendicular groups was interpreted with a two sample T-Test for information purposes only.

2.4 Results and Discussion

2.4.1 Tensile Curve Fitting

The uniaxial tensile stress-stretch behavior exhibits the classic nonlinear and linear regions (Figure 2.10 (A)). The calibrated Ogden model is able to be fit to the full stress-stretch curve. The fit achieves an R^2 value averaging 0.98 over the study's 67 samples. The fit in the linear region has an average R^2 value of 0.97; however, the fit in the toe region had an R^2 value averaging -11.45. The negative R^2 indicates that the fit is worse than fitting a horizontal line to the respective data. This result suggests that the linear region is driving the fit taking place when the Ogden model is applied to the full curve. The poor fit in the toe region was also noted by Zhou with the Ogden model [140]. Fitting to the full curve does not fully describe the nonlinear toe region. The fitting was reapplied after separating the toe and linear regions with the bilinear curve fit method. Once this method was applied the Ogden model fit the toe region of the curve with an average R^2 value of 0.99 over all samples. Figure 2.10 (A) shows the representative fits of the Ogden on the full curve, Ogden on the toe region, and linear fit on the linear region. The linear region alone had an average R^2 value of 0.99 over all samples. The linear fit in the toe region had an average R^2 of 0.78 over all samples. This suggests that the linear fit may not fully describe the relationships in this toe region. The findings of this work suggests that the tensile curve is best described by separating the nonlinear and linear regions, applying an Ogden model to the toe region, and a linear model in the linear region (Figure 2.10 (B)).

(A) **(B)**

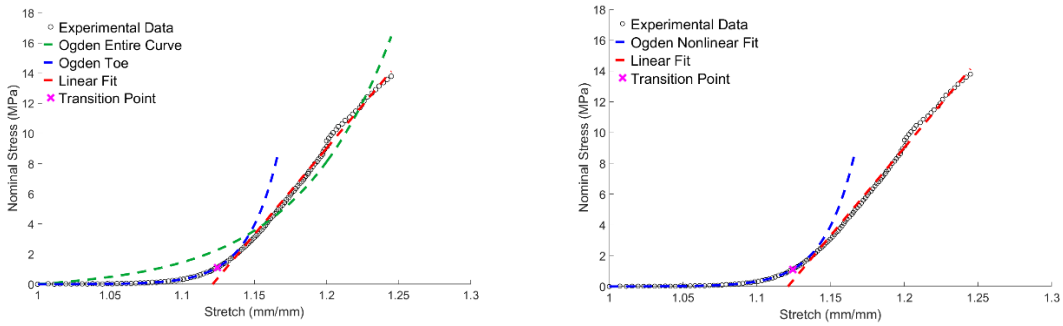

Figure 2.11 (A) Representative figure showing the Ogden model fit to 80% FS. The Toe and Linear regions are not fully captured by a full Ogden fit. Identifying a Transition Point and then conducting an Ogden and Linear fit provides an improved fit in the toe and linear regions respectively, **(B)** Representative figure showing the preferred embodiment to describe the tensile curve an Ogden fit describing the toe region and linear fit for linear region.

2.4.2 Mechanical Parameters Compared to Literature

The Failure Stress determined in the Back and Neck regions (Table 2.2) are in range with other reported studies. Pramudita found that samples from dorsal region parallel to the spine (perpendicular to Langer/Cleavage line) resulted in an ultimate tensile stress of 20.78 MPa. Those perpendicular to the spine (parallel to Langer/Cleavage Line) had an increased Failure Stress of 28.04 MPa [138]. Shergold also reported a maximum stress of 20 MPa at a rate of 0.004/s, 21 MPa at a rate of 0.4/s, and 29 MPa at 40/s (estimated from curves in [45]). Lagan reported an Ultimate Stress perpendicular to the spine in the spine region of an 8 month old pig (breed not described) as 34.13 MPa [44]. Ankersen reported work in 7-8 month old pigs, but no pig breed information was provided. He indicated that back pieces parallel to the spine had ultimate stress of 15 MPa, and those perpendicular to the spine 15.2 MPa [38].

The slope in the linear region (Table 2.2) is also consistent with what has been reported. Pramudita reported in the Dorsal region parallel to the spine 77.72 MPa and

perpendicular 150.53 MPa [138]. Lagan described the slope in the linear region for the spine region for pieces perpendicular to the spine to be 106.79 MPa [44]. No other study has reported measures in the neck region; however, the Failure Stress and slope in the linear region are in alignment with what has been reported in another relatively soft porcine skin regions. Pramudita reported that the ventral region parallel to spine had Ultimate Stress of 16.53 MPa and perpendicular to spine showed an increase to 28.64 MPa [138]. Moreover, Lagan described samples perpendicular to the spine in the abdomen at 6.09 MPa. Ankersen showed that belly pieces parallel to the spine ranged from 8 to 30 MPa and perpendicular to the spine 5 to 8 MPa [38]. Pramudita reported the slope in the linear region of in the ventral region to be 79.05 MPa parallel to the Spine and 113.10 MPa perpendicular to the Spine [138]. Lagan described perpendicular samples in the abdomen region to have a linear region slope of 7.55 MPa [44].

The Failure Stretch determined in the Back and Neck regions (Table 2.2) are also in range with other reported studies. Pramudita reported in the dorsal region of a rupture strain parallel to the spine of 0.37 and perpendicular 0.25 [138]. Ankersen reported back pieces parallel to the spine had Failure Stretch of 1.42, and those perpendicular to the spine 1.37 [38]. Any differences seen could be a result of different breeds and ages of pigs. Not all previous work reported the breed and a number of studies did not report the age of the animals from which the skin was extracted.

2.4.3 Ogden Material Constants Compared to Literature

The Ogden constitutive model was calibrated to the full curve and the toe region alone. The Ogden model had been previously used on porcine skin [44, 45, 140, 141] applied to full stress stretch curve. The Ogden model has not previously been applied to the Toe

Region alone on porcine skin. The Ogden parameters, μ and α, are interpreted as the shear modulus and strain hardening exponent, respectively [45, 140]. The measured parameters are shown in Table 2.2 . The μ and α on the full curve from the back and neck regions are comparable to those reported by others on porcine skin. The strain hardening exponent α is considered to be largely strain rate independent [45]. Shergold reported an α value of 12 on pig skin [45]. Lim had a similar finding with an α value of 11 (parallel to spine) and 7 (perpendicular to spine) in testing at various rates [141]. Lagan reported an α value dependent on location of 7.7 (abdomen) and 27.4 (spine) both from specimens that were perpendicular to the spine [44]. Shergold reported a μ that ranged from 0.4 MPa to 1.2 MPa at a strain rate of 0.004 s^{-1} and 0.4 s^{-1} respectively [45]. Lim had a μ value of 10 kPa (parallel to spine) and 3 kPa (perpendicular to spine) in testing at 0.005 s^{-1} and 20 kPa (parallel to spine) and 8 kPa (perpendicular to spine) in testing at 0.5 s^{-1} [141]. Lagan reported a value of 3.58 MPa on spine samples and 0.057 MPa for abdomen [44] at a strain rate of 0.002 s^{-1}. The differences seen again can be attributed to the pig breed, sample locations, and the strain measurement technique.

2.4.4 Back Region Comparison

Table 2.2 summarizes the experimental results in the back region. Figure 2.12 shows a representative Stress-Stretch curve for both the back and neck regions of the porcine skin. Curves for the parallel and perpendicular to the spine directions are shown. The thickness of the parallel and perpendicular tensile samples showed no significant difference in the back group (Figure 2.13 (A)). The Failure Stress was significantly different between the perpendicular and parallel groups in the Back (Figure 2.13 (B)), where the Perpendicular group had a 34% higher failure stress. In addition, the Failure Strain was not significantly

different between the parallel and perpendicular groups (Figure 2.14 (A)). The back parallel and perpendicular; however, appear to be trending towards significance. When a two tail t-test is conducted just between the parallel and perpendicular groups we do see a significant difference where the parallel tensile samples had a failure strain that was 30 % greater than the perpendicular sample. This finding is also consistent with Pramudita's findings that tensile samples in the direction of the Langer Lines elongate more than those that are parallel [138]. An increase in the number of samples may also demonstrate significance. The intersection strain provides an index of the length of the toe region. The intersection strain demonstrated a significant difference, where the parallel tensile samples had a strain that was 69% greater (Figure 2.14 (B)) than the perpendicular group.

The toe region slope was also significantly different between the parallel and perpendicular groups, where the perpendicular tensile samples were 73% greater than the parallel group (Figure 2.15 (A)). The linear region slope also demonstrated a significant difference where the perpendicular group was 88% greater than the parallel tensile samples (Figure 2.15 (B)). These findings are consistent with what Pramudita demonstrated in tensile properties from samples taken parallel and perpendicular to the spine [138]. Pramudita demonstrated significantly higher ultimate stress and Linear Slope from samples from perpendicular samples compared to parallel samples. This was also marked with a significant decrease in the rupture strain from parallel to perpendicular samples. This finding is also consistent with the increase seen in human back tissue, where Annaidh also found these directional differences in skin samples where the Ultimate Tensile Stress, Linear Slope, and initial slope were all higher in samples that were parallel as compared to perpendicular to the Langer lines [34]. This was also met with a lower failure stretch in

parallel samples in comparison to perpendicular ones. Ankersen found the opposite in the belly region of pig skin, where he found samples parallel to the spine had higher tensile properties [38].

The material constants for the Ogden model fit to the full curve demonstrated a significant difference between the parallel and perpendicular groups (Figure 2.16). The shear modulus, μ in the perpendicular group was 99% greater than the parallel group (Figure 2.16 (A)). The strain hardening exponent, α in the perpendicular group was not significantly different than the parallel group (Figure 2.16 (B)). The material constants for the Ogden model fit to the toe region demonstrated a significant difference between the parallel and perpendicular groups for both μ and α (Figure 2.17). The shear modulus μ in the perpendicular group was 65% greater than the parallel group (Figure 2.17 (A)). The strain hardening exponent, α in the perpendicular group was 27% greater than the parallel group (Figure 2.17 (B)). The Ogden model calibration to the toe region provides a better characterization of the uniaxial tensile behavior in that region. This is an example of where calibrating to the full curve may lose the ability to determine key differences taking place in the toe region. Lim also found a difference between the Ogden parameters of parallel and perpendicular to the spine groups. His samples were from the belly region of a 9 month old animal, where he found Ogden parameters to be higher in the parallel as opposed to perpendicular group [141].

2.4.5 Neck Region Comparison

Table 2.2 summarizes the experimental results in the neck region. The thickness of the parallel and perpendicular tensile samples showed no significant difference in the neck group (Figure 2.13 (A)). The representative stress-stretch behavior for the neck region

shown in Figure 2.12 interestingly shows further variation that can be described. The uniaxial tensile response of the Neck pieces varies and fall under three groups, where the parallel and perpendicular samples demonstrate a similar behavior (Figure 2.18 (A)), the perpendicular appears stiffer then the parallel samples (Figure 2.18(B)), or the perpendicular appears more compliant then the parallel samples (Figure 2.18 (C)). The data analysis tells a similar story to the representative curves, where on average the neck region behaves isotropiclly. The Failure Stress was not significantly different between the perpendicular and parallel groups in the Neck (Figure 2.13 (B)). The Toe Region slope was also not significantly different between the parallel and perpendicular groups (Figure 2.15 (A)). The Linear Region slope also did not demonstrate a significant difference (Figure 2.15 (B)). There are no reported measures on the neck region in the literature; however, Ankersen also reported regions where he did not see differences between ultimate stress measured parallel and perpendicular to the spine [38]. Interestingly, he found this in the back region of the pig samples he measured. In addition, the Failure Strain (Figure 2.14 (A)) and Intersection Strain (Figure 2.14 (B)) were also not significantly different between the parallel and perpendicular groups. The material parameters for the Ogden model did not demonstrate a significant difference between the parallel and perpendicular groups for the full curve (Figure 2.16) or the toe region alone (Figure 2.17). The variation across the neck region results on average in properties that are independent of direction (isotropic). Further experimentation on more samples from a number of procurements would have to be conducted to characterize the potential location dependent properties.

2.4.6 Back and Neck Region Comparison

The thickness was significantly different between the back and neck regardless of orientation (Figure 2.13 (A)). This significant difference could be a result from the development of the skin under natural loading as the animal grows. The Failure Stress (Figure 2.13 (B)) was also significantly different between the back and neck where the back perpendicular samples were 88% and 74% greater than both the parallel and perpendicular neck pieces respectively. The parallel back samples were significantly greater than the neck parallel pieces by 40%, but not significantly different to the neck perpendicular group. In addition, the Failure Strain was significantly different between the back perpendicular and neck groups (Figure 2.14 (A)), where the neck parallel and perpendicular tensile samples had a failure strain that was respectively 62% and 54% greater than the back perpendicular group. There is no published work on the Neck Region; however, there are comparisons to other porcine tissue zones. Pramudita found location differences between the dorsal and ventral regions [138]. Lagan found a similar result between his spine and abdomen groups [44]. Ankersen saw these differences between his back and belly specimens [38]. The Intersection Strain was also significantly different between the back perpendicular and neck groups (Figure 2.14 (B)), where the neck parallel and perpendicular tensile samples were respectively 165% and 117% greater than the back perpendicular group.

The Toe Region Slope demonstrated significant difference between the back and neck regions (Figure 2.15 (A)). The back perpendicular group was 327% and 241% greater than the neck in the parallel and perpendicular tensile samples respectively. The back parallel group was only significantly greater than the neck parallel, and was 146% higher.

The Linear Region Slope also demonstrated significant difference between the back and neck regions (Figure 2.15 (B)). The back perpendicular group was 214% and 148% greater than the neck in the parallel and perpendicular tensile samples respectively. The back parallel group was only significantly greater than the neck parallel, and was 67% higher.

The Ogden model calibration to the full curve also demonstrated a significant difference between the back and neck regions. The shear modulus to 80% FS showed a significant difference (Figure 2.16 (A)) whereas the strain hardening exponent to 80% FS did not (Figure 2.16 (B)). The shear modulus μ to 80% FS for the Back Parallel pieces were 125% and 94% greater than the neck in the parallel and perpendicular tensile samples respectively. The shear modulus μ to 80% FS for the Back Perpendicular pieces were 348% and 286% greater than the neck in the parallel and perpendicular tensile samples respectively. The Ogden model calibration to the toe region also demonstrated a significant difference between the back perpendicular and neck regions. The back perpendicular shear modulus μ Toe Region was 333% and 241% greater than the neck in the parallel and perpendicular tensile samples respectively (Figure 2.17 (A)). The back perpendicular strain hardening exponent α Toe Region was 42% and 35% greater than the neck in the parallel and perpendicular tensile samples respectively (Figure 2.17 (B)).

Table 2.2 Tensile Properties (Average ± SE)

	BACK		NECK	
	PARALLEL	**PERPENDICULAR**	**PARALLEL**	**PERPENDICULAR**
MEDIAN THICKNESS (INCHES)	0.095±0.001	0.097±0.001	0.061±0.001	0.059±0.001
FAILURE STRESS (MPa)	20.37±1.02	27.38±1.35	14.54±1.51	15.71±1.73
FAILURE STRAIN	0.38±0.02	0.29±0.03	0.48±0.04	0.45±0.04
INTERSECTION STRAIN	0.096±0.012	0.057±0.003	0.150±0.026	0.123±0.017
TOE SLOPE (MPa)	16.86±1.94	29.22±3.23	6.85±1.31	8.57±2.01
LINEAR SLOPE (MPa)	75.41±4.17	141.74±14.45	45.15±5.21	57.13±8.62
TOE (MPa)	2.61±0.40	4.29±0.31	0.99±0.31	1.26±0.46
TOE	38.94±2.71	49.63±2.70	34.86±3.39	36.80±2.46
to 80% FS (MPa)	10.19±1.06	20.28±1.94	4.53±1.18	5.25±1.15
to 80% FS	10.24±0.70	11.39±0.87	12.38±1.79	11.80±1.71
NUMBER OF SAMPLES (N)	21	17	16	13

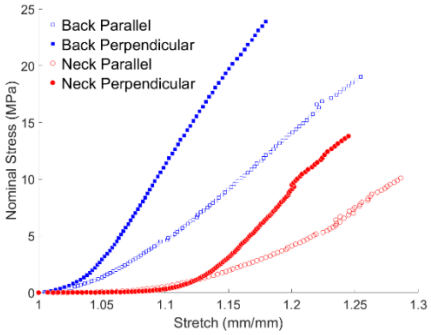

Figure 2.12 Representative figure showing the Stress-Stretch curves in different orientations for the back and neck regions.

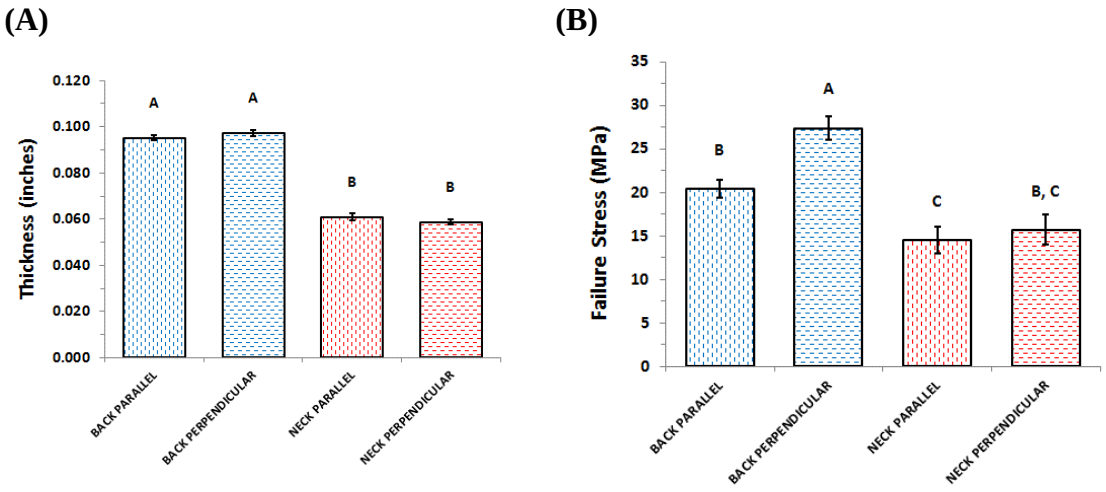

Figure 2.13 (A) The average median thickness of tensile samples from the back and neck regions.
(B) The average failure stress of tensile samples from the back and neck regions. Error bars shown are SE. Means that do not share a letter are significantly different.

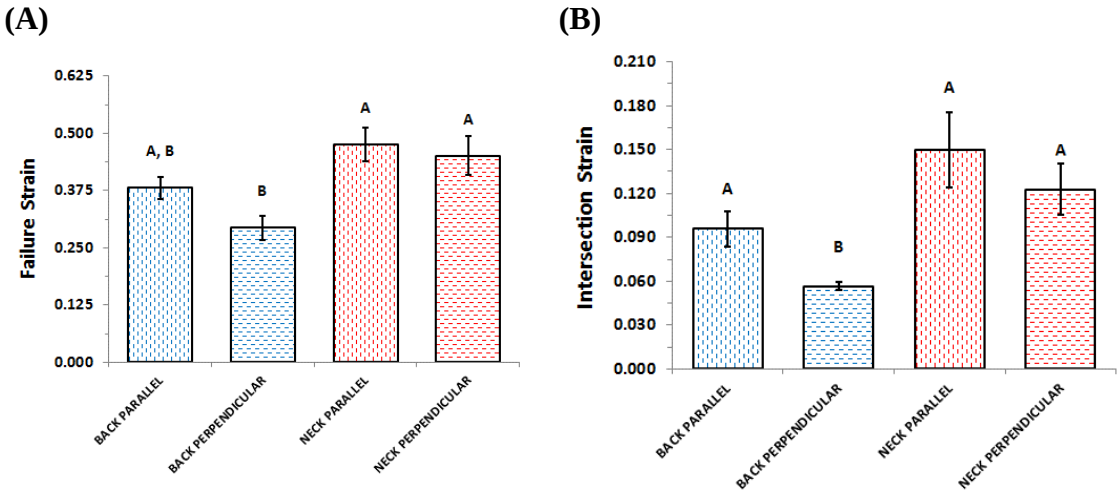

Figure 2.14 (A) The average failure strain of tensile samples from the back and neck regions,
(B) The average intersection strain of tensile samples from the back and neck regions. Error bars shown are SE. Means that do not share a letter are significantly different.

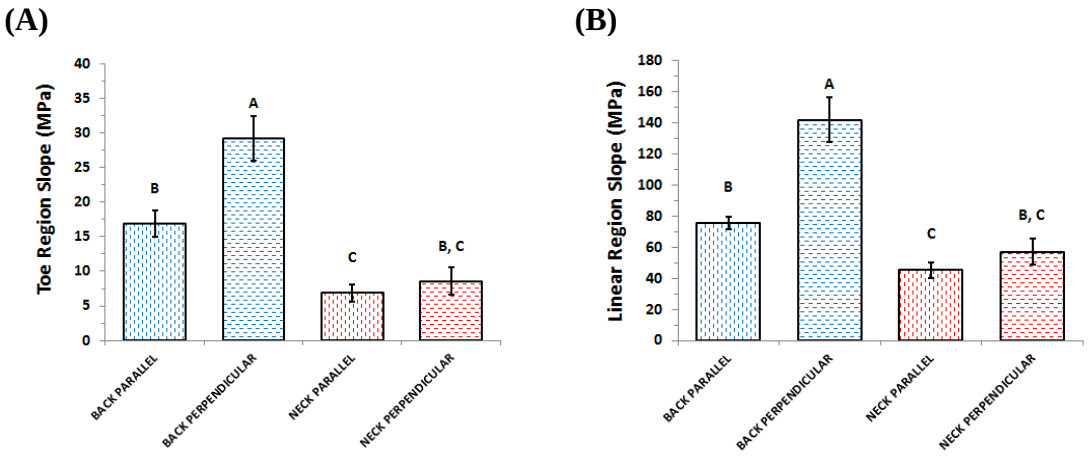

Figure 2.15 (A) The average toe region slope of tensile samples from the back and neck regions,
(B) The average linear region slope of tensile samples from the back and neck regions. Error bars shown are SE. Means that do not share a letter are significantly different.

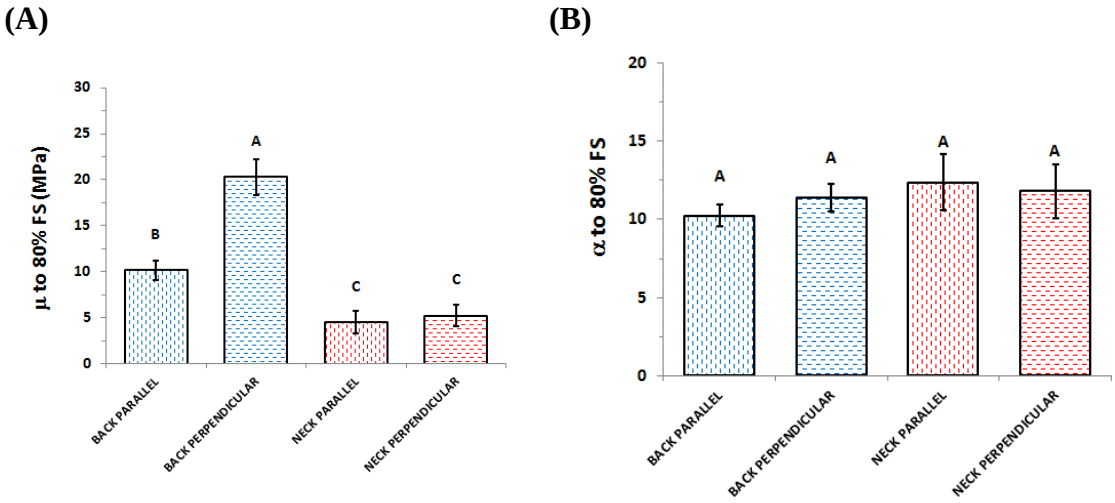

Figure 2.16 (A) The average from the Ogden Model fit to 80% Failures Strain (FS) of tensile samples from the back and neck regions.
(B) The average from the Ogden Model fit to 80% FS of tensile samples from the back and neck regions. Error bars shown are SE. Means that do not share a letter are significantly different.

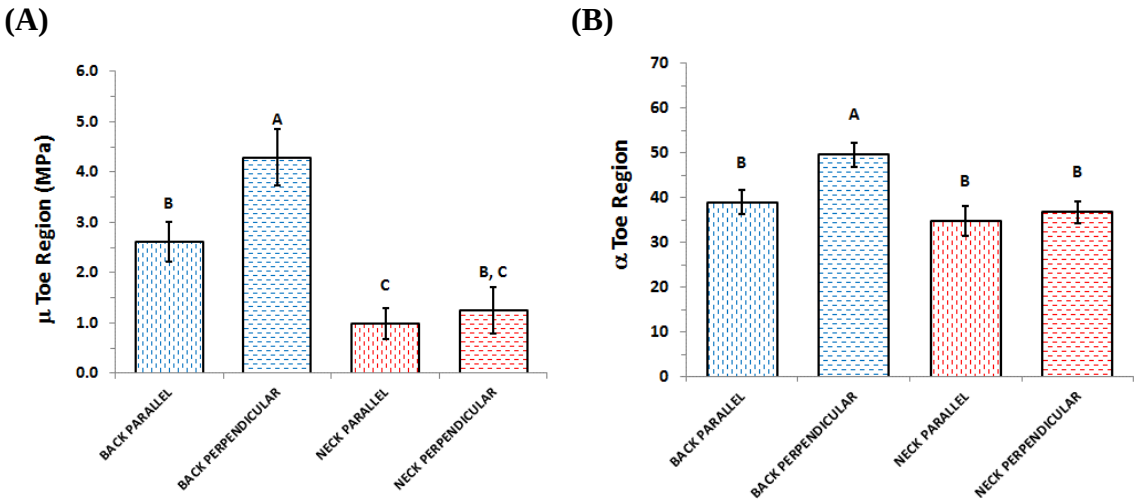

Figure 2.17 (A) The average from the Ogden Model fit in the toe region of tensile samples from the back and neck regions. **(B)** The average from the Ogden Model fit in the toe region of tensile samples from the back and neck regions. Error bars shown are SE. Means that do not share a letter are significantly different.

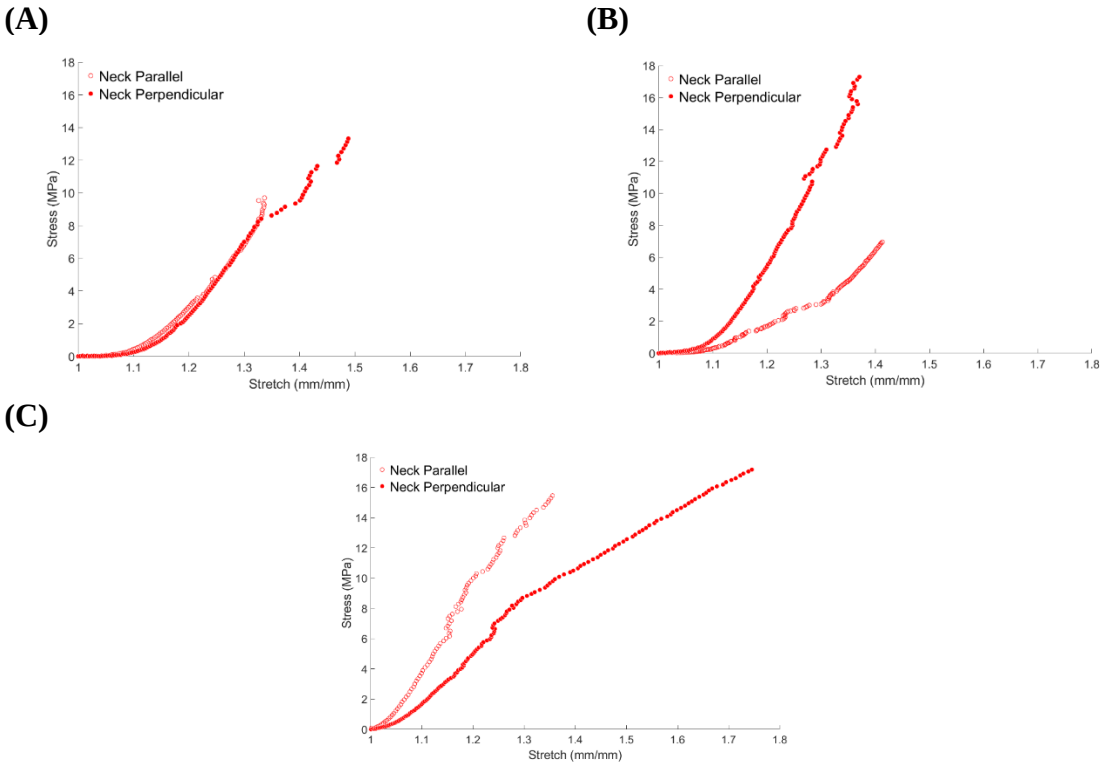

Figure 2.18 Stress stretch responses of tensile samples from the neck region demonstrating, **(A)** A similar response, **(B)** The perpendicular proceeding the parallel, **(C)** the perpendicular following the parallel.

CHAPTER 3

MICROSTRUCTURAL ARRANGEMENT DETERMINATION

3.1 Proposed Approach

The Gasser-Ogden-Holzepfel (GOH) structural model was explored to unify the tissue's directional properties. The GOH model requires that the microstructural element's (e.g., collagen fiber) arrangement within the macroscopic tissue is known beforehand. In the literature this is accomplished through histological measurements on the tissue itself. This requirement limits the ability of the GOH model to be used in the real time analysis of experimental work, which is needed in both academia and the tissue engineering industry. A method was developed to determine the microstructural arrangement (angle and dispersion) by utilizing the mechanical response at two orientations. This developed Microstructural Arrangement Determination Method (MADM) was verified by reproducing a GOH ABAQUS model from the literature. MADM was then applied to porcine skin experimental data, revealing a potential limitation of the GOH model in its treatment of transverse strain.

There is a sheet of soft biological tissue as shown in Figure 3.1, and it is assumed that the mechanical properties and the fiber structure are identical throughout the material sheet. Soft biological materials are also normally assumed to have no collagen fiber out of plane (collagen fiber only in the 1-2 plane), because the majority of collagen fibers in many (collagenous) soft connective tissues lies parallel to the surface as indicated by Holzapfel [119] and confirmed by Annaidh [34] with histology analysis. Therefore, this sheet of material is under plane stress such that the only non-zero stress components act in 1-2 plane only. Soft biological tissues are also commonly assumed to be incompressible or nearly

incompressible because of the high content of water in the material [108]. The in-plane distribution of collagen fibers in soft biological tissues are normally grouped into two families [109], and the collagen fibers are also found to be symmetrically distributed about a mean fiber orientation (see Figure 3.1) [114, 120].

The MADM approach is verified with the material settings in Gasser's paper [109] for the dissected adventitial layer. The circumferential direction is specifically defined as the "*Reference Direction".* Three uniaxial tensile samples are cut relative to the *Reference Direction* at 0 degrees, 45 degrees and 90 degrees which are named "*Parallel Specimen*", "*45 ° Specimen*" and "*Perpendicular Specimen*". $\boldsymbol{a}_{04}$ and $\boldsymbol{a}_{06}$ indicate the mean orientations of two families of fibers in the reference configuration with the collagen fiber dispersion (see Figure 3.1). Further, it is assumed that the two families of collagen fibers are symmetric about the *Reference Direction* with the angle of γ [34]. The parallel and perpendicular specimens are utilized to estimate the mechanical and structural properties, and 45° specimen is used for validating the estimated parameters of GOH model.

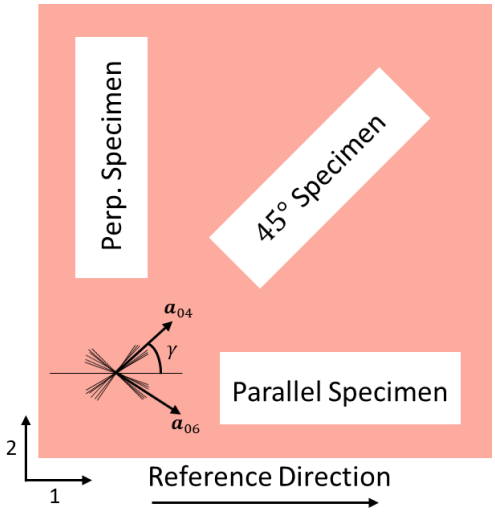

Figure 3.1 A soft biological tissue block with two embedded families of collagen fibers with the mean fiber orientations a_{04} and a_{06} respectively. The parallel, perpendicular and 45° specimens for the tensile tests are cut from the block.

Using the material parameters (Table 3.1) of GOH model given from Gasser's paper [109], a set of finite element simulations are conducted on parallel and perpendicular specimens using the commercial software package ABAQUS to generate three sets of data which are tensile stretch, transverse stretch and tensile stress. The generated stress-stretch curves for parallel and perpendicular specimens are shown in Figure 3.2. The GOH model is calibrated using the combination of the stress-stretch simulation data from parallel and perpendicular simulations to get the estimated material parameters by constrained least-square method. The constrained least-square method is the regular least-square method finding the minimum least-square error with constraint functions need to be satisfied at the mean time. The constraint functions constrain the tangent stiffness evaluated from model parameters to be equivalent to the actual slope of the curve in the toe and linear regions (see Figure 3.3). With this constraint least-square method, the best fitting results can be ensured at the critical toe and linear regions.

Table 3.1 Material Parameters from Gasser's Paper [109].

	Mechanical Properties			Structural Properties	
	$\mu\ (kPa)$	$k_1\ (kPa)$	k_2	$\gamma\ (\circ)$	κ
Gasser [109]	7.64	996.6	524.6	49.98	0.167

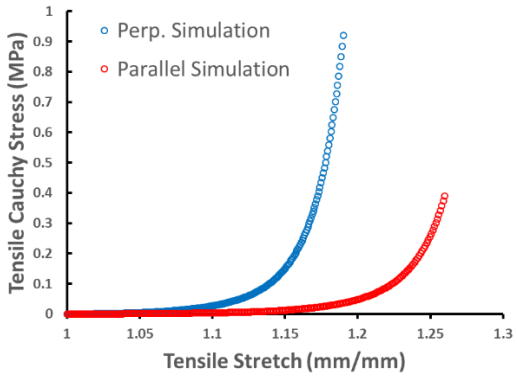

Figure 3.2 Stress-stretch curves for parallel and perpendicular samples obtained from ABAQUS simulations using the material parameters given in Table 3.1.

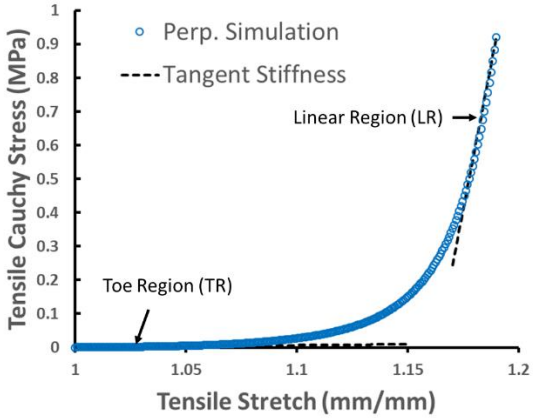

Figure 3.3 Stress-stretch curve of perpendicular sample with tangent stiffness in the toe and linear regions.

It will demonstrate the feasibility of combining the mechanical tests of parallel and perpendicular samples alone to estimate the mechanical properties and material structure without any pre-known fiber structural information. The estimated parameters are brought back into the constitutive model to compare to the generated simulation stress-stretch data from 45° specimen. This will demonstrate the feasibility of validating the estimated model parameters with 45° specimen.

3.2 Constitutive Model

The Gasser-Ogden-Holzapfel (GOH) model is a well-known continuum level constitutive model, based on the underlying structure, developed to capture the behavior of soft biological tissue, e.g., arterial tissue [109], and widely implemented in other classes of tissue [34, 142]. In this section, the continuum framework of GOH model is summarized for completeness.

3.2.1 Kinematics

Let $\boldsymbol{\Omega}_0$ be a continuous body in reference configuration, the notation $\boldsymbol{\chi}$ is used for deformation which transforms a material point $\boldsymbol{X} \in \boldsymbol{\Omega}_0$ to the current position $\boldsymbol{x} = \boldsymbol{\chi}(\boldsymbol{X})$ in it's deformed configuration [116]. As is standard, the deformation gradient is obtained as

$$\boldsymbol{F} = \partial \boldsymbol{\chi}(\boldsymbol{X}) / \partial \boldsymbol{X}, \tag{3.1}$$

and the local volume ratio is

$$J(\boldsymbol{X}) = \det(\boldsymbol{F}) > 0. \tag{3.2}$$

The multiplicative decomposition is adopted

$$\boldsymbol{F} = J^{1/3} \boldsymbol{I} \overline{\boldsymbol{F}}, \tag{3.3}$$

to decompose deformation gradient $\boldsymbol{F}$ into volumetric part $J^{1/3}\boldsymbol{I}$ and distortional part $\overline{\boldsymbol{F}}$, where

$$det(\overline{\boldsymbol{F}}) = 1. \tag{3.4}$$

The corresponding right and left Cauchy-Green tensors are given by

$$\boldsymbol{C} = \boldsymbol{F}^T\boldsymbol{F}, \qquad \boldsymbol{b} = \boldsymbol{F}\boldsymbol{F}^T. \tag{3.5}$$

And the distortional parts of right and left Cauchy-Green tensors, $\overline{\boldsymbol{C}}$ and $\overline{\boldsymbol{b}}$ are given as

$$\overline{\boldsymbol{C}} = J^{-2/3}\boldsymbol{C}, \qquad \overline{\boldsymbol{b}} = J^{-2/3}\boldsymbol{b}. \tag{3.6}$$

3.2.2 Strain Energy Density Function of GOH Model

The strain energy density function W of GOH model [109] can be decomposed additively into two parts, one that is volumetric W_{vol}, and one that is distortional W_{dis}, in the form

$$W = W_{\text{vol}}(J) + \sum_{i=4,6} \bar{W}_{dis}(\overline{\boldsymbol{C}}, \boldsymbol{H}_i), \tag{3.7}$$

where the J is the volume ratio, $\overline{\boldsymbol{C}}$ is distortional left Cauchy-Green tensor. The structure tensor $\boldsymbol{H}_i$ can be presented as

$$\boldsymbol{H}_i = \kappa_i \boldsymbol{I} + (1 - 3\kappa_i)\boldsymbol{a}_{0i}\otimes\boldsymbol{a}_{0i} \qquad \text{(i=4,6)}, \tag{3.8}$$

which represent the structure of ith family of fiber with the mean preferred directions along the unit vectors $\boldsymbol{a}_{0i}$ and dispersion parameter κ_i. (See Figure 3.1)

Here you should remind me about all those terms in this equation. The volumetric term is taken in the form

$$W_{\text{vol}}(J) = \frac{K}{2}\left(\frac{J^2-1}{2} - lnJ\right), \tag{3.9}$$

where K is the bulk modulus. The distortional part can be further decomposed into the isotropic and anisotropic terms.

$$\bar{W}_{dis} = \bar{W}_{\text{iso}}(\bar{\boldsymbol{C}}) + \sum_{i=4,6} \bar{W}_{aniso}(\bar{\boldsymbol{C}}, \boldsymbol{H}_i). \tag{3.10}$$

More specifically, the isotropic part of GOH model is taken as the well-known Neo-Hookean model

$$\bar{W}_{\text{iso}}(\bar{\boldsymbol{C}}) = \frac{\mu}{2}(\bar{I}_1 - 3), \tag{3.11}$$

where μ is the stiffness of the ground substance, and $\bar{I}_1 = tr(\bar{\boldsymbol{C}})$ is the first invariant of the distortional right Cauchy-Green tensor. A key assumption of the GOH model is that the anisotropic behavior is entirely due to two families of collagen fibers. The large deformation behavior of soft biological tissues are commonly approximated by exponential relations as mentioned by Limbert [102],

$$\sum_{i=4,6} \bar{W}_{aniso}(\bar{\boldsymbol{C}}, \boldsymbol{H}_i) = \frac{k_{1i}}{2k_{2i}} \sum_{i=4,6} [\exp(\mathrm{k}_{2\mathrm{i}}\langle \bar{E}_i \rangle^2) - 1], \tag{3.12}$$

where

$$\bar{E}_i = \boldsymbol{H}_i : \bar{\boldsymbol{C}} - 1, \tag{3.13}$$

is a Green-Lagrange strain-like quantity which indicates the strain in the mean orientation of the ith family of fibers defined by Holzapfel [112]. Holzapfel [119, 120] also proposed a fundamental hypothesis of fiber-based models which is that the fibers cannot support any compression and would buckle under the smallest compressive load. Following Holzapfel [112], the Macaulay bracket $\langle * \rangle$ is implemented here to switch the contribution of collagen fiber, $k_{1i} > 0$ are stress-like parameter related to stiffness of collagen fiber, and $k_{2i} > 0$ are dimensionless parameter for strain hardening behavior. κ_i are dispersion parameter of fiber. It is commonly assumed that the mechanical properties of two families of fibers are identical [34, 109, 112, 121], which means $k_{11} = k_{12} = k_1$, $k_{21} = k_{22} = k_2$, and $\kappa_1 = \kappa_2 = \kappa$. Therefore, the anisotropic part of GOH model can be further simplified to

$$\bar{W}_{\text{aniso}}(\bar{\boldsymbol{C}}, \boldsymbol{H}_4, \boldsymbol{H}_6) = \frac{\mathrm{k}_1}{2\mathrm{k}_2} \sum_{i=4,6} [\exp\{\mathrm{k}_2 \langle \bar{E}_i \rangle^2\} - 1]. \tag{3.14}$$

3.2.3 Stress Tensor Evaluation

As the strain energy function above, the stress-stretch relation of GOH model will also be decomposed into three parts, which are volumetric, isotropic, and anisotropic parts. The second Piola-Kirchhoff stress tensor **S** is then given by

$$\boldsymbol{S} = 2\frac{\partial W}{\partial \boldsymbol{C}} = \boldsymbol{S}_{vol} + \overline{\boldsymbol{S}}_{iso} + \overline{\boldsymbol{S}}_{aniso,} \tag{3.15}$$

where the volumetric part $\boldsymbol{S}_{vol}$ is

$$\boldsymbol{S}_{vol} = 2\frac{\partial W_{vol}}{\partial \boldsymbol{C}} = \frac{\mathrm{K}}{2}J^{2/3}(J^2 - 1)\overline{\boldsymbol{C}}^{-1}, \tag{3.16}$$

and the isotropic part $\overline{\boldsymbol{S}}_{iso}$ is

$$\overline{\boldsymbol{S}}_{iso} = 2\frac{\partial \overline{W}_{\mathrm{iso}}}{\partial \boldsymbol{C}} = J^{-\frac{2}{3}}\mu\left(\boldsymbol{I} - \frac{1}{3}\bar{I}_1\overline{\boldsymbol{C}}^{-1}\right), \tag{3.17}$$

while the anisotropic part $\overline{\boldsymbol{S}}_{aniso}$ is

$$\begin{aligned}\overline{\boldsymbol{S}}_{aniso} &= 2\frac{\partial \overline{W}_{\mathrm{aniso}}}{\partial \boldsymbol{C}} \\ &= J^{-2/3}\sum_{i=4,6} 2k_1\langle\bar{E}_i\rangle\{exp[k_2(\bar{E}_i)^2]\}\left[\boldsymbol{H}_i - \frac{1}{3}(\bar{E}_i + 1)\overline{\boldsymbol{C}}^{-1}\right].\end{aligned} \tag{3.18}$$

To sum up, by combining Equations (3.16), (3.17) and (3.18), the total second Piola-Kirchhoff stress is given by

$$\begin{aligned}\boldsymbol{S} &= \boldsymbol{S}_{vol} + \overline{\boldsymbol{S}}_{iso} + \overline{\boldsymbol{S}}_{aniso} \\ &= \frac{\mathrm{K}}{2}J^{\frac{2}{3}}(J^2 - 1)\overline{\boldsymbol{C}}^{-1} + J^{-\frac{2}{3}}\mu\left(\boldsymbol{I} - \frac{1}{3}\bar{I}_1\overline{\boldsymbol{C}}^{-1}\right) \\ &+ J^{-2/3}\sum_{i=4,6} 2k_1\langle\bar{E}_i\rangle\{exp[k_2(\bar{E}_i)^2]\}\left[\boldsymbol{H}_i - \frac{1}{3}(\bar{E}_i + 1)\overline{\boldsymbol{C}}^{-1}\right].\end{aligned} \tag{3.19}$$

Therefore, using standard relations, the Cauchy stress can be obtained from $\boldsymbol{\sigma} = \frac{1}{J}\boldsymbol{F}\boldsymbol{S}\boldsymbol{F}^T$

$$\begin{aligned}\boldsymbol{\sigma} &= \frac{1}{J}\boldsymbol{F}\boldsymbol{S}\boldsymbol{F}^{T} \\ &= \frac{K}{2}(J - J^{-1})\boldsymbol{I} + J^{-1}\mu\left(\bar{\boldsymbol{b}} - \frac{1}{3}\bar{I}_1\boldsymbol{I}\right) \\ &+ J^{-1}\sum_{i=4,6} 2k_1\langle\bar{E}_i\rangle\{exp[k_2(\bar{E}_i)^2]\}\left[\bar{\boldsymbol{b}}\boldsymbol{H}_i - \frac{1}{3}(\bar{E}_i + 1)\boldsymbol{I}\right].\end{aligned} \tag{3.20}$$

3.2.4 Elasticity Tensor

The material elasticity tensor is derived from second Piola-Kirchhoff stress with

$$\mathbb{C} = 2\frac{\partial \boldsymbol{S}}{\partial \boldsymbol{C}} = \mathbb{C}_{vol} + \mathbb{C}_{iso} + \mathbb{C}_{aniso}, \tag{3.21}$$

where $\mathbb{C}_{vol}$ is the volumetric part, $\mathbb{C}_{iso}$ is the isotropic part, and $\mathbb{C}_{aniso}$ is the anisotropic part, Before further derive where the volumetric elasticity tensor is given as

$$\mathbb{C}^{vol} = 2\frac{\partial \boldsymbol{S}_{vol}}{\partial \boldsymbol{C}} = K\left[J^{2/3}\bar{\boldsymbol{C}}^{-1}\otimes\bar{\boldsymbol{C}}^{-1} - J^{-4/3}(J^2 - 1)\bar{\boldsymbol{C}}^{-1}\odot\bar{\boldsymbol{C}}^{-1}\right], \tag{3.22}$$

where $\bar{\boldsymbol{C}}^{-1}\odot\bar{\boldsymbol{C}}^{-1}$ is a fourth-order tensor defined as

$$[\bar{\boldsymbol{C}}^{-1}\odot\bar{\boldsymbol{C}}^{-1}]_{IJKL} \equiv -\frac{\partial \bar{C}_{IJ}^{-1}}{\partial \bar{C}_{KL}^{-1}} = \frac{1}{2}\left(\bar{C}_{IK}^{-1}\bar{C}_{JL}^{-1} + \bar{C}_{IL}^{-1}\bar{C}_{JK}^{-1}\right). \tag{3.23}$$

Then the anisotropic term $\mathbb{C}^{\text{iso}}$ is given as,

$$\begin{aligned}\mathbb{C}^{iso} &= 2\frac{\partial \boldsymbol{S}_{iso}}{\partial \boldsymbol{C}} \\ &= -\frac{2}{3}J^{-4/3}\mu(\overline{\boldsymbol{C}}^{-1}\otimes \boldsymbol{I} + \boldsymbol{I}\otimes \overline{\boldsymbol{C}}^{-1}) \\ &+\frac{2}{9}J^{-4/3}\mu\bar{I}_1\overline{\boldsymbol{C}}^{-1}\otimes\overline{\boldsymbol{C}}^{-1} \\ &+\frac{2}{3}J^{-4/3}\mu\bar{I}_1\overline{\boldsymbol{C}}^{-1}\odot\overline{\boldsymbol{C}}^{-1}.\end{aligned} \tag{3.24}$$

The anisotropic elasticity tensor is

$$\begin{aligned}\mathbb{C}^{aniso} &= 2\frac{\partial \boldsymbol{S}_{aniso}}{\partial \boldsymbol{C}} \\ &= \sum_{i=4,6} J^{-\frac{4}{3}}\Big\{\alpha_1\Big[\boldsymbol{H}_i\otimes\overline{\boldsymbol{C}}^{-1} + \overline{\boldsymbol{C}}^{-1}\otimes\boldsymbol{H}_i - \frac{1}{3}(\bar{E}_i+1)\overline{\boldsymbol{C}}^{-1}\otimes\overline{\boldsymbol{C}}^{-1} \\ &\qquad + \frac{1}{3}(\bar{E}_i+1)\overline{\boldsymbol{C}}^{-1}\odot\overline{\boldsymbol{C}}^{-1}\Big] \\ &+\alpha_2\Big[\boldsymbol{H}_i\otimes\boldsymbol{H}_i - \frac{1}{3}(\bar{E}_i+1)\boldsymbol{H}_i\otimes\overline{\boldsymbol{C}}^{-1} - \frac{1}{3}(\bar{E}_i+1)\overline{\boldsymbol{C}}^{-1}\otimes\boldsymbol{H}_i \\ &\qquad - \frac{1}{9}(\bar{E}_i+1)^2\overline{\boldsymbol{C}}^{-1}\otimes\overline{\boldsymbol{C}}^{-1}\Big]\Big\},\end{aligned} \tag{3.25}$$

where

$$\alpha_1 = -\frac{4}{3}k_1\langle\bar{E}_i\rangle\{exp[k_2(\bar{E}_i)^2]\}, \tag{3.26}$$

$$\alpha_2 = k_1\left[2\left(\frac{|\bar{E}_i|}{\bar{E}_i}+1\right)+8k_2\langle\bar{E}_i\rangle^2\right]\exp[k_2(\bar{E}_i)^2]. \tag{3.27}$$

Combining Equations (3.22), (3.24) and (3.25), the complete material elasticity tensor becomes

$$
\begin{aligned}
\mathbb{C} = \mathbb{C}_{vol} + \mathbb{C}_{iso} + \mathbb{C}_{aniso} \\
&= K\left[J^{\frac{2}{3}}\overline{\boldsymbol{C}}^{-1}\otimes\overline{\boldsymbol{C}}^{-1} - J^{-\frac{4}{3}}(J^2-1)\overline{\boldsymbol{C}}^{-1}\odot\overline{\boldsymbol{C}}^{-1}\right] \\
&-\frac{2}{3}J^{-\frac{4}{3}}\mu(\bar{C}^{-1}\otimes I + I\otimes\bar{C}^{-1}) + \frac{2}{9}J^{-4/3}\mu\bar{I}_1\bar{C}^{-1}\otimes\bar{C}^{-1} \\
&+\frac{2}{3}J^{-\frac{4}{3}}\mu\bar{I}_1\bar{C}^{-1}\odot\bar{C}^{-1} \\
&+\sum_{i=4,6}J^{-\frac{4}{3}}\Big\{\alpha_1\left[\boldsymbol{H}_i\otimes\overline{\boldsymbol{C}}^{-1} + \overline{\boldsymbol{C}}^{-1}\otimes\boldsymbol{H}_i - \frac{1}{3}(\bar{E}_i+1)\overline{\boldsymbol{C}}^{-1}\right. \\
&\left.\otimes\overline{\boldsymbol{C}}^{-1} + \frac{1}{3}(\bar{E}_i+1)\overline{\boldsymbol{C}}^{-1}\odot\overline{\boldsymbol{C}}^{-1}\right] \\
&+\alpha_2\left[\boldsymbol{H}_i\otimes\boldsymbol{H}_i - \frac{1}{3}(\bar{E}_i+1)\boldsymbol{H}_i\otimes\overline{\boldsymbol{C}}^{-1} - \frac{1}{3}(\bar{E}_i+1)\overline{\boldsymbol{C}}^{-1}\right. \\
&\left.\otimes\boldsymbol{H}_i - \frac{1}{9}(\bar{E}_i+1)^2\overline{\boldsymbol{C}}^{-1}\otimes\overline{\boldsymbol{C}}^{-1}\right]\Big\}.
\end{aligned}
\tag{3.28}
$$

Following Bonet [143], the spatial elasticity tensor $\mathbb{c}$ is defined as the push forward of material elasticity tensor $\mathbb{C}$ as

$$
\mathbb{c} = \sum_{i,j,k,l,I,J,K,L=1}^{3} J^{-1}F_{iI}F_{jJ}F_{kK}F_{lL}C_{IJKL}\,e_i\otimes e_j\otimes e_k\otimes e_l. \tag{3.29}
$$

3.2.5 Derivation for Tangent Stiffness

The uniaxial tangent stiffness, which is the slope of tensile stress with respect to tensile stretch, can be obtained from linearization relation with the spatial elasticity tensor $\mathbb{c}$ by the relation of

$$
\hat{\boldsymbol{\sigma}} = \mathbb{c}\colon\boldsymbol{d}, \tag{3.30}
$$

where

$$\hat{\boldsymbol{\sigma}} = \dot{\boldsymbol{\sigma}} - \boldsymbol{l}\boldsymbol{\sigma} - \boldsymbol{\sigma}\boldsymbol{l}^{\boldsymbol{T}} + \boldsymbol{\sigma} tr(\boldsymbol{l}), \tag{3.31}$$

is the objective Truesdell stress rate of Cauchy stress tensor, and $\boldsymbol{d} = \frac{1}{2}(\boldsymbol{l} + \boldsymbol{l}^T)$ is the rate of deformation tensor, and $\boldsymbol{l} = \dot{\boldsymbol{F}}\boldsymbol{F}^{-1}$ is the velocity gradient tensor. The Equation (3.31) can be rewritten into Voigt matrix form as

$$\begin{Bmatrix} \hat{\sigma}_{11} \\ \hat{\sigma}_{22} \\ \hat{\sigma}_{33} \\ \hat{\sigma}_{12} \\ \hat{\sigma}_{23} \\ \hat{\sigma}_{13} \end{Bmatrix} = \begin{bmatrix} c_{1111} & c_{1122} & c_{1133} & c_{1112} & c_{1123} & c_{1113} \\ c_{2211} & c_{2222} & c_{2233} & c_{2212} & c_{2223} & c_{2213} \\ c_{3311} & c_{3322} & c_{3333} & c_{3312} & c_{3323} & c_{3313} \\ c_{1211} & c_{1222} & c_{1233} & c_{1212} & c_{1223} & c_{1213} \\ c_{2311} & c_{2322} & c_{2333} & c_{2312} & c_{2323} & c_{2313} \\ c_{1311} & c_{1322} & c_{1333} & c_{1312} & c_{1323} & c_{1313} \end{bmatrix} \begin{Bmatrix} d_{11} \\ d_{22} \\ d_{33} \\ d_{12} \\ d_{23} \\ d_{13} \end{Bmatrix}. \tag{3.32}$$

Under the uniaxial loading condition (deformation gradient was showed in Equation), the deformation gradient **F** can be represented as

$$\boldsymbol{F} = \begin{bmatrix} \lambda_1 & 0 & 0 \\ 0 & \lambda_2 & 0 \\ 0 & 0 & \lambda_3 \end{bmatrix}. \tag{3.33}$$

Therefore, the Equation (3.32) can be reduced to Equation (3.34) because the shear stress/strain is zero with the symmetric structure of sample, and $\boldsymbol{l} = \boldsymbol{l}^T = \text{diag}\left(\dot{\lambda}_{11}\lambda_{11}^{-1}, \dot{\lambda}_{22}\lambda_{22}^{-1}, \dot{\lambda}_{33}\lambda_{33}^{-1}\right)$

$$\begin{Bmatrix} \hat{\sigma}_{11} \\ \hat{\sigma}_{22} \\ \hat{\sigma}_{22} \end{Bmatrix} = \begin{bmatrix} c_{1111} & c_{1122} & c_{1133} \\ c_{2211} & c_{2222} & c_{2233} \\ c_{3311} & c_{3322} & c_{3333} \end{bmatrix} \begin{Bmatrix} \dot{\lambda}_{11}\lambda_{11}^{-1} \\ \dot{\lambda}_{22}\lambda_{22}^{-1} \\ \dot{\lambda}_{33}\lambda_{33}^{-1} \end{Bmatrix}. \tag{3.34}$$

If it is assumed that 1-direction in Figure 3.4 is the loading direction ($\hat{\sigma}_{11} \neq 0$, $\hat{\sigma}_{22} = 0$, and $\hat{\sigma}_{33} = 0$), we can get the relation from the second and third equations in Equation (3.34) that

$$\dot{\lambda}_{22}\lambda_{22}^{-1} = -\frac{c_{2211}\dot{\lambda}_{11}\lambda_{11}^{-1} + c_{2233}\dot{\lambda}_{33}\lambda_{33}^{-1}}{c_{2222}}, \tag{3.35}$$

$$\dot{\lambda}_{22}\lambda_{22}^{-1} = -\frac{c_{3311}\dot{\lambda}_{11}\lambda_{11}^{-1} + c_{3333}\dot{\lambda}_{33}\lambda_{33}^{-1}}{c_{3322}}. \tag{3.36}$$

Then, from the relation of Equation (3.35) equals to Equation (3.36), the relation between $\dot{\lambda}_{11}\lambda_{11}^{-1}$ and $\dot{\lambda}_{33}\lambda_{33}^{-1}$ can be obtained as

$$\dot{\lambda}_{33}\lambda_{33}^{-1} = \frac{c_{2222}c_{3311} - c_{2211}c_{3322}}{c_{2233}c_{3322} - c_{2222}c_{3333}}\dot{\lambda}_{11}\lambda_{11}^{-1}. \tag{3.37}$$

Then bring Equation (3.37) into Equation (3.36), the relation between $\dot{\lambda}_{22}\lambda_{22}^{-1}$ and $\dot{\lambda}_{11}\lambda_{11}^{-1}$ can be obtained as

$$\dot{\lambda}_{22}\lambda_{22}^{-1} = -\frac{c_{2211}}{c_{2222}} + \frac{c_{2233}}{c_{2222}}\frac{c_{2222}c_{3311} - c_{2211}c_{3322}}{c_{2233}c_{3322} - c_{2222}c_{3333}}\dot{\lambda}_{11}\lambda_{11}^{-1}. \tag{3.38}$$

Finally, bring Equation (3.37) and Equation (3.38) back into the first equation in matrix expression of Equation (3.34). After rearranging the equation, the relation becomes the form of $\dot{\sigma}_{11} = E\dot{\lambda}_{11}$. If we multiply both side with dt, the equation can be rewritten into incremental form as

$$d\sigma_{11} = Ed\lambda_{11}, \tag{3.39}$$

and the slope E is given as

$$\begin{aligned} E = \Bigg[& c_{1111} - c_{1122}\left(\frac{c_{2211}}{c_{2222}} + \frac{c_{2233}}{c_{2222}}\frac{c_{2222}c_{3311} - c_{2211}c_{3322}}{c_{2233}c_{3322} - c_{2222}c_{3333}}\right) \\ & + c_{1133}\frac{c_{2222}c_{3311} - c_{2211}c_{3322}}{c_{2233}c_{3322} - c_{2222}c_{3333}} \\ & + \sigma_{11}\left(1 + \frac{c_{2211}}{c_{2222}} + \frac{c_{2233}}{c_{2222}}\frac{c_{2222}c_{3311} - c_{2211}c_{3322}}{c_{2233}c_{3322} - c_{2222}c_{3333}}\right. \\ & \left. - \frac{c_{2222}c_{3311} - c_{2211}c_{3322}}{c_{2233}c_{3322} - c_{2222}c_{3333}}\right)\Bigg]\lambda_{11}^{-1}. \end{aligned} \tag{3.40}$$

3.3 ABAQUS Simulation Settings

As mentioned in the Section 3.1 , the commercial finite element software package ABAQUS was used to simulate uniaxial tensile tests and generate three sets of data which are tensile stress, tensile stretch and transverse stretch. The referential sample geometry and material parameters are taken from Gasser's paper [109]. The dimensions of the sample $L = 10.0mm, W = 3.0mm, T = 0.5mm$ are provided. Material parameters are given in Table 3.1 and the bulk modulus was assumed to be 2 *GPa* to approximate nearly incompressible behavior.

In the simulations, the displacement in the l-direction of Face EFGH is fixed to zero (2 and 3 directions are free), displacement boundary condition $\boldsymbol{u}$ is placed on the other end of the 1-direction (2 and 3 directions are free), and two sides of the sample are left unconstrained (see Figure 3.4). The deformation gradient $\boldsymbol{F}$ for the uniaxial tensile test can be represented as

$$\boldsymbol{F} = \begin{bmatrix} \lambda_1 & 0 & 0 \\ 0 & \lambda_2 & 0 \\ 0 & 0 & \lambda_3 \end{bmatrix}. \tag{3.41}$$

The *'parallel specimen'* and *'perpendicular specimen'* cut from the material sheet are orthogonal to each other (See Figure 3.1). The angle between mean fiber orientation and reference direction is given as $\gamma = 49.98$. Since the direction of tension on specimen is parallel to the longitudinal direction of specimen (See Figure 3.4), the mean fiber orientation γ for the parallel specimen is $49.98°$, and the mean fiber orientation for perpendicular specimen is $90 - \gamma$, which is 40.2 in the simulation . The specific displacement values are also taken from Gasser's paper [109], which are 2.6

mm for parallel specimen and 1.9 mm for perpendicular specimen. The generated stress-stretch data has been shown in Figure 3.2.

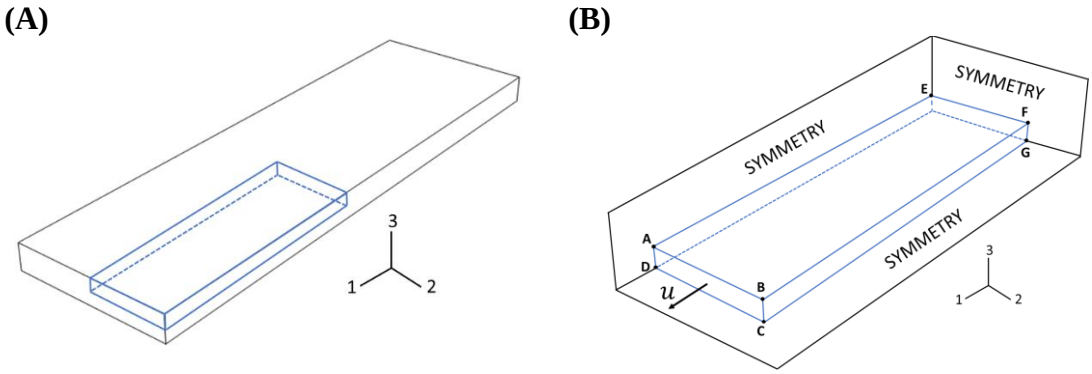

Figure 3.4 Schematic plot for uniaxial tensile test simulation. **(A)** 1/8 of the specimen geometry was taken for the ABAQUS simulation, **(B)** The boundary conditions of the simulation. The symmetry boundary conditions are placed on the ADHE, EFGH, and CDHG planes, and the displacement boundary condition $\boldsymbol{u}$ are placed on the ABCD plane.

3.4 Microstructural Arrangement Determination Approach

The GOH model has five unknown parameters ($\boldsymbol{\beta} = \{\mu, \kappa, k_1, k_2, \gamma\}$) which will be identified by calibrating the model against simulation data using a built-in Matlab (MATLAB R2019b, MathWorks) function *fmincon*. This process involves minimizing the objective functions (Eq. 26) and satisfying the stiffness constraint functions (Eq. 27), as described in detail below. This solver is commonly used to calibrate the constrained nonlinear multivariable model for soft tissue materials, e.g., artery [144]. Furthermore, following Balaban [145] the *MultiStart* optimization algorithm in MATLAB Optimization Toolbox was employed with $n_{guess} = 50$ initial conditions in the best effort to ensure the global minimum was found for the objective function. Based on the boundary conditions of uniaxial tensile test shown in Figure 3.4, the objective functions minimized in the model calibration are shown in Equation (3.42).

$$\mathrm{F}(\boldsymbol{\beta}) = \sum_{i=1}^{n_1} \left[\left({\sigma_{11}}_i^{par} - {\sigma_{11}^{sim}}_i^{par} \right)^2 + \left({\sigma_{22}}_i^{par} - 0 \right)^2 \right] + \sum_{i=1}^{n_2} \left[\left({\sigma_{11}}_i^{per} - {\sigma_{11}^{sim}}_i^{per} \right)^2 + \left({\sigma_{22}}_i^{per} - 0 \right)^2 \right], \tag{3.42}$$

where n_1 and n_2 are the number of data points in the parallel and perpendicular samples respectively. ${\sigma_{11}}_i$ and ${\sigma_{22}}_i$ are the ith data point of tensile and transverse Cauchy stresses respectively. The superscript par and per in ${\sigma_{11}}_i^{par}$ and ${\sigma_{11}}_i^{per}$ indicates the tensile stress of parallel and perpendicular samples respectively. And σ_{11}^{sim} is the simulation data of tensile stress generated from ABAQUS simulation.

For the constraint functions, the tangent stiffness (evaluated from $\boldsymbol{\beta} = \{\mu, \kappa, k_1, k_2, \gamma\}$) at the middle point of toe and linear regions are constrained to be equivalent to the slope at the respective regions. . The four constraint functions are given as,

$$\begin{aligned} \frac{E_{TR}^{Par}}{M_{TR}^{Par}} - 1 = 0, \\ \frac{E_{LR}^{Par}}{M_{LR}^{Par}} - 1 = 0, \\ \frac{E_{TR}^{Per}}{M_{TR}^{Per}} - 1 = 0, \\ \frac{E_{LR}^{Per}}{M_{LR}^{Per}} - 1 = 0, \end{aligned} \tag{3.43}$$

where M are slopes evaluated from simulation data by finding the slope of respective regions with MATLAB built-in function - polyfit. TR indicates Toe Region, and LR

indicates Linear Region (See Figure 3.3). An algorithm of linear regression was developed to separate the Toe Region and Linear Region of stress-strain curve. Since the stress-strain relation in the toe and linear regions are roughly linear, starting from the first point and the last point for toe and linear regions respectively, and one point is added into the respective region until the R-squared value of linear regression is lower than 0.99. See Figure 3.5 for the algorithm details.

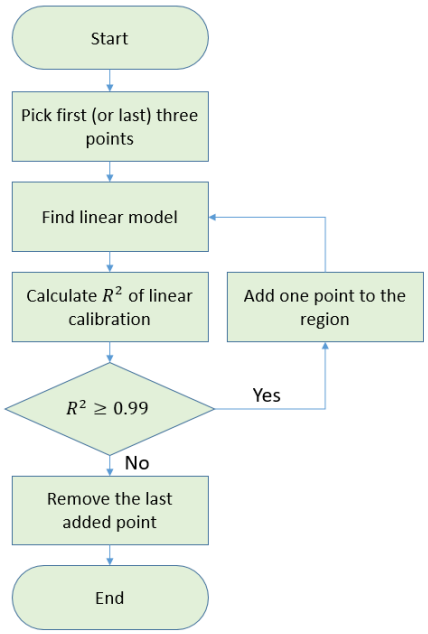

Figure 3.5 Flowchart of algorithm for separating toe and linear regions

The symbol E, which indicates the slope of tensile stress with respect to tensile stretch can be obtained from the tangent stiffness derivation in Section 3.2.5 . It is known that the nonlinear optimization procedures are often sensitive to the chosen initial parameter values, upper, and lower bounds. The lower bounds of all the parameters are zeros, and the upper bounds of mechanical parameters (μ, k_1, k_2) are determined based on the literature. Since the model parameters from Gasser's paper [109] are based on the arterial adventitia tissue, the stiffness of adventitia tissue was investigated and ranged

between 1500 kPa to 4237 kPa from literature [146 385, 147, 148], and the upper bounds of both μ and k_1 are set to be 5000 kPa. The structural parameters (γ, κ) are determined based on the structural limits of collagen fibers as reported by Gasser [109], since the mean fiber orientation γ can only vary in the range between $(0,90)$, and the fiber dispersion can only be in the range between $(0,1/3)$. The initial values of the model parameters are set between upper and lower bounds, and because of the physical interpretation of parameters μ and k_1 introduced above, the initial value of μ and k_1 are set to be the measured stiffness in the initial and linear region respectively. See Table 3.2 for the initial values, lower and upper bounds of model parameters for the constrained least-squares calibration. The initial values of the model parameters are also normalized for the best optimization results.

Table 3.2 Initial Values, Lower and Upper Bounds for Five Unknown Model Parameters

	Mechanical Properties			Structural Properties	
	$\mu\ (kPa)$	$k_1\ (kPa)$	k_2	$\gamma\ (\circ)$	κ
Initial Values	Stiffness in IR	Stiffness in LR	500	45	0.167
Lower Boundary	0	0	0	0	0
Upper Boundary	5000	5000	1000	90	0.3333

To sum up, the following algorithm procedure (Figure 3.6) was adopted for the model calibration

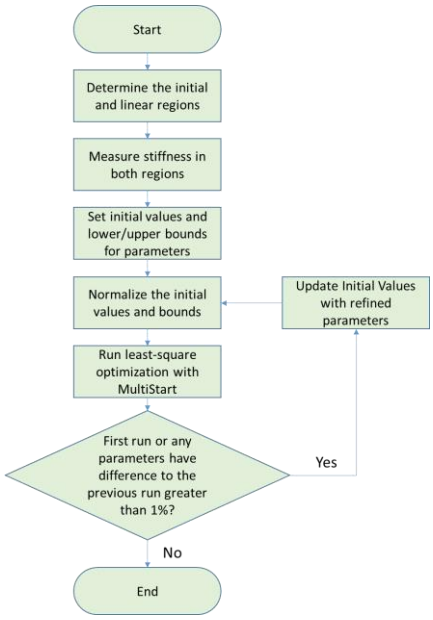

Figure 3.6 Flowchart of algorithm for GOH model calibration

The goodness of the model calibration was quantified with standard deviation error, (which is also used by Li [142]),

$$\varepsilon = \frac{1}{\sigma^{mean}} \sqrt{\frac{\mathrm{F}(\boldsymbol{\beta})}{2(n_1 + n_2)}}, \tag{3.44}$$

with $\mathrm{F}(\boldsymbol{\beta})$ as objective function shown in Equation (3.42), and normalized by the mean stress

$$\sigma^{mean} = \frac{\left(\sum_{i=1}^{n_1} \sigma_{11}{}_{i}^{exppar} + \sum_{i=1}^{n_2} \sigma_{11}{}_{i}^{expper}\right)}{2(n_1 + n_2)}. \tag{3.45}$$

3.5 Verification

3.5.1 Verification on ABAQUS simulation data

The stress and strain data sets of parallel and perpendicular specimens generated from ABAQUS simulation was imported into the program, and it is assumed that the material sheet presented in Figure 3.1 is identical throughout the sheet which means the mechanical properties (μ, k_1, k_2) and structural properties (γ, κ) of parallel and perpendicular specimens are the same with respect to the reference direction. After the model calibration, the model parameters are estimated with the standard deviation error of 3.73E-5. The estimated parameters are presented in Table 3.3. The stress-stretch curve generated by the estimated parameters is aligned to the simulation data in Figure 3.7.

Table 3.3 Results of Least-squared Optimization on Simulation Data

	Mechanical Parameters			Structural Parameters	
	$\mu\ (kPa)$	$k_1\ (kPa)$	k_2	$\gamma\ (\circ)$	κ
Known Parameters	7.64	996.60	524.60	49.98	0.226
Estimated Parameters	7.64	996.23	524.79	49.98	0.226
Difference %	0.01%	0.03%	0.04%	0.00%	0.02%

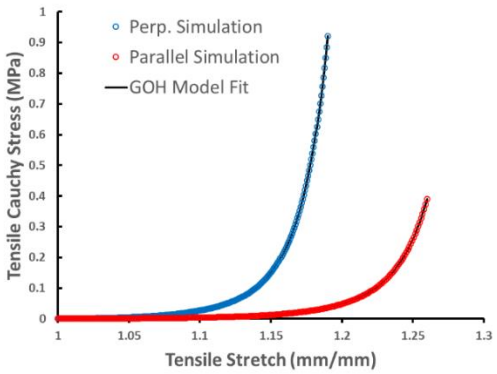

Figure 3.7 Comparison of the stress-stretch curves generated from the simulation data and from the estimated model parameters.

From the results obtained above, our approach of combining two orthogonal specimens to characterize the mechanical properties of soft tissue works well. The estimated model parameters are precise and the generated stress-stretch curves are aligned to the simulation data.

3.5.2 Verification on ABAQUS simulation data with variation

However, the stress strain data generated from ABAQUS simulation is too clean to be obtained in real experiments because of the expected fluctuation during data collection. In order to find out the feasibility of this model calibration method working with some real experiment data, some random variations is introduced to the simulation data to verify the sensitivity of the MADM method. In the first trial, the material displacements are assumed to be measured perfectly, and variation was introduced to the stress data by adopting the *randn* (generating random number array with normal distribution) function in MatLab. The variation percentage keeps increasing from 1% until there is one or more parameters have more than 5% difference. On the other hand, the same approach is applied except the stress is fixed perfectly and the variation is placed on the strain data. The results can be seen in Table 3.4, and the stress-stretch curves are compared in Figure 3.8.

Table 3.4 Results of Least-squared Optimization on Simulation Data with Variation in Stress

	$\mu\ (kPa)$	$k_1\ (kPa)$	k_2	$\gamma\ (\circ)$	κ	*R-Squared*	*SDE*
Known Parameters	7.64	996.60	524.60	49.98	0.226	/	/
Variation on Stress Data							
$\pm$1% Variation	7.75	977.53	526.95	50.00	0.226	0.99	4.95E-4
Difference %	1.41%	1.91%	0.45%	0.04%	0.22%	/	/
$\pm$2% Variation	7.83	999.63	515.07	49.71	0.220	0.99	5.35E-4
Difference %	2.47%	0.30%	1.82%	0.54%	2.85%	/	/
$\pm$3% Variation	7.83	1009.16	525.26	49.85	0.225	0.98	7.35E-4
Difference %	2.44%	1.26%	0.13%	0.27%	0.47%	/	/
$\pm$4% Variation	7.89	968.52	547.96	49.89	0.228	0.97	9.52E-4
Difference %	3.25%	2.82%	4.45%	0.18%	0.96%	/	/
$\pm$5% Variation	7.66	906.85	553.31	50	0.226	0.97	7.83E-4
Difference %	0.21%	9.01%	5.47%	0.05%	0.01%	/	/
Variation on Strain Data							
$\pm$1% Variation	7.62	1011.07	511.57	49.94	0.223	0.982	7.71E-4
Difference %	0.21%	1.45%	2.48%	0.07%	1.20%	/	/
$\pm$2% Variation	7.54	1072.47	506.87	49.95	0.227	0.961	9.54E-4
Difference %	1.37%	7.61%	3.38%	0.06%	0.39%	/	/

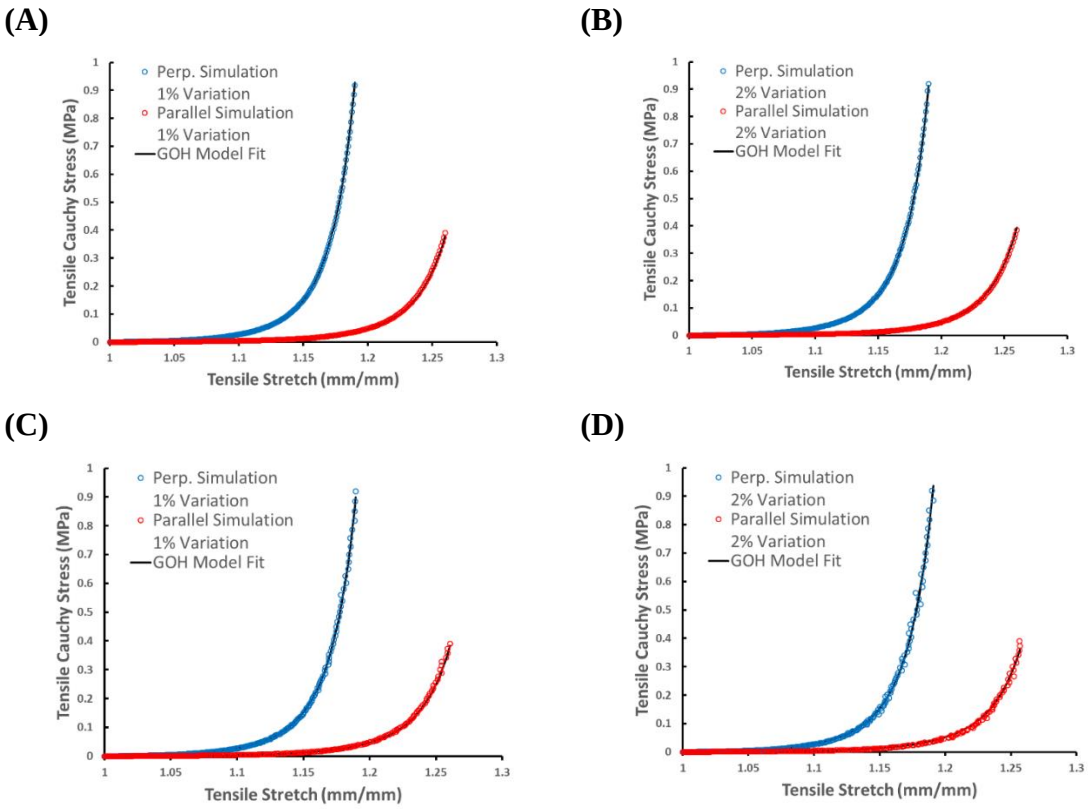

Figure 3.8 Comparison of the stress-stretch curves generated from the simulation data with variation on stress and from the estimated model parameters. **(A)** 1% variation on stress, **(B)** 2% variation on stress, **(C)** 1% variation on stretch, **(D)** 2% variation on stretch.

From Table 3.4 and Figure 3.8, we can see that the mechanical properties $(\mu, k_1, k_2)$are more sensitive than the structural properties (γ, κ) under data fluctuation.

3.5.3 MADM Model Validation on Off-axis Specimens

In Figure 3.1, a 45-degree sample that is 45 degree deviated from the *Reference Direction* is known as an off-axis specimen which is also simulated in ABAQUS. Because the sample structure is no longer symmetric about the loading direction, the boundary conditions of 45-degree sample in the ABAQUS simulation are different and shown in Figure 3.9. The deformation gradient $\boldsymbol{F}$ becomes,

$$\boldsymbol{F} = \begin{bmatrix} F_{11} & F_{12} & 0 \\ F_{21} & F_{22} & 0 \\ 0 & 0 & F_{33} \end{bmatrix} = \begin{bmatrix} \lambda_{11} & \gamma_{12} & 0 \\ \gamma_{21} & \lambda_{22} & 0 \\ 0 & 0 & \lambda_{33} \end{bmatrix}. \quad (3.46)$$

Shear deformation in the 2-3 and 1-3 planes are zero because the collagen fiber is assumed to be only in the plane of 1-2. The components of deformation gradient in Equation (3.46) are generated from ABAQUS simulation for validation on 45-degree sample. The stress-stretch curve of 45-degree specimen generated from the optimal model parameters in Table 3.3 is compared to the stress-stretch curve from ABAQUS simulation in Figure 3.10. The goodness of model calibration is measured by the R-squared value and standard deviation error as mentioned in Equation (3.45). The same approach was also applied to the 30-degree specimen and 60-degree specimen for further validation, and the results are shown in Table 4.5 and Figure 3.11.

(A) **(B)**

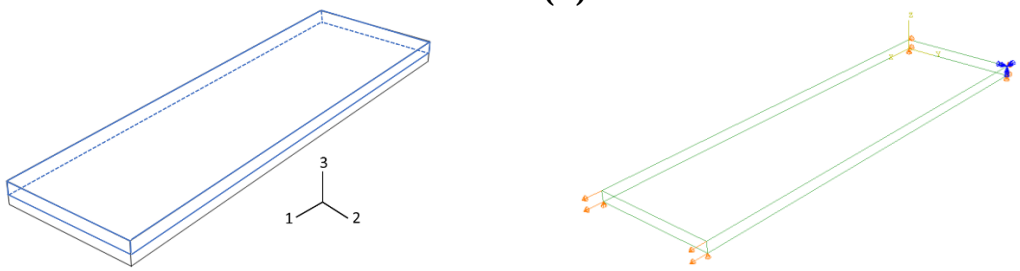

Figure 3.9 Schematic plot for uniaxial tensile test simulation. **(A)** 1/2 of the specimen geometry was taken for the ABAQUS simulation, **(B)** The boundary conditions of the simulation.

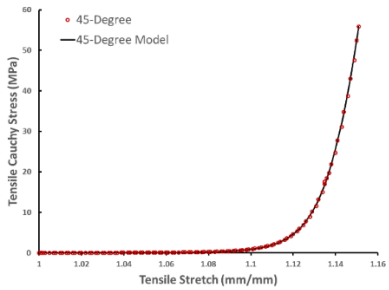

Figure 3.10 Comparison of the stress-stretch curves of 45-degree specimen generated from the simulation data and from the estimated model parameters.

(A) **(B)**

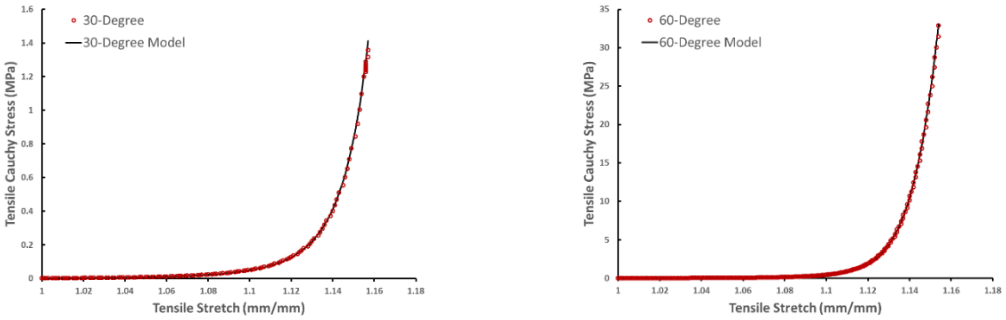

Figure 3.11 Comparison of the stress-stretch curves generated from the simulation data and from the estimated model parameters, **(A)** 30-degree specimen, **(B)** 60-degree specimen.

Table 3.5 R-Square Value and Standard Deviation Error (SDE) for 30-Degree, 45-Degree, and 60-Degree Validation

	R-Square	**SDE**
30-Degree	0.97	5.86E-4
45-Degree	0.99	5.74E-5
60-Degree	0.98	1.07E-4

CHAPTER 4

MADM APPROACH ON EXPERIMENTAL DATA

In Chapter 3, the developed Microstructural Arrangement Determination Method (MADM) approach has been verified with ABAQUS simulation data. It has been shown that the MADM approach can estimate the material properties without any pre-known structural information, e.g., collagen fiber orientation and dispersion. In this Chapter, the MADM approach is implemented to the real experimental data of porcine skin dermis and try to characterize the material properties.

4.1 Initial Trial with Experimental Data of Skin Dermis

As introduced in Chapter 2, the 'Spine', 'Head' and 'Tail' are the unique references for sample location and orientation. The sample set with number 128 sample as *"Parallel Sample"* (parallel to the Spine) and number 127 sample as *"Perpendicular Sample*" (perpendicular to the Spine) is selected from all the experimental data of porcine skin dermis for the initial trails of MADM approach. The locations of samples are shown in the Figure 4.1. The stress-strain curve and the relation between transverse strain and tensile strain are shown in Figure 4.2.

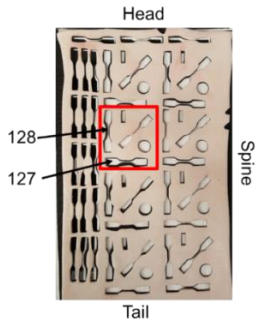

Figure 4.1 Location of sample 127 and 128 in the skin sheet.

(A) **(B)**

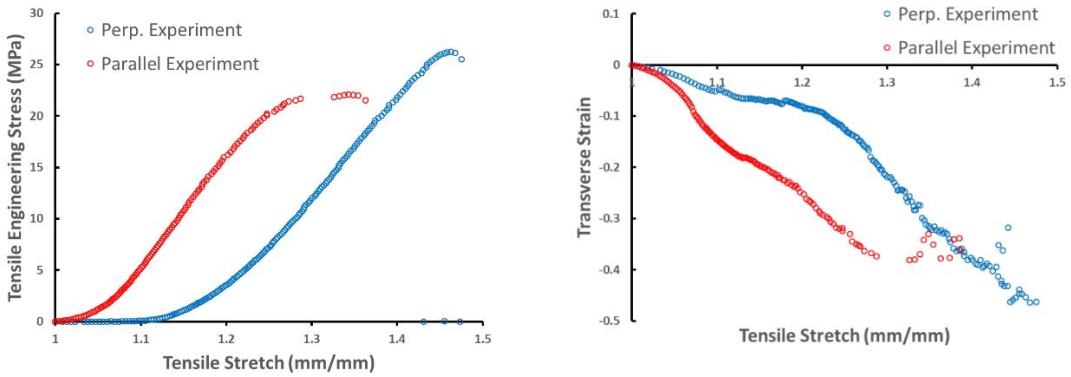

Figure 4.2 Experimental data of sample set example **(A)** Stress-stretch curves of parallel and perpendicular data set (127-128) from experimental data of porcine skin dermis, **(B)** Transverse engineering Strain against tensile engineering strain for data set (127-128).

Based on the previous work, the linear zone ends at 80% of failure stress, therefore the curves shown in Figure 4.2 are truncated from 80% of failure stress which are shown in

(A) **(B)**

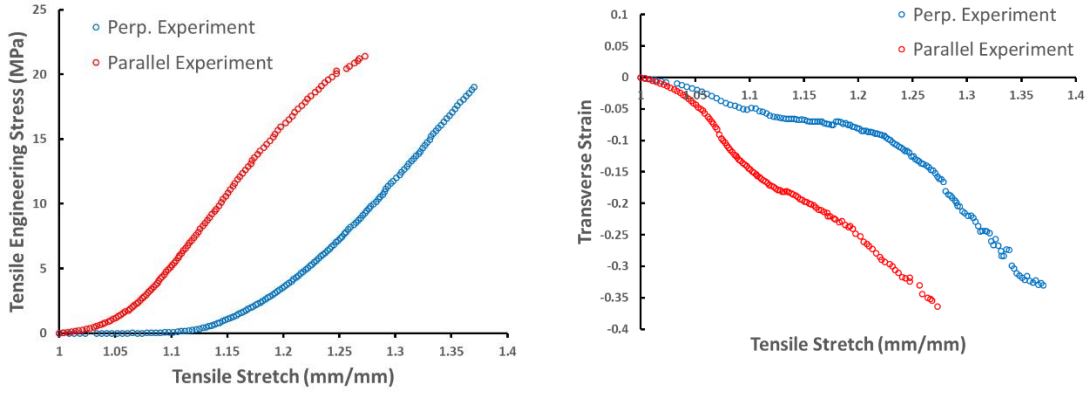

Figure 4.3 The relations of stress-stretch after truncating the failure phase. **(A)** Stress-stretch curves of parallel and perpendicular data set (127-128) from experimental data of porcine skin dermis. **(B)** Transverse engineering Strain against tensile engineering strain for data set (127-128)

After the 50 runs with the MultiStart algorithm, the MADM approach didn't converge to a feasible result, and the run with the best fitting goodness is with R-square value equal to 0.62. The estimated model parameters are shown in **Table 4.1**, and the stress-stretch curve generated from estimated model parameters is shown in **Figure 4.4**.

Table 4.1 Estimated Model Parameters of Sample Set 127-128

Mechanical Properties			Structural Properties	
$\mu\ (MPa)$	$k_1\ (MPa)$	k_2	$\gamma\ (\circ)$	κ
1.73	179.67	0.01	38.73	0.211

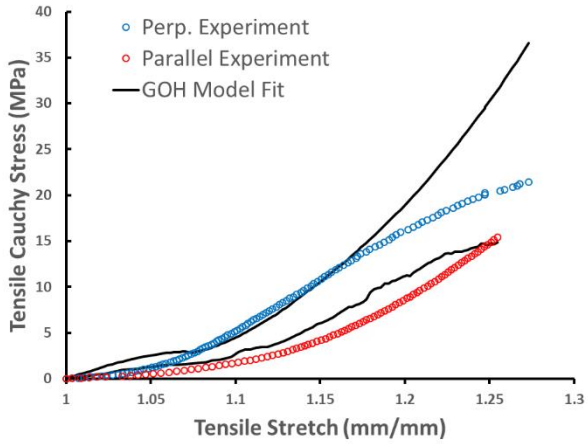

Figure 4.4 Stress-stretch curves with experimental data and fitting curve compared.

4.2 Issues Identifications of Non-convergence

In the Section 4.1 , it is shown that the MADM approach didn't converge to a feasible result, and the evaluated stress from MADM approach is not aligned to the stress from experiment. In this section, two possible reasons are explored. The first possible reason is that the GOH model and MADM approach cannot work with experimental data of porcine skin dermis. The second possible reason is that the treatment of transverse strain is not correct.

4.2.1 Confirm If It Is a Model Issue to Describe Dermis

GOH model was initially developed for describing the deformation behavior of arterial adventitia tissue in Gasser's paper [109]. The implementation of GOH model on porcine skin dermis tissue might be inappropriate. In this section, the experimental data of porcine skin dermis is compared to the experimental data of arterial adventitia tissue from literature [149] in terms of "*Degree of Anisotropy*" (DOA). The MADM approach is also applied to each set of data. The relation of goodness of fitting and DOA is presented.

The "*Degree of Anisotropy*" (DOA) is quantified by the stiffness ratio of samples in parallel and perpendicular orientation (circumferential and axial for adventitia tissue respectively). The relation of DOA can be presented as

$$DOA = \frac{E^{Par}}{E^{Per}}. \tag{4.1}$$

The DOA in both toe and linear regions are defined with the experimental data of arterial adventitia tissue from Holzapfel's paper [149]. In addition, the "*Ratio of L/T Ratio*" (Linear Slope Ratio / Toe Slope Ratio) and "*Ratio of Init. Strain %*" (Percentage of Toe strain in the entire curve) are also compared for further information. DOA of all the nine sample sets in Figure 4.5 are calculated and compared to our experimental data of skin dermis.

The transverse strain was not measured by Holzapfel [149], therefore the 'One-Strain' version of MADM approach was implemented to estimate the material properties. The 'One-Strain' method is commonly utilized in the literature because of the absence of the measurement of transverse deformation in the specimen [34]. The transverse strain is calculated (instead of measured in experiments) from the relation of transverse stress equal to zero ($P_{tran} = 0$) as the boundary conditions of uniaxial tensile test discussed in Chapter

3. Because of the absence of the measured transverse strain from literature, the "One-Strain" version of MADM approach is applied to each data set in Figure 4.5. The results of comparison are shown in Table 4.2. The R-square value of each curve fitting ranges from 0.83 to 0.96, and there is no obvious relation between DOA and the goodness of fitting found.

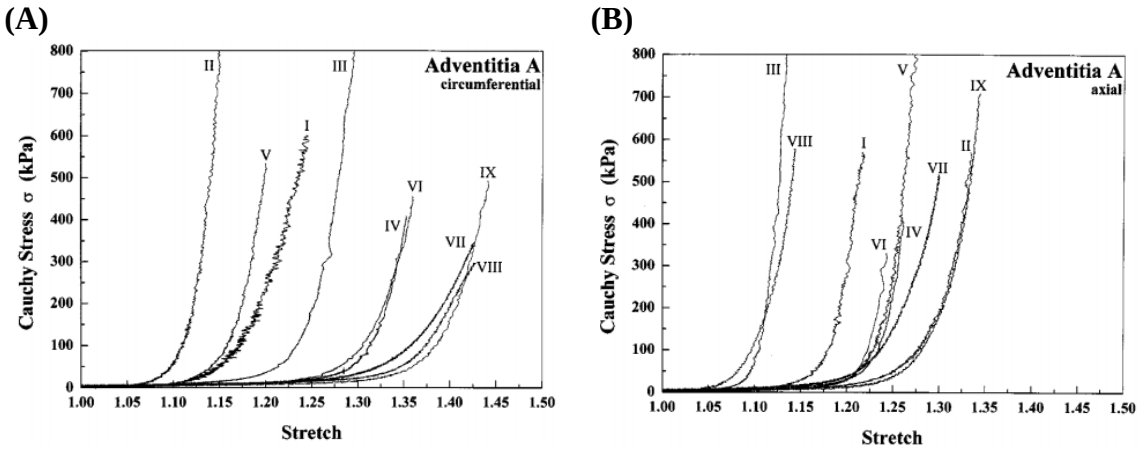

Figure 4.5 Stress-stretch curve of arterial adventitia tissue **(A)** circumferential samples, **(B)** axial samples.
Source: [149].

Table 4.2 Acquisition Interval for Different Stretch Speed

Sample Set	Toe Slope Ratio	Linear Slope Ratio	Ratio of L/T Ratio	Ratio of Init. Strain %	R-Squared Value
1	1.07	0.73	0.68	0.91	0.84
2	0.46	1.09	2.35	1.25	0.86
3	0.69	0.75	1.10	1.00	0.85
4	0.30	0.30	1.01	1.01	0.91
5	0.19	0.10	0.55	1.00	0.83
6	2.71	0.86	0.32	0.80	0.91
7	0.49	0.31	0.64	0.93	0.95
8	1.69	2.09	1.24	1.03	0.95
9	0.33	0.31	0.93	0.98	0.96
Mean Skin Back	1.73	1.88	1.08	0.77	/
Mean Skin Neck	1.25	1.26	1.01	0.86	/

From the results shown in Table 4.2, we know that the stress-stretch curves of back and neck regions has no obvious difference to the arterial adventitia tissues in terms of DOA, however, by utilizing the 'One-strain' method, the goodness of fitting is better.

4.2.2 Confirm If This Is in Treatment of Transverse Strain

The second possible reason is that the transverse deformation of porcine skin dermis doesn't work with GOH model. In order to verify for this reason, the GOH model and MADM approach are applied to the experimental data of arterial adventitia tissue in Sokolis's research [150] which has the transverse strain measured (see Figure 4.6). If the MADM model can be successfully applied to experimental data of arterial adventitia, we can say the failure of fitting on porcine skin dermis is because the GOH model has issues to describe the transverse deformation of porcine skin dermis material.

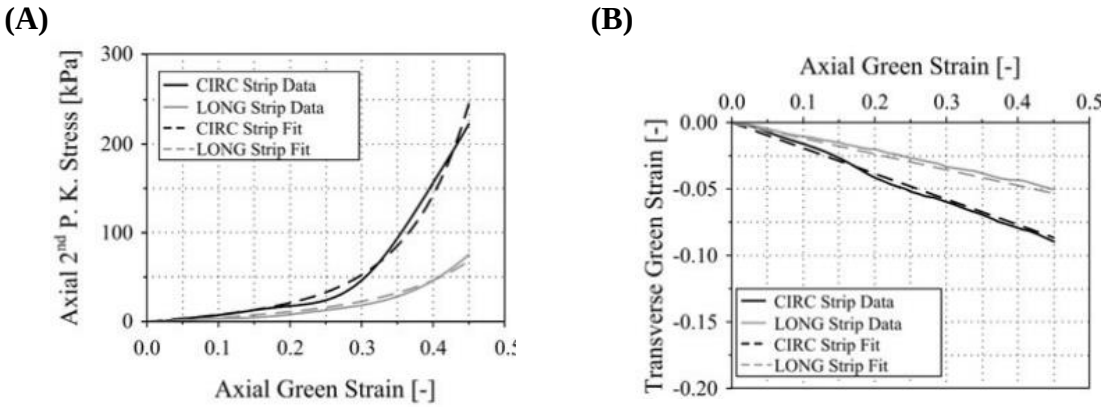

Figure 4.6 The stress-stretch curve of arterial adventitia tissue **(A)** 2nd PK stress against axial Green strain, **(B)** Transverse Green strain against axial Green strain.
Source: [150]

Both "One-Strain" version of MADM approach and "Two-Strain" version of MADM approach are applied to the experimental data in Sokolis's research [150] for comparison. The estimated model parameters with "One-Strain" version of MADM

approach are presented in Table 4.3, and the stress-stretch curve is given in Figure 4.7 (A). As you can see in Figure 4.7 (A), the calculated transverse strain are deviated from the measured transverse strain provided in the literature (see Figure 4.7 (B)). The comparison of measured and calculated Poisson's ratio is provided in Table 4.4.

Table 4.3 Estimated Model Parameters with "One-Strain" MADM Approach for Experimental Data in Sokolis's research [150]

Mechanical Properties			Structural Properties		
$\mu\ (kPa)$	$k_1\ (kPa)$	k_2	$\gamma\ (\circ)$	κ	R-Square
12.4	431	9.92	42.81	0.0001	0.84

Table 4.4 Comparison of between calculated transverse strain and measured transverse strain for Experimental Data in Sokolis's research [150]

	Measured Poisson's Ratio	Calculated Poisson's Ratio
Parallel Sample	0.11	1.22
Perpendicular Sample	0.2	1.33

(A)

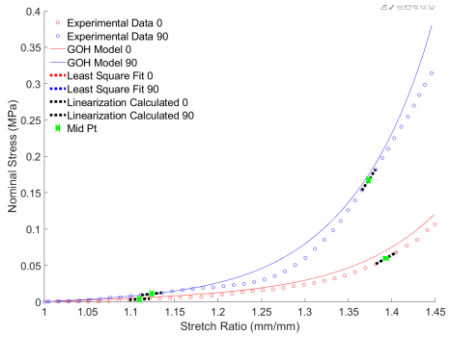

(B)

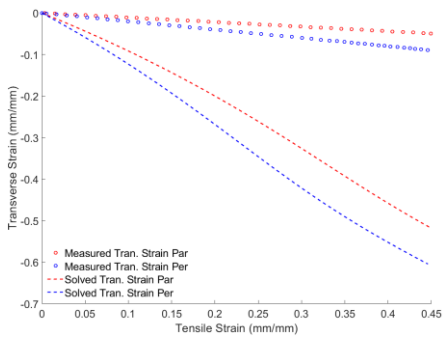

Figure 4.7 Stress-stretch curve with estimated model parameters with "One-Strain MADM" approach to the experimental data, **(A)** Stress-stretch curve, **(B)** Transverse strain against tensile strain.
Source: [150]

Using “Two-Strain” version of MADM approach, the model converge to a result with R-square value equal to 0.77. The estimated model parameters is presented in Table 4.5 and the stress-stretch curve is shown in Figure 4.8 (A). The obtained transverse stress with estimated model parameters is not exact zero, and the curve of transverse stress against tensile stretch can be found in Figure 4.8 (B).

Table 4.5 Estimated Model Parameters with “Two-Strain” MADM Approach for Experimental Data in Sokolis’s research [150]

Mechanical Properties			Structural Properties		
$\mu\ (kPa)$	$k_1\ (kPa)$	k_2	$\gamma\ (\circ)$	κ	R-Square
17.83	232.72	25.82	1	0.314	0.77

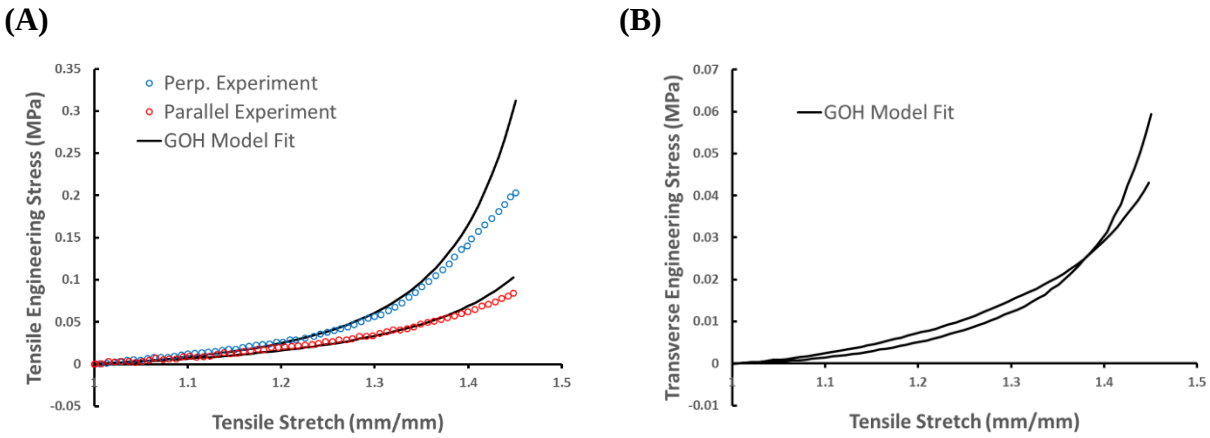

Figure 4.8 Stress-stretch curve with estimated model parameters with “Two-Strain MADM” approach to the experimental data
(A) Stress-stretch curve,
(B) Transverse stress against tensile strain.
Source: [150].

From this section, we can conclude that the degree of anisotropy (DOA) has no obvious effect to the goodness of GOH curve-fitting with MADM approach. And the GOH model cannot correctly predict the transverse strains by calculating from the relations of

transverse and thickness stresses are equal to zero. This conclusion has also been reported in multiple publications, such as mentioned by Latorre [151].

4.3 Sensitivity Analysis of Transverse Strain

In order to further understand how the transverse strain affects the GOH model fitting, this section will focus on identifying which term of transverse strain affects the stress most significant. The transverse strain plays a role in all the three components in terms of

- $J = \lambda_1\lambda_2\lambda_3$ as volume change
- $I_1 = \boldsymbol{I}:\boldsymbol{C} = \lambda_1^2 + \lambda_2^2 + \lambda_3^2$ as first invariant
- $I_i = \boldsymbol{a}_0\boldsymbol{C}\boldsymbol{a}_0 = \lambda_1^2\cos^2\gamma + \lambda_2^2\sin^2\gamma\,, \quad i = 4{,}6$ as the squares of fiber stretch
- $I_i^* = \kappa I_1 + (1-3\kappa)I_i$ as squares of fiber stretch with dispersion

In the sensitivity analysis of transverse strain on different terms of constitutive relation, the estimated model parameters in Table 4.3 and the experiment data in Sokolis's research [150] is used. It is most intuitive to compare the sensitivity of the stress with respect to the invariants listed above. We can see from Figure 4.9 that the stress components are the most sensitive to volume change.

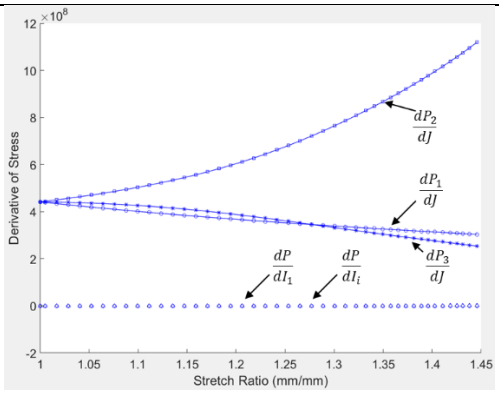

Figure 4.9 Comparison of sensitivity of stress components with respect to volumetric, isotropic and anisotropic parts.

The comparison of sensitivity of I_1 and I_i, which are isotropic and anisotropic parts, are shown in Figure 4.10. As a conclusion, the volumetric part of stress is the most sensitive to the transverse strain which is because of the bulk modulus K as a very large number (10^8). And the anisotropic part of stress is the second sensitive to transverse strain because k_1 is normally larger than μ and the exponential relation in the anisotropic term.

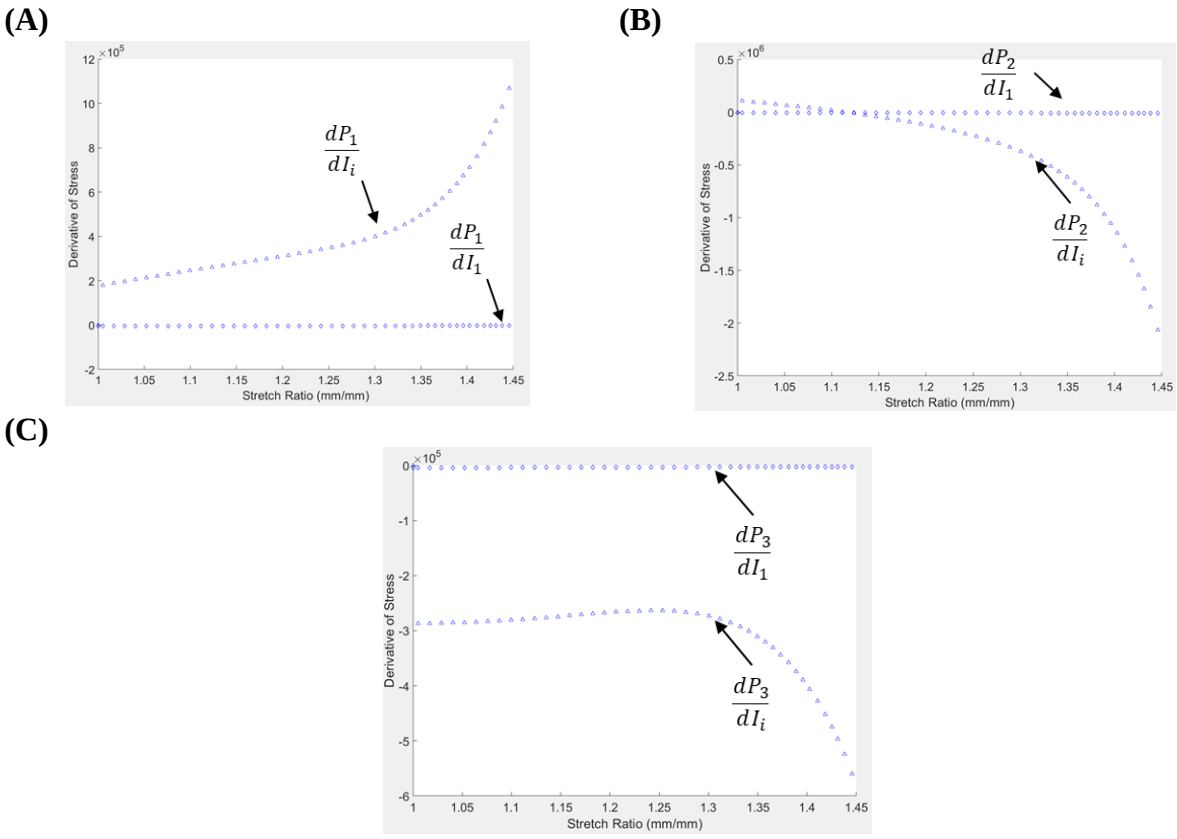

Figure 4.10 Comparison of sensitivity of isotropic and anisotropic parts for **(A)** Sensitivity of Tensile stress P_1 with respect to invariants I_1 and I_i , **(B)** Sensitivity of Transverse stress P_2 with respect to invariants I_1 and I_i , **(C)** Sensitivity of Thickness stress P_3 with respect to invariants I_1 and I_i.

CONCLUSION

PSSM mechanical properties were characterized through the analysis of uniaxial tensile tests under different orientations and locations. The PSSM material demonstrates the classic nonlinear and linear regions seen in other porcine skin studies and tissues. An Ogden model was used to analyze the PSSM's stress-stretch behavior. The Ogden model was able to be fit to the full curve, but the fit in the nonlinear region was improved by separating the curve into a toe and linear region. The findings of this work suggest that the tensile curve is best described by first separating the nonlinear and linear regions, and then analyzing each region with its own model. The PSSM results showed that:

(1) The Mechanical Parameters including Failure Stress, slope in the linear region, Failure Stretch and Ogden material constants are consistent with other porcine skin studies in the literature.

(2) The mechanical behavior was location dependent, where the back behaved anisotropically and the neck isotropically.

(3) The Mechanical Parameters and Ogden material constants demonstrated significant differences between the back and neck groups.

The PSSM mechanical properties in Chapter 2 can serve as a preliminary guide for engineers and scientists who are exploring the design of tissue engineering devices or processes. Further studies are needed to establish the correlation between the PSSM's sample location and respective mechanical properties. The experimental and theoretical characterization methods demonstrated in this study could help characterize other biologic materials in the tissue engineering field, and be used towards the development of tissue specific industrial standards.

In Chapter 3, the Microstructural Arrangement Determination Method (MADM) proposed and verified with the ABAQUS simulation data. By unifying the mechanical tests of uniaxial tensile samples in two orthogonal orientations, the mechanical properties can be accurately determined and the necessary of Histology Analysis can be eliminated. However, in Chapter 4, the implementation of MADM on experimental data of PSSM didn't converge to a good result, which indicates the GOH model might need some further development for better describing the material behavior. The treatment of transverse strain was concluded as the greatest reason of the failure on model calibration, which is the direction for the further exploration.

REFERENCES

[1] Deeken, C. R., and Lake, S. P., 2017, "Mechanical properties of the abdominal wall and biomaterials utilized for hernia repair," Journal of the mechanical behavior of biomedical materials, 74, pp. 411-427.

[2] Baylon, K., Rodriguez-Camarillo, P., Elias-Zuniga, A., Diaz-Elizondo, J. A., Gilkerson, R., and Lozano, K., 2017, "Past, Present and Future of Surgical Meshes: A Review," Membranes (Basel), 7(3).

[3] Rastegarpour, A., Cheung, M., Vardhan, M., Ibrahim, M. M., Butler, C. E., and Levinson, H., 2016, "Surgical mesh for ventral incisional hernia repairs: Understanding mesh design," Plastic Surgery, 24(1), pp. 41-50.

[4] Logan Ellis, H., Asaolu, O., Nebo, V., and Kasem, A., 2016, "Biological and synthetic mesh use in breast reconstructive surgery: a literature review," World journal of surgical oncology, 14, p. 121.

[5] Scheflan, M., and Colwell, A. S., 2014, "Tissue Reinforcement in Implant-based Breast Reconstruction," Plastic and reconstructive surgery global open, 2(8), p. e192.

[6] Hunter, J. D., 3rd, and Cannon, J. A., 2014, "Biomaterials: so many choices, so little time. What are the differences?," Clinics in colon and rectal surgery, 27(4), pp. 134-139.

[7] Primus, F. E., and Harris, H. W., 2013, "A critical review of biologic mesh use in ventral hernia repairs under contaminated conditions," Hernia, 17(1), pp. 21-30.

[8] Smart, N. J., Bryan, N., Hunt, J. A., and Daniels, I. R., 2014, "Porcine dermis implants in soft-tissue reconstruction: current status," Biologics, 8, pp. 83-90.

[9] Deeken, C. R., Eliason, B. J., Pichert, M. D., Grant, S. A., Frisella, M. M., and Matthews, B. D., 2012, "Differentiation of biologic scaffold materials through physicomechanical, thermal, and enzymatic degradation techniques," Annals of surgery, 255(3), pp. 595-604.

[10] Zhu, L. M., Schuster, P., and Klinge, U., 2015, "Mesh implants: An overview of crucial mesh parameters," World journal of gastrointestinal surgery, 7(10), pp. 226-236.

[11] Pott, P. P., Schwarz, M. L., Gundling, R., Nowak, K., Hohenberger, P., and Roessner, E. D., 2012, "Mechanical properties of mesh materials used for hernia repair and soft tissue augmentation," PLoS One, 7(10), p. e46978.

[12] "ASTM F2027-16, Standard Guide for Characterization and Testing of Raw or Starting Materials for Tissue-Engineered Medical Products," ASTM International, West Conshohocken, PA, 2016, www.astm.org.

[13] ASTM D638-14, Standard test method for tensile properties of plastics, ASTM International, West Conshohocken, PA, 2014, www.astm.org.

[14] Williams, L. S., and Hopper, P. D., 2015, Understanding medical surgical nursing, FA Davis.

[15] Dabbas, N., Adams, K., Pearson, K., and Royle, G., 2011, "Frequency of abdominal wall hernias: is classical teaching out of date?," JRSM short reports, 2(1), p. 5.

[16] Bendavid, R., 2001, Abdominal wall hernias: principles and management, Springer Science & Business Media.

[17] Kingsnorth, A., 2004, "Treating inguinal hernias: Open mesh Lichtenstein operation is preferred over laparoscopy," BMJ: British Medical Journal, 328(7431), p. 59.

[18] Li, X., Kruger, J. A., Jor, J. W., Wong, V., Dietz, H. P., Nash, M. P., and Nielsen, P. M., 2014, "Characterizing the ex vivo mechanical properties of synthetic polypropylene surgical mesh," Journal of the mechanical behavior of biomedical materials, 37, pp. 48-55.

[19] Zogbi, L., 2011, "The use of biomaterials to treat abdominal hernias," Biomaterials Applications for Nanomedicine, InTech.

[20] Society, A. C., 2017, "Breast Cancer Facts & Figures 2017-2018," Atlanta: American Cancer Society, Inc.

[21] Swine, M. R., "Precision leveling technology," http://midwestresearchswine.com/productsservices/midwest-research-swine/precision-layering-technology/.

[22] Swine, M. R., "Total quality assurance approach," http://midwestresearchswine.com/quality-control/quality-flow-chart/.

[23] Lanir, Y., 1987, "Chapter 11: Skin Mechanics," Handbook of Bioengineering.

[24] Griffiths, C., Barker, J., Bleiker, T., Chalmers, R., and Creamer, D., 2016, Rook's textbook of dermatology, John Wiley & Sons.

[25] Querleux, B., 2016, Computational Biophysics of the Skin, CRC Press.

[26] Goldsmith, L. A., 1991, Biochemistry and Physiology of the Skin, Oxford University Press.

[27] Oxlund, H., Manschot, J., and Viidik, A., 1988, "The role of elastin in the mechanical properties of skin," Journal of biomechanics, 21(3), pp. 213-218.

[28] Groves, R. B., Coulman, S., Birchall, J. C., and Evans, S. L., 2012, "Quantifying the mechanical properties of human skin to optimise future microneedle device design," Computer methods in biomechanics and biomedical engineering, 15(1), pp. 73-82.

[29] Joodaki, H., and Panzer, M. B., 2018, "Skin mechanical properties and modeling: A review," Proceedings of the Institution of Mechanical Engineers, Part H: Journal of Engineering in Medicine, 232(4), pp. 323-343.

[30] Caro-Bretelle, A., Gountsop, P., Ienny, P., Leger, R., Corn, S., Bazin, I., and Bretelle, F., 2015, "Effect of sample preservation on stress softening and permanent set of porcine skin," Journal of biomechanics, 48(12), pp. 3135-3141.

[31] Daly, C. H., and Odland, G. F., 1979, "Age-related changes in the mechanical properties of human skin," Journal of Investigative Dermatology, 73(1), pp. 84-87.

[32] Del Prete, Z., Antoniucci, S., Hoffman, A. H., and Grigg, P., 2004, "Viscoelastic properties of skin in Mov-13 and Tsk mice," Journal of Biomechanics, 37(10), pp. 1491-1497.

[33] Munoz, M., Bea, J., Rodriguez, J., Ochoa, I., Grasa, J., del Palomar, A. P., Zaragoza, P., Osta, R., and Doblaré, M., 2008, "An experimental study of the mouse skin behaviour: damage and inelastic aspects," Journal of biomechanics, 41(1), pp. 93-99.

[34] Annaidh, A. N., Bruyere, K., Destrade, M., Gilchrist, M. D., Maurini, C., Otténio, M., and Saccomandi, G., 2012, "Automated estimation of collagen fibre dispersion in the dermis and its contribution to the anisotropic behaviour of skin," Annals of biomedical engineering, 40(8), pp. 1666-1678.

[35] Annaidh, A. N., Bruyère, K., Destrade, M., Gilchrist, M. D., and Otténio, M., 2012, "Characterization of the anisotropic mechanical properties of excised human skin," Journal of the mechanical behavior of biomedical materials, 5(1), pp. 139-148.

[36] Gallagher, A., Ní Annaidh, A., and Bruyère, K., 2012, "Dynamic tensile properties of human skin," IRCOBI Conference 2012, 12-14 September 2012, Dublin (Ireland), International Research Council on the Biomechanics of Injury.

[37] Karimi, A., Rahmati, S. M., and Navidbakhsh, M., 2015, "Mechanical characterization of the rat and mice skin tissues using histostructural and uniaxial data," Bioengineered, 6(3), pp. 153-160.

[38] Ankersen, J., Birkbeck, A. E., Thomson, R. D., and Vanezis, P., 1999, "Puncture resistance and tensile strength of skin simulants," Proceedings of the Institution of Mechanical Engineers, Part H: Journal of Engineering in Medicine, 213(6), pp. 493-501.

[39] Ridge, M., and Wright, V., 1966, "Mechanical properties of skin: a bioengineering study of skin structure," Journal of applied physiology, 21(5), pp. 1602-1606.

[40] Żak, M., Kuropka, P., Kobielarz, M., Dudek, A., Kaleta-Kuratewicz, K., and Szotek, S., 2011, "Determination of the mechanical properties of the skin of pig foetuses with respect to its structure," Acta of Bioengineering and Biomechanics, 13(2), pp. 37-43.

[41] Riemersa, D., and Schamhardt, H., 1982, "The cryo-jaw, a clamp designed for in vitro rheology studies of horse digital flexor tendons," Journal of biomechanics, 15(8), pp. 619-620.

[42] Shi, D., Wang, D., Wang, C., and Liu, A., 2012, "A novel, inexpensive and easy to use tendon clamp for in vitro biomechanical testing," Medical Engineering and Physics, 34(4), pp. 516-520.

[43] Ng, B., Chou, S., and Krishna, V., 2005, "The influence of gripping techniques on the tensile properties of tendons," Proceedings of the Institution of Mechanical Engineers, Part H: Journal of Engineering in Medicine, 219(5), pp. 349-354.

[44] Łagan, S., and Liber-Kneć, A., 2017, "Application of the Ogden Model to the Tensile Stress-Strain Behavior of the Pig's Skin," Innovations in Biomedical Engineering, Springer, pp. 145-152.

[45] Shergold, O. A., Fleck, N. A., and Radford, D., 2006, "The uniaxial stress versus strain response of pig skin and silicone rubber at low and high strain rates," International Journal of Impact Engineering, 32(9), pp. 1384-1402.

[46] Stark, H., 1977, "Directional variations in the extensibility of human skin," British Journal of Plastic Surgery, 30(2), pp. 105-114.

[47] Huang, H.-Y. S., Huang, S., Gettys, T., Prim, P. M., and Harrysson, O. L., 2013, "A biomechanical study of directional mechanical properties of porcine skin tissues," ASME 2013 International Mechanical Engineering Congress and Exposition, American Society of Mechanical Engineers, pp. V009T010A052-V009T010A052.

[48] Lanir, Y., and Fung, Y., 1974, "Two-dimensional mechanical properties of rabbit skin—II. Experimental results," Journal of biomechanics, 7(2), pp. 171-174.

[49] Wilkes, G., Brown, I., and Wildnauer, R., 1973, "The biomechanical properties of skin," CRC critical reviews in bioengineering, 1(4), pp. 453-495.

[50] Edwards, C., and Marks, R., 1995, "Evaluation of biomechanical properties of human skin," Clinics in dermatology, 13(4), pp. 375-380.

[51] Uzer, G., Ho, A., Clark, R., and Fu-pen, C., 2009, "Mechanical properties of pig skin," Proceedings of the Society for Experimental Mechanics Annual Conference.

[52] Pereira, J., Mansour, J., and Davis, B., 1991, "Dynamic measurement of the viscoelastic properties of skin," Journal of biomechanics, 24(2), pp. 157-162.

[53] Roeder, B. A., Kokini, K., Sturgis, J. E., Robinson, J. P., and Voytik-Harbin, S. L., 2002, "Tensile mechanical properties of three-dimensional type I collagen extracellular matrices with varied microstructure," Journal of biomechanical engineering, 124(2), pp. 214-222.

[54] Delalleau, A., Josse, G., Lagarde, J. M., Zahouani, H., and Bergheau, J. M., 2008, "A nonlinear elastic behavior to identify the mechanical parameters of human skin in vivo," Skin research and Technology, 14(2), pp. 152-164.

[55] Lake, S. P., Miller, K. S., Elliott, D. M., and Soslowsky, L. J., 2009, "Effect of fiber distribution and realignment on the nonlinear and inhomogeneous mechanical properties of human supraspinatus tendon under longitudinal tensile loading," Journal of Orthopaedic Research, 27(12), pp. 1596-1602.

[56] Wan, C., Hao, Z., Wen, S., and Leng, H., 2014, "A quantitative study of the relationship between the distribution of different types of collagen and the mechanical behavior of rabbit medial collateral ligaments," PLoS One, 9(7), p. e103363.

[57] Eshel, H., and Lanir, Y., 2001, "Effects of strain level and proteoglycan depletion on preconditioning and viscoelastic responses of rat dorsal skin," Annals of biomedical engineering, 29(2), pp. 164-172.

[58] Ottenio, M., Tran, D., Annaidh, A. N., Gilchrist, M. D., and Bruyère, K., 2015, "Strain rate and anisotropy effects on the tensile failure characteristics of human skin," Journal of the mechanical behavior of biomedical materials, 41, pp. 241-250.

[59] Haut, R., 1989, "The effects of orientation and location on the strength of dorsal rat skin in high and low speed tensile failure experiments," Journal of biomechanical engineering, 111(2), pp. 136-140.

[60] Dombi, G. W., Haut, R. C., and Sullivan, W. G., 1993, "Correlation of high-speed tensile strength with collagen content in control and lathyritic rat skin," Journal of Surgical Research, 54(1), pp. 21-28.

[61] Khatyr, F., Imberdis, C., Vescovo, P., Varchon, D., and Lagarde, J. M., 2004, "Model of the viscoelastic behaviour of skin in vivo and study of anisotropy," Skin research and technology, 10(2), pp. 96-103.

[62] Agache, P., 2000, "Collection Explorations Fonctionnelles Humaines," Physiologie de la Peau et Explorations Fonctionnelles Cutanées.

[63] Dupuytren, G., 1835, Traité théorique et pratique des blessures par armes de guerre, H. Dumont.

[64] Langer, K., 1978, "On the anatomy and physiology of the skin: I. The cleavability of the cutis," British journal of plastic surgery, 31(1), pp. 3-8.

[65] Langer, K., 1978, "On the anatomy and physiology of the skin. II. Skin tension," Br J Plast Surg, 31, pp. 93-106.

[66] Rose, E. H., Ksander, G. A., and Vistnes, L. M., 1976, "Skin tension lines in the domestic pig," Plastic and reconstructive surgery, 57(6), pp. 729-732.

[67] Flint, M., 1976, "The biological basis of Langer's lines," The Ultrastructure of Collagen. Springfield IL: Charles C Thomas, pp. 132-140.

[68] Cox, H., 1941, "The cleavage lines of the skin," British Journal of Surgery, 29(114), pp. 234-240.

[69] Liu, Z., and Yeung, K., 2008, "The preconditioning and stress relaxation of skin tissue," Journal of Biomedical & Pharmaceutical Engineering, 2(1), pp. 22-28.

[70] Graf, B. K., Vanderby, R., Ulm, M. J., Rogalski, R. P., and Thielke, R. J., 1994, "Effect of preconditioning on the viscoelastic response of primate patellar tendon," Arthroscopy, 10(1), pp. 90-96.

[71] Fung, Y.-C., 1993, "Bioviscoelastic solids," Biomechanics, Springer, pp. 242-320.

[72] Minns, R., Soden, P., and Jackson, D., 1973, "The role of the fibrous components and ground substance in the mechanical properties of biological tissues: a preliminary investigation," Journal of biomechanics, 6(2), pp. 153-165.

[73] Łagan, S. D., and Liber-Kneć, A., 2017, "Experimental testing and constitutive modeling of the mechanical properties of the swine skin tissue," Acta of bioengineering and biomechanics, 19(2), pp. 93--102.

[74] Pan, B., Qian, K., Xie, H., and Asundi, A., 2009, "Two-dimensional digital image correlation for in-plane displacement and strain measurement: a review," Measurement Science and Technology, 20(6), p. 062001.

[75] Palanca, M., Tozzi, G., and Cristofolini, L., 2015, "The use of digital image correlation in the biomechanical area: a review," International Biomechanics, 3(1), pp. 1-21.

[76] Lionello, G., Sirieix, C., and Baleani, M., 2014, "An effective procedure to create a speckle pattern on biological soft tissue for digital image correlation measurements," Journal of the mechanical behavior of biomedical materials, 39, pp. 1-8.

[77] Gao, Z., and Desai, J. P., 2010, "Estimating zero-strain states of very soft tissue under gravity loading using digital image correlation," Medical image analysis, 14(2), pp. 126-137.

[78] Freddi, A., Olmi, G., and Cristofolini, L., 2015, Experimental Stress Analysis for Materials and Structures, Springer.

[79] Sutton, M., Ke, X., Lessner, S., Goldbach, M., Yost, M., Zhao, F., and Schreier, H., 2008, "Strain field measurements on mouse carotid arteries using microscopic three-dimensional digital image correlation," Journal of Biomedical Materials Research Part A, 84(1), pp. 178-190.

[80] Zhang, D., Zhang, X., and Cheng, G., 1999, "Compression strain measurement by digital speckle correlation," Experimental mechanics, 39(1), pp. 62-65.

[81] Zhou, P., and Goodson, K. E., 2001, "Subpixel displacement and deformation gradient measurement using digital image/speckle correlation (DISC)," Optical Engineering, 40(8), pp. 1613-1620.

[82] Bay, B. K., 1995, "Texture correlation: a method for the measurement of detailed strain distributions within trabecular bone," Journal of Orthopaedic Research, 13(2), pp. 258-267.

[83] Gaudette, G. R., Todaro, J., Krukenkamp, I. B., and Chiang, F.-P., 2001, "Computer aided speckle interferometry: a technique for measuring deformation of the surface of the heart," Annals of biomedical engineering, 29(9), pp. 775-780.

[84] Chen, D., and Chiang, F., 1993, "Computer-aided speckle interferometry using spectral amplitude fringes," Applied Optics, 32(2), pp. 225-236.

[85] Sjödahl, M., and Benckert, L., 1993, "Electronic speckle photography: analysis of an algorithm giving the displacement with subpixel accuracy," Applied Optics, 32(13), pp. 2278-2284.

[86] Synnergren, P., 1997, "Measurement of three-dimensional displacement fields and shape using electronic speckle photography," Optical Engineering, 36(8), pp. 2302-2310.

[87] Crammond, G., Boyd, S., and Dulieu-Barton, J., 2013, "Speckle pattern quality assessment for digital image correlation," Optics and Lasers in Engineering, 51(12), pp. 1368-1378.

[88] Lecompte, D., Smits, A., Bossuyt, S., Sol, H., Vantomme, J., Van Hemelrijck, D., and Habraken, A., 2006, "Quality assessment of speckle patterns for digital image correlation," Optics and lasers in Engineering, 44(11), pp. 1132-1145.

[89] Pan, B., Xie, H., Wang, Z., Qian, K., and Wang, Z., 2008, "Study on subset size selection in digital image correlation for speckle patterns," Optics express, 16(10), pp. 7037-7048.

[90] Myers, K. M., Coudrillier, B., Boyce, B. L., and Nguyen, T. D., 2010, "The inflation response of the posterior bovine sclera," Acta biomaterialia, 6(11), pp. 4327-4335.

[91] Bucinell, R. B., Adams, M. T., Dlamini, M., and Fleishman, L. J., 2016, "Technique for In-Vivo Measurements of Heart Deformation Using Digital Image Correlation," American Journal of Engineering and Applied Sciences, 9(4), pp. 1144-1149.

[92] Thompson, M. S., Schell, H., Lienau, J., and Duda, G. N., 2007, "Digital image correlation: a technique for determining local mechanical conditions within early bone callus," Medical engineering & physics, 29(7), pp. 820-823.

[93] Libertiaux, V., Pascon, F., and Cescotto, S., 2011, "Experimental verification of brain tissue incompressibility using digital image correlation," Journal of the mechanical behavior of biomedical materials, 4(7), pp. 1177-1185.

[94] Moerman, K. M., Holt, C. A., Evans, S. L., and Simms, C. K., 2009, "Digital image correlation and finite element modelling as a method to determine mechanical properties of human soft tissue in vivo," Journal of biomechanics, 42(8), pp. 1150-1153.

[95] Wang, C. C. B., Chahine, N. O., Hung, C. T., and Ateshian, G. A., 2003, "Optical determination of anisotropic material properties of bovine articular cartilage in compression," Journal of Biomechanics, 36(3), pp. 339-353.

[96] Wang, Y., and Cuitiño, A. M., 2002, "Full-field measurements of heterogeneous deformation patterns on polymeric foams using digital image correlation," International Journal of Solids and Structures, 39(13), pp. 3777-3796.

[97] Zhang, D., and Arola, D. D., 2004, "Applications of digital image correlation to biological tissues," Journal of Biomedical Optics, 9(4), pp. 691-699.

[98] Guan, E., Smilow, S., Rafailovich, M., and Sokolov, J., 2004, "Determining the mechanical properties of rat skin with digital image speckle correlation," Dermatology, 208(2), pp. 112-119.

[99] Nagarkatti, D. G., McKeon, B. P., Donahue, B. S., and Fulkerson, J. P., 2001, "Mechanical evaluation of a soft tissue interference screw in free tendon anterior cruciate ligament graft fixation," The American journal of sports medicine, 29(1), pp. 67-71.

[100] Holzapfel, G. A., 2006, "Determination of material models for arterial walls from uniaxial extension tests and histological structure," Journal of theoretical biology, 238(2), pp. 290-302.

[101] Fritz, J. R., Phillips, B. T., Conkling, N., Fourman, M., Melendez, M. M., Bhatnagar, D., Simon, M., Rafailovich, M., and Dagum, A. B., 2012, "Comparison of native porcine skin and a dermal substitute using tensiometry and digital image speckle correlation," Annals of plastic surgery, 69(4), pp. 462-467.

[102] Limbert, G., 2017, "Mathematical and computational modelling of skin biophysics: a review," Proceedings of the Royal Society A: Mathematical, Physical and Engineering Sciences, 473(2203), p. 20170257.

[103] Holzapfel, G. A., and Ogden, R. W., 2010, "Constitutive modelling of arteries," Proceedings of the Royal Society A: Mathematical, Physical and Engineering Sciences, 466(2118), pp. 1551-1597.

[104] Veronda, D., and Westmann, R., 1970, "Mechanical characterization of skin—finite deformations," Journal of biomechanics, 3(1), pp. 111-124.

[105] Ogden, R. W., 1972, "Large deformation isotropic elasticity–on the correlation of theory and experiment for incompressible rubberlike solids," Proc. R. Soc. Lond. A, The Royal Society, pp. 565-584.

[106] Fung, Y.-c., 2013, Biomechanics: mechanical properties of living tissues, Springer Science & Business Media.

[107] Lanir, Y., 1983, "Constitutive equations for fibrous connective tissues," Journal of biomechanics, 16(1), pp. 1-12.

[108] Groves, R. B., Coulman, S. A., Birchall, J. C., and Evans, S. L., 2013, "An anisotropic, hyperelastic model for skin: experimental measurements, finite element modelling and identification of parameters for human and murine skin," Journal of the mechanical behavior of biomedical materials, 18, pp. 167-180.

[109] Gasser, T. C., Ogden, R. W., and Holzapfel, G. A., 2006, "Hyperelastic modelling of arterial layers with distributed collagen fibre orientations," Journal of the royal society interface, 3(6), pp. 15-35.

[110] Tong, P., and Fung, Y.-C., 1976, "The stress-strain relationship for the skin," Journal of Biomechanics, 9(10), pp. 649-657.

[111] Lokshin, O., and Lanir, Y., 2009, "Viscoelasticity and preconditioning of rat skin under uniaxial stretch: microstructural constitutive characterization," Journal of biomechanical engineering, 131(3), p. 031009.

[112] Holzapfel, G. A., Niestrawska, J. A., Ogden, R. W., Reinisch, A. J., and Schriefl, A. J., 2015, "Modelling non-symmetric collagen fibre dispersion in arterial walls," Journal of the royal society interface, 12(106).

[113] Cortes, D. H., Lake, S. P., Kadlowec, J. A., Soslowsky, L. J., and Elliott, D. M., 2010, "Characterizing the mechanical contribution of fiber angular distribution in connective tissue: comparison of two modeling approaches," Biomechanics and modeling in mechanobiology, 9(5), pp. 651-658.

[114] Holzapfel, G. A., Gasser, T. C., and Ogden, R. W., 2000, "A new constitutive framework for arterial wall mechanics and a comparative study of material models," Journal of elasticity and the physical science of solids, 61(1-3), pp. 1-48.

[115] Holzapfel, G. A., and Ogden, R. W., 2016, "On Fiber Dispersion Models: Exclusion of Compressed Fibers and Spurious Model Comparisons," Journal of Elasticity, 129(1-2), pp. 49-68.

[116] Gurtin, M. E., Fried, E., and Anand, L., 2010, The mechanics and thermodynamics of continua, Cambridge University Press.

[117] Arruda, E. M., and Boyce, M. C., 1993, "A three-dimensional constitutive model for the large stretch behavior of rubber elastic materials," Journal of the Mechanics and Physics of Solids, 41(2), pp. 389-412.

[118] Yeoh, O., 1993, "Some forms of the strain energy function for rubber," Rubber Chemistry and technology, 66(5), pp. 754-771.

[119] Holzapfel, G. A., 2001, "Biomechanics of soft tissue," The handbook of materials behavior models, 3, pp. 1049-1063.

[120] Holzapfel, G. A., 2002, "Nonlinear solid mechanics: a continuum approach for engineering science," Meccanica, 37(4), pp. 489-490.

[121] Holzapfel, G. A., and Gasser, T. C., 2001, "A viscoelastic model for fiber-reinforced composites at finite strains: continuum basis, computational aspects and applications," Computer methods in applied mechanics and engineering, 190(34), pp. 4379-4403.

[122] Hillman, H., 2000, "Limitations of clinical and biological histology," Medical hypotheses, 54(4), pp. 553-564.

[123] Kuo, Y., Yang, T., and Huang, G.-W., 2008, "The use of grey relational analysis in solving multiple attribute decision-making problems," Computers & Industrial Engineering, 55(1), pp. 80-93.

[124] Donovan, P. J., and Gearhart, J., 2001, "The end of the beginning for pluripotent stem cells," Nature, 414(6859), pp. 92-97.

[125] Banabic, D., 2010, Sheet metal forming processes: constitutive modelling and numerical simulation, Springer Science & Business Media.

[126] Hill, R., 1948, "A theory of the yielding and plastic flow of anisotropic metals," Proceedings of the Royal Society of London. Series A. Mathematical and Physical Sciences, 193(1033), pp. 281-297.

[127] Glieck, J., "New York Times, 14 April 1987," Science Times, p. 21.

[128] Milton, G. W., 1992, "Composite materials with Poisson's ratios close to—1," Journal of the Mechanics and Physics of Solids, 40(5), pp. 1105-1137.

[129] Caddock, B., and Evans, K., 1989, "Microporous materials with negative Poisson's ratios. I. Microstructure and mechanical properties," Journal of Physics D: Applied Physics, 22(12), p. 1877.

[130] Lakes, R., 1987, "Foam structures with a negative Poisson's ratio," Science, 235, pp. 1038-1041.

[131] Lowe, A., and Lakes, R., 2000, "Negative Poisson's ratio foam as seat cushion material," Cellular Polymers, 19(3), pp. 157-168.

[132] Yanping, L., Hong, H., Lam, J. K. C., and Su, L., 2009, "Negative Poisson's Ratio Weft-knitted Fabrics," Textile Research Journal, 80(9), pp. 856-863.

[133] Williams, J., and Lewis, J., 1982, "Properties and an anisotropic model of cancellous bone from the proximal tibial epiphysis," Journal of biomechanical engineering, 104(1), pp. 50-56.

[134] Lees, C., Vincent, J. F., and Hillerton, J. E., 1991, "Poisson's ratio in skin," Bio-medical materials and engineering, 1(1), pp. 19-23.

[135] Geerligs, M., 2006, "A literature review of the mechanical behavior of the stratum corneum, the living epidermis and the subcutaneous fat tissue," Philips Research.

[136] Foutz, T., Stone, E., and Abrams Jr, C., 1992, "Effects of freezing on mechanical properties of rat skin," American journal of veterinary research, 53(5), pp. 788-792.

[137] Ranamukhaarachchi, S. A., Lehnert, S., Ranamukhaarachchi, S. L., Sprenger, L., Schneider, T., Mansoor, I., Rai, K., Hafeli, U. O., and Stoeber, B., 2016, "A micromechanical comparison of human and porcine skin before and after preservation by freezing for medical device development," Scientific reports, 6, p. 32074.

[138] Pramudita, J. A., Shimizu, Y., Tanabe, Y., Ito, M., and Watanabe, R., 2014, "Tensile Properties of Porcine Skin in Dorsal and Ventral Regions," Journal of the Japanese Society for Experimental Mechanics, 14(Special_Issue), pp. s245-s250.

[139] Virues Delgadillo, J. O., Delorme, S., El-Ayoubi, R., DiRaddo, R., and Hatzikiriakos, S. G., 2010, "Effect of freezing on the passive mechanical properties of arterial samples," Journal of Biomedical Science and Engineering, 03(07), pp. 645-652.

[140] Zhou, B., Xu, F., Chen, C. Q., and Lu, T. J., 2010, "Strain rate sensitivity of skin tissue under thermomechanical loading," Physical and Engineering Sciences, 368(1912), pp. 679-690.

[141] Lim, J., Hong, J., Chen, W. W., and Weerasooriya, T., 2011, "Mechanical response of pig skin under dynamic tensile loading," International Journal of Impact Engineering, 38(2-3), pp. 130-135.

[142] Li, W., and Luo, X., 2016, "An Invariant-Based Damage Model for Human and Animal Skins," Annals of biomedical engineering, 44(10), pp. 3109-3122.

[143] Bonet, J., and Wood, R. D., 1997, Nonlinear continuum mechanics for finite element analysis, Cambridge university press.

[144] Tan, Q., Wang, Q., Liu, D., Zhang, S., Zhang, Y., and Li, Y., 2015, "Intravascular ultrasound-guided unprotected left main coronary artery stenting in the elderly," Saudi medical journal, 36(5), p. 549.

[145] Balaban, G., Alnæs, M. S., Sundnes, J., and Rognes, M. E., 2016, "Adjoint multi-start-based estimation of cardiac hyperelastic material parameters using shear data," Biomechanics and modeling in mechanobiology, 15(6), pp. 1509-1521.

[146] Hoffman, A. H., Teng, Z., Zheng, J., Wu, Z., Woodard, P. K., Billiar, K. L., Wang, L., and Tang, D., 2017, "Stiffness properties of adventitia, media, and full thickness human atherosclerotic carotid arteries in the axial and circumferential directions," Journal of biomechanical engineering, 139(12).

[147] Kohn, J. C., Lampi, M. C., and Reinhart-King, C. A., 2015, "Age-related vascular stiffening: causes and consequences," Frontiers in genetics, 6, p. 112.

[148] Khanafer, K., Schlicht, M., and Berguer, R., 2013, "How should we measure and report elasticity in aortic tissue?," European Journal of Vascular and Endovascular Surgery, 45(4), pp. 332-339.

[149] Holzapfel, G. A., Sommer, G., and Regitnig, P., 2004, "Anisotropic mechanical properties of tissue components in human atherosclerotic plaques," Journal of biomechanical engineering, 126(5), pp. 657-665.

[150] Sokolis, D. P., Kritharis, E. P., and Iliopoulos, D. C., 2012, "Effect of layer heterogeneity on the biomechanical properties of ascending thoracic aortic aneurysms," Medical & biological engineering & computing, 50(12), pp. 1227-1237.

[151] Latorre, M., Romero, X., and Montans, F. J., 2016, "The relevance of transverse deformation effects in modeling soft biological tissues," International Journal of Solids and Structures, 99, pp. 57-70.